Cover illustration
The entangling of atoms through spin coupling in a double-well potential (Courtesy of I. Bloch)

Editor, *Nature*
Philip Campbell
Insights Publisher
Steven Inchcoombe
Insights Editor
Karl Ziemelis
Production Editor
Davina Dadley-Moore
Senior Art Editor
Martin Harrison
Art Editor
Nik Spencer
Sponsorship
Amélie Pequignot
Production
Jocelyn Hilton
Marketing
Katy Dunningham
Elena Woodstock
Editorial Assistant
Alison McGill

QUANTUM COHERENCE

Quantum physics has come a long way since its theoretical beginnings in the early twentieth century. Techniques to manipulate light and matter have become increasingly sophisticated, facilitating fundamental studies of quantum effects and inspiring new technologies. From atomic networks to semiconductor 'spintronics', seemingly disparate areas of research are being driven by a shared goal — to harness and exploit quantum coherence and entanglement.

Inevitably, these laboratory endeavours have necessitated a new theoretical toolbox. The image of a pair of photons zooming off in opposite directions, each sensitive to the other through their quantum entanglement, is conceptually tidy. But what happens when describing the quantum properties of more complex systems? This Insight on quantum coherence and entanglement starts with a Progress article that addresses the problem of 'thinking big': how can entanglement be quantified or measured in a system that comprises many particles and degrees of freedom?

The reviews in this Insight highlight the exciting experimental progress in such systems, covering a wide range of physical settings. They describe both bottom-up approaches, in which researchers strive to achieve increasingly complex systems starting from a very small number of particles and degrees of freedom, and top-down approaches, in which the individual and collective degrees of freedom in larger systems are controlled. Ultimately, the goal is to control many-particle systems at the quantum limit, an attractive prospect for quantum simulation and information applications.

As such, this Insight brings together varied research. We trust, however, that you will find coherence in this diversity.

Karen Southwell, Senior Editor

PROGRESS

REVIEWS

nature insight

© 2008 Macmillan Publishers Limited. All rights reserved

NATURE|Vol 453|19 June 2008|doi:10.1038/nature07124

Quantifying entanglement in macroscopic systems

Vlatko Vedral[1,2,3]

Traditionally, entanglement was considered to be a quirk of microscopic objects that defied a common-sense explanation. Now, however, entanglement is recognized to be ubiquitous and robust. With the realization that entanglement can occur in macroscopic systems — and with the development of experiments aimed at exploiting this fact — new tools are required to define and quantify entanglement beyond the original microscopic framework.

In the past decade, there has been an explosion of interest in entanglement in macroscopic (many body) physical systems[1]. The transformation in how entanglement is perceived has been remarkable. In less than a century, researchers have moved from distrusting entanglement because of its 'spooky action at a distance' to starting to regard it as an essential property of the macroscopic world.

There are three basic motivations for studying entanglement in the macroscopic world. The first motivation is fundamental. Researchers want to know whether large objects can support entanglement. The conventional wisdom is that a system that consists of a large number of subsystems (for example, 10^{26} of them, similar to the number of atoms in a living room) immersed in an environment at a high temperature (room temperature, for example) ought to behave fully classically. Studying macroscopic entanglement is thus a way of probing the quantum-to-classical transition.

The second motivation is physical and relates to the different phases of matter. Traditionally, the idea of an order parameter is used to quantify phase transitions. For example, a non-magnetic system (in the 'disordered phase') can be magnetized (or become ordered) in certain conditions, and this transition is indicated by an abrupt change in the order parameter of the system. In this case, the magnetization itself is a relevant order parameter, but the interesting question is whether entanglement is a useful order parameter for other phase transitions[2,3].

The third motivation comes from technology. If the power of entanglement is to be harnessed through quantum computing, then entangled systems of increasingly large sizes need to be handled, which is itself a challenge.

It is clear that the modern perspective on entanglement differs greatly from the initial ideas about its seemingly paradoxical nature. Researchers are now realizing how general and robust entanglement is. Larger and larger entangled systems are being manipulated coherently in different physical implementations. And it is not as surprising as it once was to find that entanglement contributes to some phenomena.

Not all of the mystery has vanished, however. As is common in scientific research, answering one question generates many new ones, in this case related to the type of entanglement that is useful for studies motivated by each of the three reasons above. These questions bring researchers closer to the heart of the current understanding of entanglement.

Here I first examine what entanglement is and how it is quantified in physical systems. Different classes of entanglement are then discussed, and I conclude by considering the possibilities of achieving and exploiting large-scale entanglement in the laboratory.

What is entanglement?

The first chapter of almost any elementary quantum-mechanics textbook usually states that quantum behaviour is not relevant for systems with a physical size much larger than their de Broglie wavelength. The de Broglie wavelength, which can intuitively be thought of as the quantum extent of the system, scales inversely as (the square root of) mass

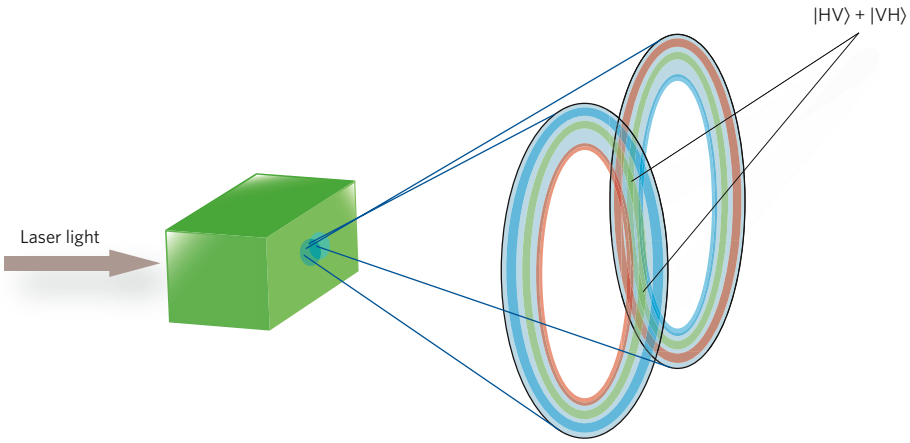

Figure 1 | A way of generating entangled photons by using down conversion. The input laser light is shone onto a nonlinear crystal (green box). The nonlinearity of the crystal means that there is a non-zero probability that two photons will be emitted from the crystal. The cones represent the regions where each of the two photons is emitted. Owing to energy conservation, the frequencies of the photons need to add up to the original frequency. Their momenta also must cancel in the perpendicular direction and add up to the original momentum in the forward direction. One of the photons is horizontally polarized (H), and one is vertically polarized (V). However, in the regions where the two cones overlap, the state of the photons will be $|\mathrm{HV}\rangle + |\mathrm{VH}\rangle$. It is around these points that entangled photons are generated.

[1]School of Physics and Astronomy, University of Leeds, Leeds LS2 9JT, UK. [2]Centre for Quantum Technologies, National University of Singapore, 3 Science Drive 2, Singapore 117543. [3]Department of Physics, National University of Singapore, 2 Science Drive 3, Singapore 117542.

© 2008 Macmillan Publishers Limited. All rights reserved

times temperature. From this, it can be concluded that massive and hot systems — which could almost be considered as synonymous with macroscopic systems — should not behave quantum mechanically.

As I show in the next section, however, de-Broglie-type arguments are too simplistic. First, entanglement can be found in macroscopic systems[4] (including at high temperatures[5]). And, second, entanglement turns out to be crucial for explaining the behaviour of large systems[6]. For example, the low values of magnetic susceptibilities in some magnetic systems can be explained only by using entangled states of those systems.

Now, what exactly is entanglement? After all is said and done, it takes (at least) two to tangle[7], although these two need not be particles. To study entanglement, two or more subsystems need to be identified, together with the appropriate degrees of freedom that might be entangled. The subsystems are technically known as modes, and the possibly entangled degrees of freedom are called observables. Most formally, entanglement is the degree of correlation between observables pertaining to different modes that exceeds any correlation allowed by the laws of classical physics.

I now describe several examples of entangled systems. Two photons that have been generated by, for example, parametric down conversion[8] are in the overall polarized state $|\mathrm{HV}\rangle + |\mathrm{VH}\rangle$ (where H is horizontal polarization and V is vertical polarization) and are entangled as far as their polarization is concerned (Fig. 1). A photon is an excitation of the electromagnetic field, and its polarization denotes the direction of the electric field. Each of the two entangled photons represents a subsystem, and the relevant observables are the polarizations in different directions. (Two electrons could also be entangled in terms of their spin value in an analogous way.)

When two subsystems in pure states become entangled, the overall state can no longer be written as a product of the individual states (for example, $|\mathrm{HV}\rangle$). A pure state means that the information about how the state was prepared is complete. A state is called mixed if some knowledge is lacking about the details of system preparation. For example, if the apparatus prepares either the ground state $|0\rangle$ or the first excited state $|1\rangle$ in a random manner, with respective probabilities p and $1-p$, then the overall state will need to be described as the mixture $p|0\rangle\langle 0| + (1-p)|1\rangle\langle 1|$. In this case, the probabilities need to be used to describe the state because of the lack of knowledge. Consequently, quantifying entanglement for mixed states is complex.

Systems can also be entangled in terms of their external degrees of freedom (such as in spatial parameters). For example, two particles could have their positions and momenta entangled. This was the original meaning of entanglement, as defined by Albert Einstein, Boris Podolsky and Nathan Rosen[9].

When the subsystems have been identified, states are referred to as entangled when they are not of the disentangled (or separable) form[10]: $\rho_{\mathrm{sep}} = \sum_i p_i \rho_1^i \otimes \rho_2^i \otimes \ldots \otimes \rho_n^i$, where $\sum_i p_i = 1$ is a probability distribution and $\rho_1^i, \rho_2^i, \ldots, \rho_n^i$ are the states (generally mixed) of subsystem 1, 2, …, n, respectively. On the one hand, two subsystems described by the density matrix $\rho_{12} = \frac{1}{2}(|00\rangle\langle 00| + |11\rangle\langle 11|)$ are one such example of a separable state. The state of three subsystems, $|000\rangle + |111\rangle$, on the other hand, can easily be confirmed to be not separable and therefore (by definition) entangled.

This simple mathematical definition hides a great deal of physical subtlety. For example, Bose–Einstein condensates are created when all particles in a system go into the same ground state. It seems that the overall state is just the product of the individual particle states and is therefore (by definition) disentangled. However, in this case, entanglement lies in the correlations between particle numbers in different spatial modes. Systems can also seem to be entangled but, on closer inspection, are not (Fig. 2).

Witnesses and measures of entanglement

In this section, I present two surprising results from recent studies of many-body entanglement: first, entanglement can be witnessed by macroscopic observables[11,12] (see the subsection 'Witnessing entanglement'); and second, entanglement can persist in the thermodynamic limit at arbitrarily high temperatures[13]. The first statement is surprising because observables represent averages over all subsystems, so it is expected that entanglement disappears as a result of this averaging. The effect of temperature is similar. Increasing the temperature means that an increasing amount of noise is added to the entanglement, so the second finding — that entanglement can persist at high temperatures — is also surprising.

Before these findings are described in more detail, a simple observation can be made. The entanglement of two subsystems in a pure state is very easy to quantify. This is because the more entangled the state, the more mixed the subset of the system. This property of quantum states — namely that although exact information about the overall state is available, information about parts of the system can be incomplete — was first emphasized by Erwin Schrödinger[14], in the famous paper in which he described the 'Schrödinger's cat' thought experiment.

This logic fails for mixed states, however. For example, an equal mixture of $|00\rangle$ and $|11\rangle$ also results in maximally mixed states for each quantum bit (qubit), but the overall state is not entangled. It also fails for quantifying quantum correlations between more than two components. In fact, in this last case, it is even difficult to determine whether a state of many subsystems is entangled in the first place. This leads on to the concept of witnessing entanglement.

Witnessing entanglement

Entanglement witnesses[15] are observables whose expectation value can indicate something about the entanglement in a given state. Suppose that there is an observable W, which has the property that for all disentangled states, the average value is bounded by some number b,

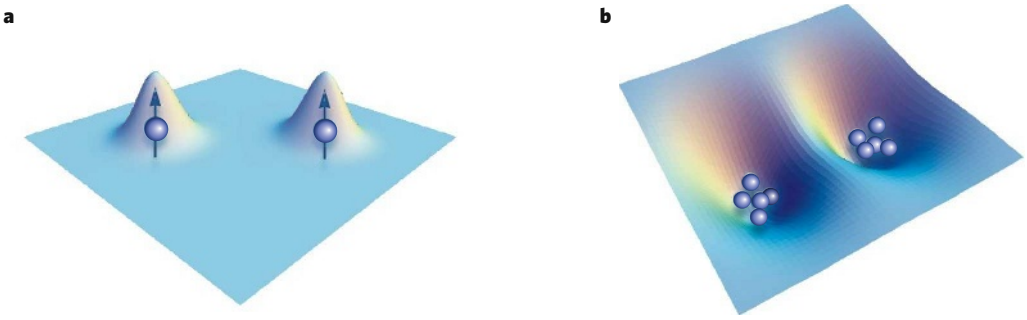

Figure 2 | Separable states. Two examples of disentangled systems are shown. **a**, Two electrons are shown confined to two spatial regions and with their internal spins pointing up. In this case, their spin states are both in the same upwards direction. Because electrons are fermions, the overall state of this system must be antisymmetrical. The internal state is symmetrical (because the electrons are pointing up), and so their special wavefunctions must be antisymmetrized, $|\Psi_1\Psi_2\rangle - |\Psi_2\Psi_1\rangle$. The spatial part of the electronic state, therefore, seems to be entangled — but this only seems to be the case. The electrons in question are fully distinguishable (because they are far apart), so any experiment on one of them is not correlated to any experiment on the other one. Therefore, these electrons cannot be entangled. **b**, A double-well potential, with each well containing five particles, is shown. Experiments that trap atoms in this way are now routine. It is clear that there is no entanglement between the two wells, because each well contains a fixed, clearly defined number of particles, although there could be some entanglement within each well, depending on the exact circumstances.

© 2008 Macmillan Publishers Limited. All rights reserved

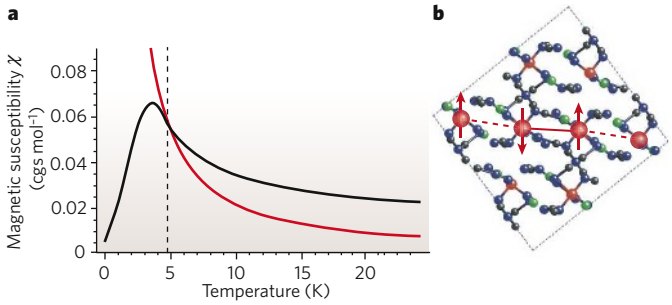

Figure 3 | Susceptibility as a macroscopic witness of entanglement. a, The typical behaviour of magnetic susceptibility χ versus temperature for a magnetic system is depicted (black). The behaviour of the entanglement witness is also depicted (red). Values of magnetic susceptibility below the red line are entangled, and the dashed line indicates the transitional point. **b,** One of the earliest experimental confirmations of entanglement[6] involved copper nitrate, $Cu(NO_3)_2{\cdot}2.5H_2O$, with entanglement existing at less than ~5 K. A molecular image of copper nitrate is depicted, with copper in red, nitrogen in blue, oxygen in black and hydrogen in green. The one-dimensional chain (red), which consists of interacting copper atoms, is the physically relevant chain in terms of the magnetic properties of the compound and can be thought of as a collection of dimers (shown separated by dashed red lines).

$\langle W\rangle \leq b$. Suppose, furthermore, that a researcher is given a physical state and experimentally shows that $\langle W\rangle > b$, then the only explanation is that the state is entangled.

Imagine two spins (a 'dimer') coupled through a Heisenberg interaction[4]: $H = -J\boldsymbol{\sigma}\bullet\boldsymbol{\sigma}$, where H is the hamiltonian, σ denotes a Pauli spin matrix and J is the strength of coupling. I now use the hamiltonian as an entanglement witness. It is easy to see that the average value of H with respect to disentangled (separable) states cannot exceed the value J: $\langle H\rangle = |\mathrm{Tr}(\rho_{\mathrm{sep}}H)| = J|\langle\boldsymbol{\sigma}\rangle\langle\boldsymbol{\sigma}\rangle| \leq J$. However, if the expected values are computed for the singlet state (which is the ground state of H), then the following is obtained: $|\mathrm{Tr}(\rho_{\mathrm{sin}}H)| = 3J$, where ρ_{sin} is the density matrix of the singlet state. This value is clearly outside the range of separable states. The singlet is therefore entangled. This logic generalizes to more complex hamiltonians (with arbitrarily many particles), and it can be shown that observables other than energy (for example, magnetic susceptibility) can be good witnesses of entanglement[1] (Fig. 3). In fact, by using this method, ground states of antiferromagnets, as well as other interacting systems, can generally be shown to be entangled at low temperatures ($k_BT \leq J$, where k_B is the Boltzmann constant and T is temperature; this seems to be a universal temperature bound for the existence of entanglement[16].

Measuring entanglement

Measuring entanglement is complex, and there are many approaches[17]. Here I discuss two measures of entanglement: overall entanglement and connectivity. Further measures are described in ref. 17.

The first measure is overall entanglement, also known as the relative entropy of entanglement[18], which is a measure of the difference between a given quantum state and any classically correlated state. It turns out that the best approximation to the Greenberger–Horne–Zeilinger (GHZ)[19] state, $|000\rangle + |111\rangle$, is a mixture of the form $|000\rangle\langle 000| + |111\rangle\langle 111|$. For W states[20] (by which I mean any symmetrical superposition of zeros and ones, such as $|001\rangle + |010\rangle + |100\rangle$), the best classical approximation is a slightly more elaborate mixture[5].

On the basis of overall entanglement, W states are more entangled than GHZ states. What is the most entangled state of N qubits according to the overall entanglement? The answer is that the maximum possible overall entanglement is $N/2$, and one such state that achieves this (by no means the only one) is a collection of dimers (that is, maximally entangled pairs of qubits). This is easy to understand when considering that each dimer has one unit of entanglement and that there are $N/2$ dimers in total.

The second measure (originally termed disconnectivity) is referred to here as connectivity[21]. Measuring connectivity is designed to address the question of how far correlations stretch. Take a GHZ state of N qubits, $|000\ldots0\rangle + |111\ldots1\rangle$. It is clear that the first two qubits are as correlated as the first and the third and, in fact, as the first and the last. Correlations of GHZ states therefore have a long range. GHZ states have a connectivity equal to N. The W state, by contrast, can be well described by nearest-neighbour correlations. The W state containing $N/2$ zeros and $N/2$ ones can be well approximated by the states $|01\rangle + |10\rangle$ between nearest neighbours. Therefore, correlations do not stretch far, and the connectivity is only equal to 2.

The above considerations of how to quantify entanglement are general and apply to all discrete (spin) systems, as well as to continuous systems (such as harmonic chains[22] and quantum fields[23]), although continuous systems need to be treated with extra care because of their infinite dimensionality. Although the discussed witnesses and measures can be applied to mixed states, I now focus on pure states for simplicity.

Different types of macroscopic entanglement

There are many types of entanglement. Here I discuss the four types that cover all three motivations mentioned earlier: GHZ, W, resonating valence bond (RVB)[24] and cluster[25]. GHZ states are typically used in testing the non-locality of quantum mechanics, because they have a high value of connectivity. W and RVB states naturally occur for a range of physical systems. For example, both Bose–Einstein condensates (such as superfluid and superconducting materials) and ferromagnets have W states as ground states[5].

RVB states are built from singlet states between pairs of spins. It is clear that connectivity of RVBs is only 2, but the states themselves have a high overall degree of entanglement, $N/2$ (ref. 26). It is intriguing that natural states have low connectivity but a high overall entanglement that scales as $\log N$ or even $N/2$, whereas GHZ states, which do not occur naturally, have high connectivity of the order of N but a very low overall entanglement (Box 1).

Are there states that have both connectivity and overall entanglement that scale as the number of subsystems? The answer is, surprisingly, yes. Even more interestingly, these states, which are known as cluster states, are important for quantum computing[25]. Cluster states are highly entangled arrays of qubits, and this entanglement is used to carry out quantum computing through single qubit measurements. Entanglement drives the dynamics of these computers[27], which is why high overall entanglement is needed. But the type of entanglement is also responsible for the implementation of various gates during the operation of these computers, which is why high connectivity is needed.

Experimental considerations and beyond

There are many paths to preparing and experimenting with larger collections of entangled systems. As I have described, natural entanglement is not strong in general and is far from being maximal with respect to overall entanglement or connectivity. To create high overall entanglement and connectivity invariably involves a great deal of effort.

There are two basic approaches to generating large-scale entanglement: bottom up and top down. The first approach, the bottom-up approach, relies on gaining precise control of a single system first and then extending this control to two systems and scaling it up further. So far, 'bottom-up experiments' have obtained up to eight entangled ions in an ion trap (in a W state)[28] and six entangled photons[29]. During nuclear magnetic resonance spectroscopy, 13 nuclei can be 'pseudo-entangled'[30]. Larger systems, however, are exceedingly difficult to control in this way.

The second approach is the top-down approach. As described earlier, many natural systems, with many degrees of freedom (1 million atoms, for example), can become entangled without the need for difficult manipulations (for example, the only requirement might be to decrease the temperature to less than 5 K, which is physically possible). Moreover, in many systems, certain types of entanglement are present in thermal equilibrium and even above room temperature, without the need for any manipulation.

© 2008 Macmillan Publishers Limited. All rights reserved

Box 1 | Comparison of four types of entangled qubit state

Qubit state	Overall entanglement	Connectivity
GHZ	1	*N*
W	Log *N*	2
RVB	*N*/2	2
Cluster	*N*/2	*N*

The naturally occurring states, W and RVB, have a much smaller connectivity than the states used for testing non-locality (GHZ) and for carrying out universal computing (cluster). In contrast to connectivity, the overall entanglement shows a different scaling. The important point is that the overall entanglement and connectivity capture markedly different aspects of the 'quantumness' of macroscopic states. Both of these measures can be thought of in terms of fragility of the entangled state, but they describe different types of fragility. The connectivity is related to the fragility of the state under dephasing: that is, the loss of phases between various components in the superposition. The overall entanglement, by contrast, is related to the fragility of the state under the full removal of qubits from the state. For example, if one qubit is removed from the GHZ state, then the remaining qubits automatically become disentangled, which is why the overall entanglement of the GHZ state is equal to 1. If each qubit dephases at the rate *r*, then *N* qubits in GHZ states will dephase at the rate *Nr*, which is why the connectivity of the GHZ state is *N*. By contrast, for RVB states, there are *N*/2 singlets, so half of the qubits need to be removed to destroy entanglement. Similarly, this state is not markedly susceptible to dephasing, indicating a low value of connectivity.

Given that macroscopic entanglement exists, an important technological question is how easy this entanglement would be to extract and use. Suppose that two neutron beams are aimed at a magnetic substance, each at a different section[31]. It is fruitful — albeit not entirely mathematically precise — to think of this interaction as a state swap of the spins of the neutrons and the spins of the atoms in the solid. If the atoms in the solid are themselves entangled, then this entanglement is transferred to each of the scattered spins. This transferral could then presumably be used for further information processing. Similarly, schemes can be designed to extract entanglement from Bose–Einstein condensates[32,33] and superconductors[34] (which can be thought of as Bose–Einstein condensates of Cooper pairs of electrons), although none of these extraction schemes has been implemented as yet.

There are many open questions regarding entanglement. Here I have stated that, in theory, entanglement can exist in arbitrarily large and hot systems. But how true is this in practice? Another question is whether the entanglement of massless bodies fundamentally differs from that of massive ones[35]. Furthermore, does macroscopic entanglement also occur in living systems and, if so, is it used by these systems?

Some of the open questions might never be answered. Some might turn out to be uninteresting or irrelevant. One thing is certain though: current experimental progress is so rapid that future findings will surprise researchers and will take the current knowledge of entanglement to another level. ■

1. Amico, L., Fazio, R., Osterloh, A. & Vedral, V. Many-body entanglement. *Rev. Mod. Phys.* **80,** 517–576 (2008).
2. Osterloh, A. *et al.* Scaling of entanglement close to a quantum phase transition. *Nature* **416,** 608–610 (2002).
3. Osborne, T. J. & Nielsen, M. A. Entanglement in a simple quantum phase transition. *Phys. Rev. A* **66,** 032110 (2002).
4. Arnesen, M. C., Bose, S. & Vedral, V. Natural thermal and magnetic entanglement in 1D Heisenberg model. *Phys. Rev. Lett.* **87,** 017901 (2001).
5. Vedral, V. High temperature macroscopic entanglement. *New J. Phys.* **6,** 102 (2004).
6. Brukner, C., Vedral, V. & Zeilinger, A. Crucial role of entanglement in bulk properties of solids. *Phys. Rev. A* **73,** 012110 (2006).
7. Vedral, V. A better than perfect match. *Nature* **439,** 397 (2006).
8. Zeilinger, A., Weihs, G., Jennewein, T. & Aspelmeyer, M. Happy centenary, photon. *Nature* **433,** 230–238 (2005).
9. Einstein, A., Podolsky, B. & Rosen, N. Can quantum-mechanical description of physical reality be considered complete? *Phys. Rev.* **47,** 777–780 (1935).
10. Werner, R. F. Quantum states with Einstein–Podolsky–Rosen correlations admitting a hidden-variable model. *Phys. Rev. A* **40,** 4277–4281 (1989).
11. Brukner, C. & Vedral, V. Macroscopic thermodynamical witnesses of quantum entanglement. Preprint at <http://arxiv.org/abs/quant-ph/0406040> (2004).
12. Toth, G. & Guhne, O. Detecting genuine multipartite entanglement with two local measurements. *Phys. Rev. Lett.* **94,** 060501 (2004).
13. Narnhoffer, H. Separability for lattice systems at high temperature. *Phys. Rev. A* **71,** 052326 (2005).
14. Schrödinger, E. Die gegenwärtige Situation in der Quantenmechanik. *Naturwissenschaften* **23,** 807–812; 823–828; 844–849 (1935).
15. Horodecki, M., Horodecki, P. & Horodecki, R. Separability of mixed states: necessary and sufficient conditions. *Phys. Lett. A* **223,** 1–8 (1996).
16. Anders J. & Vedral, V. Macroscopic entanglement and phase transitions. *Open Sys. Inform. Dyn.* **14,** 1–16 (2007).
17. Horodecki, M. Entanglement measures. *Quant. Inform. Comput.* **1,** 3–26 (2001).
18. Vedral V. *et al.* Quantifying entanglement. *Phys. Rev. Lett.* **78,** 2275–2279 (1997).
19. Greenberger, D., Horne, M. A. & Zeilinger, A. in *Bell's Theorem, Quantum Theory, and Conceptions of the Universe* (ed. Kafatos, M.) 73–76 (Kluwer Academic, Dordrecht, 1989).
20. Dur, W., Vidal, G. & Cirac, J. I. Three qubits can be entangled in two inequivalent ways. *Phys. Rev. A* **62,** 062314 (2000).
21. Leggett, A. J. Macroscopic quantum systems and the quantum theory of measurement. *Prog. Theor. Phys. Suppl.* **69,** 80–100 (1980).
22. Anders, J. & Winter, A. Entanglement and separability of quantum harmonic oscillator systems at finite temperature. *Quant. Inform. Comput.* **8,** 0245–0262 (2008).
23. Vedral, V. Entanglement in the second quantisation formalism. *Cent. Eur. J. Phys.* **2,** 289–306 (2003).
24. Anderson, P. W. Resonating valence bonds: a new kind of insulator? *Mater. Res. Bull.* **81,** 53–60 (1973).
25. Raussendorf, R. & Briegel, H. J. A one-way quantum computer. *Phys. Rev. Lett.* **86,** 5188–5191 (2001).
26. Chandran, A., Kaszlikowski, D., Sen De, A., Sen, U. & Vedral, V. Regional versus global entanglement in resonating-valence-bond states. *Phys. Rev. Lett.* **99,** 170502 (2007).
27. Page, D. N. & Wootters, W. K. Evolution without evolution: dynamics described by stationary observables. *Phys. Rev. D* **27,** 2885–2892 (1983).
28. Haffner, H. *et al.* Scalable multiparticle entanglement of trapped ions. *Nature* **438,** 643–646 (2005).
29. Lu, C.-Y. *et al.* Experimental entanglement of six photons in graph states. *Nature Phys.* **3,** 91–95 (2007).
30. Baugh, J. *et al.* Quantum information processing using nuclear and electron magnetic resonance: review and prospects. Preprint at <http://arxiv.org/abs/0710.1447> (2007).
31. de Chiara, G. *et al.* A scheme for entanglement extraction from a solid. *New J. Phys.* **8,** 95 (2006).
32. Toth, G. Entanglement detection in optical lattices of bosonic atoms with collective measurements. *Phys. Rev. A* **69,** 052327 (2004).
33. Heaney, L., Anders, J., Kaszlikowski, D. & Vedral, V. Spatial entanglement from off-diagonal long-range order in a Bose–Einstein condensate. *Phys. Rev. A* **76,** 053605 (2007).
34. Recher, P. & Loss, D. Superconductor coupled to two Luttinger liquids as an entangler for spin electrons. *Phys. Rev. B* **65,** 165327 (2002).
35. Verstraete, F. & Cirac, J. I. Quantum nonlocality in the presence of superselection rules and data hiding protocols. *Phys. Rev. Lett.* **91,** 010404 (2003).

Acknowledgements I am grateful for funding from the Engineering and Physical Sciences Research Council, the Wolfson Foundation, the Royal Society and the European Union. My work is also supported by the National Research Foundation (Singapore) and the Ministry of Education (Singapore). I thank J. A. Dunningham, A. J. Leggett, D. Markham, E. Rieper, W. Son and M. Williamson for discussions of this and related subjects. W. Son's help with illustrations is also gratefully acknowledged.

Author Information Reprints and permissions information is available at npg.nature.com/reprints. The author declares no competing financial interests. Correspondence should be addressed to the author (vlatko.vedral@quantuminfo.org).

© 2008 Macmillan Publishers Limited. All rights reserved

NATURE|Vol 453|19 June 2008|doi:10.1038/nature07125

Entangled states of trapped atomic ions

Rainer Blatt[1,2] & David Wineland[3]

To process information using quantum-mechanical principles, the states of individual particles need to be entangled and manipulated. One way to do this is to use trapped, laser-cooled atomic ions. Attaining a general-purpose quantum computer is, however, a distant goal, but recent experiments show that just a few entangled trapped ions can be used to improve the precision of measurements. If the entanglement in such systems can be scaled up to larger numbers of ions, simulations that are intractable on a classical computer might become possible.

For more than five decades, quantum superposition states that are coherent have been studied and used in applications such as photon interferometry and Ramsey spectroscopy[1]. However, entangled states, particularly those that have been 'engineered' or created for specific tasks, have become routinely available only in the past two decades (see page 1004). The initial experiments with pairs of entangled photons[2,3], starting in the 1970s, were important because they provided tests of non-locality in quantum mechanics[4]. Then, in the early to mid-1980s, Richard Feynman and David Deutsch proposed that it might be possible way to carry out certain computations or quantum simulations efficiently by using quantum systems[5,6]. This idea was, however, largely considered a curiosity until the mid-1990s, when Peter Shor devised an algorithm[7] that could factor large numbers very efficiently with a quantum computer. This marked the beginning of widespread interest in quantum information processing[8] and stimulated several proposals for the implementation of a quantum computer.

Among these proposals, the use of trapped ions[9] has proved to be one of the most successful ways of deterministically creating entangled states, and for manipulating, characterizing and using these states for measurement. At present, about 25 laboratories worldwide are studying aspects of quantum information processing with trapped ions. Ions provide a relatively 'clean' system, because they can be confined for long durations while experiencing only small perturbations from the environment, and can be coherently manipulated. Although trapping ions in this way involves several technical processes, the system is an accessible one in which to test concepts that might be applicable to other systems, such as those involving neutral trapped atoms, quantum dots, nuclear spins, Josephson junctions or photons.

In this review, we highlight recent progress in creating and manipulating entangled states of ions, and we describe how these advances could help to generate quantum gates for quantum information processing and improve tools for high-precision measurement. For a review of earlier progress in quantum information processing with atoms, including atomic ions, and photons, see ref. 10.

Trapped and laser-cooled ions

To study entanglement, it is desirable to have a collection of quantum systems that can be individually manipulated, their states entangled, and their coherences maintained for long durations, while suppressing the detrimental effects of unwanted couplings to the environment. This can be realized by confining and laser cooling a group of atomic ions in a particular arrangement of electric and/or magnetic fields[11,12]. With such 'traps', atomic ions can be stored nearly indefinitely and can be localized in space to within a few nanometres. Coherence times of as long as ten minutes have been observed for superpositions of two hyperfine atomic states of laser-cooled, trapped atomic ions[13,14].

In the context of quantum information processing, a typical experiment involves trapping a few ions by using a combination of static and sinusoidally oscillating electric potentials that are applied between the electrodes of a linear quadrupole, an arrangement known as a Paul trap[12] (Fig. 1). When the trapped ions are laser cooled, they form a linear 'string', in which the spacings are determined by a balance between the horizontal (axial) confining fields and mutual Coulomb repulsion. Scattered fluorescence, induced by a laser beam, can be imaged with a camera (Fig. 1). The use of tightly focused laser beams allows the manipulation of individual ions.

For simplicity, in this review, we focus on two specific internal states of each ion, which we refer to as the ground and excited states ($|g\rangle$ and $|e\rangle$, respectively). This 'quantum bit' (qubit) structure is 'dressed' by the oscillator states $|n\rangle$ of frequency ω_{m} of a particular mode (Fig. 1). We denote the internal states as 'spin' states, in analogy to the two states of a spin −½ particle. If the energy between internal states corresponds to an optical frequency ω_{eg}, this atomic transition can be driven by laser radiation at frequency ω_{eg}, which couples states $|g, n\rangle \leftrightarrow |e, n\rangle$, where $|g, n\rangle$ denotes the combined state $|g\rangle|n\rangle$. Spin and motional degrees of freedom can be coupled by tuning the laser to 'sideband' frequencies $\omega_{eg} \pm \omega_{\mathrm{m}}$, which drives transitions $|g, n\rangle \leftrightarrow |e, n+\Delta n\rangle$ (refs 15–18), with $\Delta n = \pm 1$. In this case, state evolution can be described as a rotation $R_{\Delta n}(\theta, \phi)$ of the state vector on the Bloch sphere[8,18] and is defined here as

$$R_{\Delta n}(\theta, \phi)\,|g, n\rangle \rightarrow \cos\frac{\theta}{2}|g, n\rangle + ie^{i\phi}\sin\frac{\theta}{2}|e, n+\Delta n\rangle$$

$$R_{\Delta n}(\theta, \phi)\,|e, n+\Delta n\rangle \rightarrow ie^{-i\phi}\sin\frac{\theta}{2}|g, n\rangle + \cos\frac{\theta}{2}|e, n+\Delta n\rangle \quad (1)$$

where θ depends on the strength and the duration of the applied laser pulse, ϕ is the laser beam phase at the ion's position and $i = \sqrt{-1}$. For $\Delta n = \pm 1$, entanglement is generated between the spin and motional degrees of freedom. Higher-order couplings ($|\Delta n| > 1$) are suppressed for laser-cooled ions, the spatial extent of which is much smaller than the laser wavelength, which is known as the Lamb–Dicke regime. In this regime, sideband laser cooling works by tuning the laser to induce absorption on the lower sideband frequency ($\Delta n = -1$), followed by spontaneous emission decay, which occurs mainly at the 'carrier'

[1]Institut für Experimentalphysik, Universität Innsbruck, Technikerstrasse 25, A-6020 Innsbruck, Austria. [2]Institut für Quantenoptik und Quanteninformation, Österreichische Akademie der Wissenschaften, Otto-Hittmair-Platz 1, A-6020 Innsbruck, Austria. [3]National Institute of Standards and Technology, 325 Broadway, Boulder, Colorado 80305, USA.

© 2008 Macmillan Publishers Limited. All rights reserved

transition frequency ($\Delta n = 0$). With repeated absorption–emission cycles, the ions are optically pumped to the combined spin and motion ground state $|g, n=0\rangle$ (ref. 19). If the spin energy levels correspond to microwave or lower frequencies (as occurs in hyperfine atomic states and Zeeman states), the same processes can be realized by replacing single-photon optical transitions with two-photon stimulated-Raman transitions and by replacing spontaneous emission with spontaneous Raman scattering[15–18]. It should be noted that there are similarities between the coupling of an ion's internal states to the harmonic oscillator associated with a mode of motion and the case of cavity quantum electrodynamics, in which an atom's internal states are coupled to the harmonic oscillator associated with a single electromagnetic mode of the cavity (see page 1023).

The qubit state of an ion can be detected with more than 99% efficiency by measuring resonance fluorescence from an auxiliary state that is strongly coupled (by a monitoring excitation) to one of the qubit states ($|g\rangle$ or $|e\rangle$) and decays back only to that same state, known as a cycling transition. This is usually called quantum non-demolition (QND) detection because when the ion has been projected into a particular spin state, it will remain in that state throughout repeated excitation–emission cycles. Therefore, a cycle can be repeated many times, and it is not necessary to detect every emitted photon to obtain a high overall detection efficiency. If the qubit is projected to, or 'shelved' in, the state that is not coupled to the fluorescing transition, then no photons are observed, and this state can therefore be distinguished from the fluorescing state[20].

Spin-entangled states

In 1995, Ignacio Cirac and Peter Zoller suggested how to use a trapped-ion system to implement a quantum computer[9]. For universal quantum computing and for the generation of arbitrary entangled qubit states, two basic gate operations are required: first, individual qubit rotations as described by equation (1); and, second, a two-qubit-entangling operation that is the quantum counterpart to the classical operation with the XOR logic gate, the controlled-NOT (CNOT)-gate operation. The CNOT gate flips the state of a target qubit depending on the state of a control qubit. And, importantly, when applied to superposition states, it generates entanglement. The CNOT operation (Fig. 2) is achieved with a sequence of carrier pulses ($R_0(\theta, \phi)$) and red sideband pulses ($R_{-1}(\theta, \phi)$). The central part of this sequence involves a 'phase gate' that applies a phase shift $e^{i\pi} = -1$ to the $|g, n=1\rangle$ component of the target ion's wavefunction. This is implemented by applying a coherent $R_{-1}(2\pi, \phi)$ pulse between the $|g, 1\rangle$ state and an auxiliary state $|\text{aux}, 0\rangle$. Because the applied radiation cannot excite the states $|g, 0\rangle$, $|e, 0\rangle$ or $|e, 1\rangle$, they are unaffected. This operation is sandwiched between rotations that transfer phase changes into state changes, as occurs in Ramsey spectroscopy. By using a single ion, Christopher Monroe *et al.*[21] realized the CNOT operation between motion and spin for $^9Be^+$ ions. Subsequently, Ferdinand Schmidt-Kaler *et al.*[22,23] and later Mark Riebe *et al.*[24] realized the complete CNOT operation between two individually addressed $^{40}Ca^+$ ions. Entangling gates have also been realized by irradiating ions simultaneously (Fig. 3). Although such gates can be implemented in a single step, they still involve transitory entanglement with a motional mode, which effectively couples the spin qubits. Ions have also been entangled with each other in a probabilistic way mediated by entanglement with scattered photons[25] (Fig. 4).

By sequentially combining single-qubit and multiqubit operations, various entangled states of ions have been created deterministically or 'on demand'. A research group from the National Institute of Standards and Technology (NIST), in Boulder, Colorado, created[26] the state $|\Psi_e(\phi)\rangle = \frac{3}{5}|ge\rangle - e^{i\phi}\frac{4}{5}|eg\rangle$, where ϕ is a controllable phase factor and $|ge\rangle$ denotes the combined state $|g\rangle_1|e\rangle_2$ for ions 1 and 2. More generally, by using entangling operations and single-qubit rotations with adjustable phases, all Bell states — $|\Psi^{\pm}\rangle = \frac{1}{\sqrt{2}}(|ge\rangle \pm |eg\rangle)$, $|\Phi^{\pm}\rangle = \frac{1}{\sqrt{2}}(|gg\rangle \pm |ee\rangle)$ — and arbitrary superpositions can be generated[27,28]. The quality or fidelity of quantum states is usually characterized by the degree with which they agree with the desired (or ideal) state, which is expressed as

$$F = \langle \Psi_{\text{ideal}} | \rho_{\text{exp}} | \Psi_{\text{ideal}} \rangle \quad (2)$$

where ρ_{exp} is the experimentally achieved density matrix, which characterizes both pure and non-pure states. In current experiments, fidelities $F > 0.95$ are achieved.

In some cases, complete knowledge of the density matrix is not required. For example, the fidelity of a state relative to $|\Phi^+\rangle$ can be derived from just three matrix elements, $F = \frac{1}{2}(\rho_{gg,gg} + \rho_{ee,ee}) + \text{Re}\rho_{ee,gg}$, where $\rho_{ee,gg} \equiv \langle ee|\rho_{\text{exp}}|gg\rangle$ and so on and Re denotes the real part of the expression that follows. The matrix elements $\rho_{gg,gg}$ and $\rho_{ee,ee}$ are obtained from the measured populations of the respective states. The matrix element $\rho_{ee,gg}$

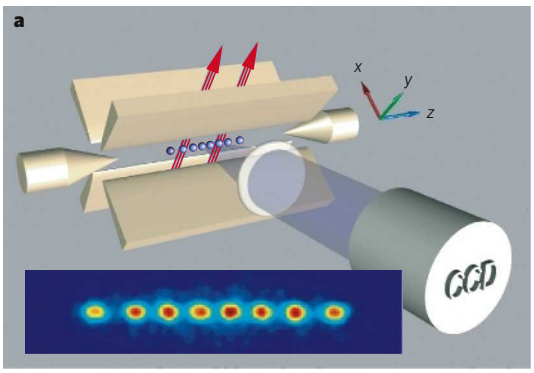

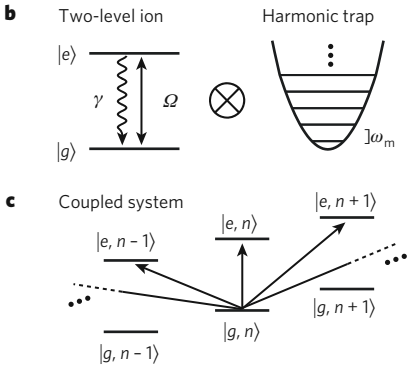

Figure 1 | Ions confined in a trap. a, A linear quadrupole ion trap (known as a Paul trap; beige) containing individually addressed $^{40}Ca^+$ ions (blue) is depicted. After cooling by laser beams (red), the trapped ions form a string and are then imaged by using a charge-coupled device (CCD). In the CCD image shown, the spacing of the two centre ions is ~8 μm. The electrode arrangement in the Paul trap provides an almost harmonic three-dimensional well. For a single ion, this is characterized by three frequencies[17]: ω_x, ω_y and ω_z, where x, y and z denote the confining potential axes. In this case, z points along the trap axis and x, y in the transverse directions. Owing to the Coulomb coupling that occurs between ions, the motion is best described in terms of normal modes; a string of ions can therefore be viewed as a pseudo-molecule. In general, the normal-mode frequencies ω_m differ from each other, and a particular mode can be accessed by spectral selection. **b**, The energy levels of a two-level ion (left) and one mode of the ion's motion (right) are shown. On the left is depicted the ion's ground state $|g\rangle$ and excited state $|e\rangle$, interacting with radiation characterized by the Rabi frequency Ω and decaying with the rate γ. On the right is depicted the harmonic oscillator potential and equally spaced energy levels for one mode of motion. Both the two-level system and the harmonic oscillator can be described jointly in a quantum-mechanical way, indicated by the direct product $\otimes$, resulting in a manifold of two-level systems separated by the mode frequency ω_m (as shown in **c**). **c**, The level structure of the coupled ion–harmonic-oscillator system is shown, with states jointly described by the spin ($|g\rangle$ and $|e\rangle$) and motional ($|0\rangle, |1\rangle, \ldots, |n\rangle$) degrees of freedom, where $|g\rangle|n\rangle = |g, n\rangle$ and $|e\rangle|n\rangle = |e, n\rangle$. Arrows indicate the transitions that are possible when appropriately tuned radiation is applied; dashed lines indicated connections to levels not shown.

© 2008 Macmillan Publishers Limited. All rights reserved

can be obtained by applying a rotation $R_0(\pi/2, \phi)$ to both ions and measuring the parity $P \equiv |gg\rangle\langle gg| + |ee\rangle\langle ee| - |ge\rangle\langle ge| - |eg\rangle\langle eg|$ of the resultant state as a function of ϕ. The only component of the parity that oscillates sinusoidally with frequency 2ϕ is proportional to $\rho_{ee,gg}$, which allows this element to be extracted[29].

As shown by equation (2), the fidelity can be obtained by measuring the full density matrix. To do this, the quantum state in question must be prepared many times; in this way, with the appropriate single-qubit rotations applied before the qubit measurements, all expectation values of the density matrix are obtained. Such a procedure is known as quantum-state tomography[28]. When this procedure is applied to Bell states, the density matrix can be completely characterized (Fig. 5). From the density matrices, all measures can subsequently be calculated. For example, in the case of Bell's inequalities, it is possible to determine the expectation value of the operator[30] $A = \sigma_x^{(1)} \otimes \sigma_{x-z}^{(2)} + \sigma_x^{(1)} \otimes \sigma_{x+z}^{(2)} + \sigma_z^{(1)} \otimes \sigma_{x-z}^{(2)} - \sigma_z^{(1)} \otimes \sigma_{x+z}^{(2)}$, where $\sigma_{x\pm z} = (\sigma_x \pm \sigma_z)/\sqrt{2}$ and σ is a Pauli operator and the superscripts refer to the first and second qubits. For local realistic theories, measurements of $|\langle A \rangle|$ are predicted to be less than 2, and values of $2 < |\langle A \rangle| < 2\sqrt{2}$ are expected for states that can be described only by quantum theory. With trapped ions, experiments yielded $|\langle A \rangle| = 2.25(3)$ at NIST[27], $|\langle A \rangle| = 2.52(6)$ at the Institute for Experimental Physics, University of Innsbruck (Innsbruck, Austria)[28], and $|\langle A \rangle| = 2.20(3)$ at the FOCUS Center and Department of Physics, University of Michigan (Ann Arbor, Michigan)[31], where the number in parentheses denotes the uncertainty in the last digit, clearly corroborating quantum theory (Fig. 5). Moreover, each time an experiment was run, a result was recorded. This closed the 'detection loophole', which would provide a way to violate Bell's inequalities within local realistic theories.

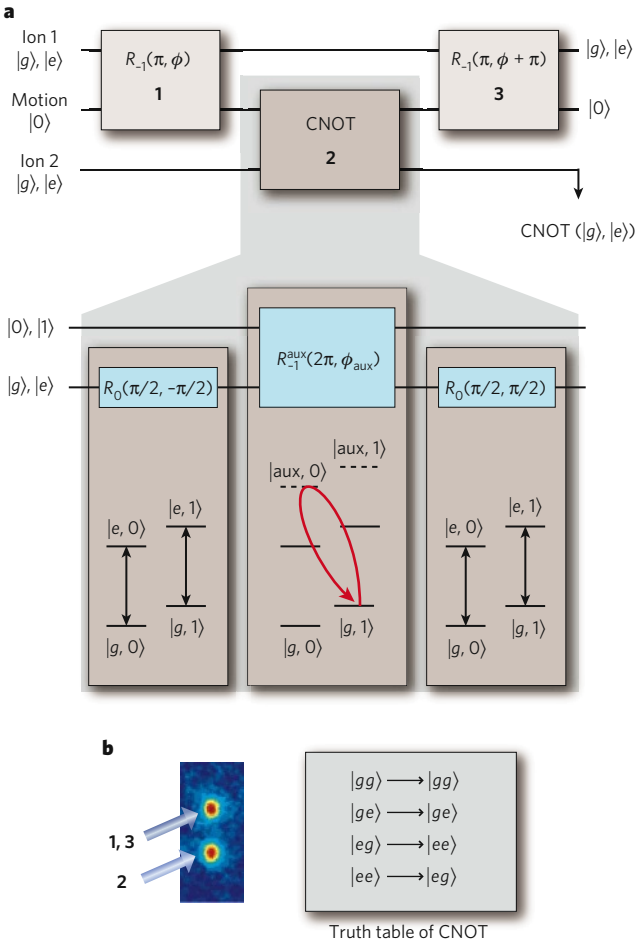

Figure 2 | A CNOT-gate operation with two trapped ions. a, Consider two ions in the same trap that are initially prepared in their motional ground state. In step 1, a lower-sideband pulse $R_{-1}(\pi, \phi)$ is applied to the first ion (ion 1; the control qubit) and maps the excited-state amplitude of this ion to the first excited state of a selected motional mode (a process known as a SWAP operation). Importantly, this motional excitation is also shared with the second ion (ion 2; the target qubit). In step 2, a CNOT-gate operation is implemented between the motion qubit (which is shared by both spin qubits) and the spin state of ion 2. Finally, in step 3, the first step is reversed, thereby restoring the initial spin state of ion 1 and returning the motion to its ground state. The pulse sequence of the CNOT-gate operation is also shown (lower part of **a**). **b**, On the left is a CCD image of two ions. The arrows indicate laser radiation that is applied to the ions in the order of the indicated numbers (which correspond to the three steps in **a**). First, a laser pulse is applied to the upper ion (1), then the CNOT sequence is applied to the lower ion (2). Finally, a laser pulse is applied to the upper ion again (3). On the right is the resultant truth table of the CNOT-gate operation, with the first and second symbols denoting the state of the control qubit (ion 1) and the target qubit (ion 2), respectively.

With trapped ions, cat states with $|\alpha| = |\beta|$ have been generated by using two approaches. At NIST, global entangling operations were used to demonstrate a cat state of four ions[29], a GHZ state with $F = 0.89$ (ref. 37), and cat states of up to six ions[38]. Using individually addressed ions and a CNOT-gate operation, the research group at Innsbruck produced GHZ states in an algorithmic way and analysed the states by using tomographic measurements[39]. In a similar way, the Innsbruck group also produced W states for N-ion qubits, $|\Psi_W\rangle = \frac{1}{\sqrt{N}}(|g \ldots gge\rangle + |g \ldots geg\rangle + \ldots + |eg \ldots g\rangle)$, which belong to a different class of entangled states. Such classes are distinct because states of different classes cannot be transformed into each other by local operations and classical communication[40]. Nevertheless, both cat and W states can violate Bell-type inequalities. In contrast to cat states, W states are remarkably robust in the face of a variety of decoherence processes: for W states, even the loss of qubits does not destroy entanglement completely. The Innsbruck group deterministically prepared an eight-qubit W state[41] by using individual ion addressing. Both the NIST and Innsbruck groups verified multipartite entanglement by using an 'entanglement witness', an operator constructed so that its expectation value must exceed (or be less than) a certain value to verify N-particle entanglement[38,41].

Demonstrating quantum-information-processing algorithms

Algorithms are lists of instructions for completing a task[8]. As is the case in classical computation, quantum algorithms can sometimes be viewed as subroutines in a larger computation. A quantum-information-processing algorithm generally involves single-qubit gates and multiqubit gates, as well as measurements and measurement-dependent operations. The result of such a sequence of operations could be a deterministically prepared quantum state (such as a Bell, GHZ or W state), a conditioned state (such as an error-corrected state) or a state that is subsequently inferred from a measurement of the quantum register and is then available as classical information.

In contrast to classical information processing, quantum information processing allows tests to be carried out using superpositions. A simple example showing the gain in efficiency that is possible with a quantum algorithm was proposed by Deutsch and Richard Jozsa[42]. The Deutsch–Jozsa algorithm was first demonstrated with two qubits in nuclear magnetic resonance spectroscopy[43], and it was demonstrated more recently with a trapped ion[44], with the motional and spin properties of the ion qubit serving as the two qubits.

© 2008 Macmillan Publishers Limited. All rights reserved

Another example algorithm is teleportation of the state of one qubit to another qubit, an important protocol for the transfer of quantum information[10,45]. In this algorithm, Alice wants to send a qubit state (which, in general, is unknown) to Bob. To do this, a Bell pair is generated, and one qubit from this pair is given to the sender, Alice, and the other qubit to the receiver, Bob. When the unknown state is ready to be teleported, it is entangled with Alice's qubit of the Bell pair. A subsequent measurement of both qubits by Alice yields two bits of classical information that she sends to Bob. With this information, Bob knows which of four possible rotations to apply to his qubit to obtain Alice's original unknown state.

Deterministic quantum teleportation has been demonstrated by the NIST[46] and Innsbruck[47] groups. The Innsbruck group used individual laser-beam addressing of three qubits; therefore, the state was teleported from one end of the ion string to the other end, a distance of ~10 μm. The NIST group used a multizone linear-trap array. By applying control potentials to electrode segments, the ions could be separated and moved in and out of one zone in which the laser beams were present. In this case, the state was teleported across a few hundred micrometres.

Teleportation is an important building block for quantum information processing and can reduce the computational resource requirements. Furthermore, it is the basic procedure for quantum communication protocols, such as for implementing quantum repeaters. Other algorithms — such as entanglement purification[48], quantum error correction[49], the quantum Fourier transform[50] and deterministic entanglement swapping (M. Riebe, T. Monz, K. Kim, A. S. Villar, P. Schindler, M. Chwalla, M. Hennrich and R. Blatt, unpublished observations) — have also been demonstrated with ion qubits.

These experiments demonstrate the basic features of quantum algorithms, but for the concatenation of processes and repeated computations, improved operation fidelities will be required. In particular, full and repetitive implementation of quantum error correction, which could keep a qubit superposition 'alive' while subjected to decoherence, remains a major challenge in quantum information processing.

Applications

In the mid-1990s, a wave of interest in potential applications for quantum information processing was generated by Shor's period-finding algorithm for factoring large numbers[7]. Another noteworthy potential application is the implementation of unstructured searches[51]. However, to be of practical use, these applications require substantial resources in terms of the number of qubits and the number of operations, far beyond the capabilities of current implementations. Despite this, some elements of quantum information processing and entanglement with small numbers of qubits are beginning to find applications in metrology. Many physicists also expect that useful quantum simulations will be carried out on a relatively small number of qubits, perhaps up to 100, in the next decade.

One application in metrology is to improve interferometry. As an example, we discuss how entanglement can be applied to Ramsey spectroscopy[52], but this scheme has a direct analogue in electron, atom and photon Mach–Zehnder interferometry. Ramsey spectroscopy on the $|g\rangle \rightarrow |e\rangle$ transition proceeds as follows. The atom is first prepared in the state $|\Psi_{\text{initial}}\rangle = |g\rangle$. Radiation at frequency ω near ω_{eg} is applied in a fast pulse to produce the state $R_0(\pi/2, -\pi/2)|g\rangle = \frac{1}{\sqrt{2}}(|g\rangle + |e\rangle)$. The atom is now allowed to evolve for a duration T so that the atom's upper state accumulates a phase $\phi_R = (\omega - \omega_{ge})T$ relative to the lower state (when the problem is viewed in a frame that rotates at frequency ω). Finally, again, a rotation $R_0(\pi/2, -\pi/2)$ is applied and leaves the atom in the state (up to a global phase factor) $|\Psi_{\text{final}}\rangle = \sin(\phi_R/2)|g\rangle + i\cos(\phi_R/2)|e\rangle$. Therefore, the probability of finding the atom in the state $|e\rangle$ is $p_e = \frac{1}{2}(1 + \cos[(\omega - \omega_{ge})T])$. For an ensemble of N atoms, the detected signal will be Np_e. In precision spectroscopy, the idea is to detect changes in $\omega - \omega_{ge}$ or ϕ_R, as observed through changes in p_e. Therefore, the N-ion signal can be defined as $S = \mathrm{d}(Np_e)/\mathrm{d}\phi_R = -N/2\sin(\phi_R)$. The fundamental noise in the signal is given by the 'projection noise': that is, the fluctuation in the number of atoms, from experiment to experiment, that is measured to be in the state $|e\rangle$ (ref. 53). The variance of this noise is given by $V_N = Np_e(1 - p_e)$, so the magnitude of the signal-to-noise ratio is equal to $S/\sqrt{V_N} = \sqrt{N}$, essentially the shot noise corresponding to the number of atoms.

Now, suppose that the first $R_0(\pi/2, -\pi/2)$ pulse can be replaced with an entangling $\pi/2$ pulse[37,38], which creates the cat state

$$|g\rangle_1|g\rangle_2 \ldots |g\rangle_N \rightarrow \tfrac{1}{\sqrt{2}}(|g\rangle_1|g\rangle_2 \ldots |g\rangle_N + |e\rangle_1|e\rangle_2 \ldots |e\rangle_N) \equiv \tfrac{1}{\sqrt{2}}(|g_N\rangle + |e_N\rangle) \qquad (3)$$

After a delay T, the $|e_N\rangle$ state accumulates a phase $N\phi_R$ relative to the $|g_N\rangle$ state. A final entangling $\pi/2$ pulse leaves the atoms in a superposition state $\sin(N\phi_R/2)|g_N\rangle + i\cos(N\phi_R/2)|e_N\rangle$; therefore, the probability of detecting the atoms in the $|e_N\rangle$ state is $p_{N_e} = \frac{1}{2}(1 + \cos[N(\omega - \omega_{ge})T])$. It is as though spectroscopy has been carried out on a single 'super-atom' composed of states $|e_N\rangle$ and $|g_N\rangle$. The super-atom has a resonant frequency that is N times higher than that of a single atom, as well as a phase sensitivity (to the Nth harmonic of the applied radiation) that is N times higher. The resultant gain in interferometric sensitivity must, however, be offset by the fact that only a single-particle two-state system ($|e_N\rangle$ and $|g_N\rangle$) is being measured. Nevertheless, after a statistically significant number of repeated measurements, the sensitivity is

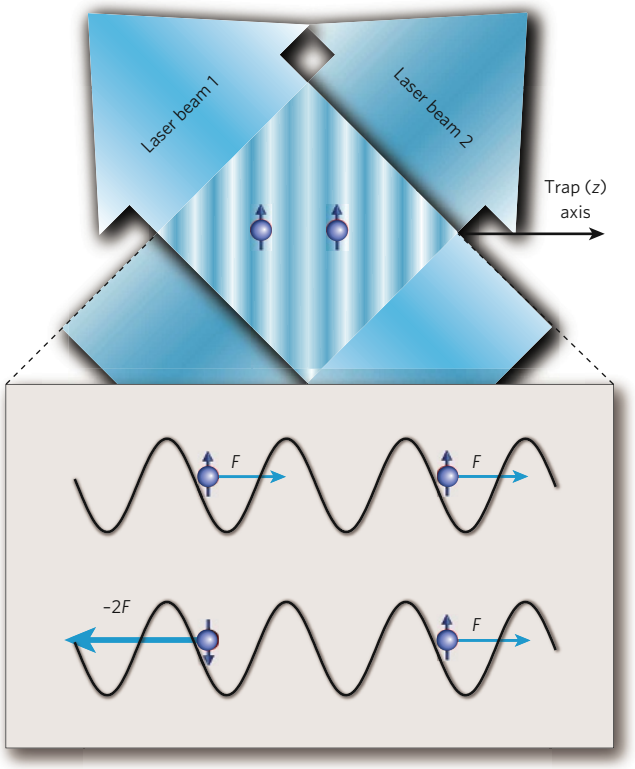

Figure 3 | A two-qubit phase gate. A phase gate with two ions (blue) is depicted. The operation of such phase gates relies on the fact that when a selected mode of the ions' motion is displaced in phase space about a closed path, the ions' wavefunction picks up a phase that is proportional to the enclosed area. If this displacement depends on the ions' qubit states, then entanglement is generated[92–95]. This state-dependent displacement can be implemented by applying optical dipole forces (F) by using laser-beam intensity gradients. In this example, an intensity standing wave is created with two laser beams, and the horizontal spacing of the ions is made to be an integral number of wavelengths of the intensity pattern. The pattern sweeps across the ions at the difference between the frequencies of the beams, chosen to be near the stretch-mode frequency. If the ions' qubit states $|g\rangle$ and $|e\rangle$ feel different dipole forces, then only the $|ge\rangle$ and $|eg\rangle$ components of the ions' wavefunction are displaced in phase space. By making the trajectories closed and by choosing the size of the displacements appropriately, the wavefunction is unchanged except for an $e^{i\pi/2}$ phase shift on the $|ge\rangle$ and $|eg\rangle$ states, the desired phase gate. Such gate operations have been implemented with trapped $^9Be^+$ ions[29,95] and in a similar way with $^{111}Cd^+$ ions[96] and $^{40}Ca^+$ ions[63,97].

© 2008 Macmillan Publishers Limited. All rights reserved

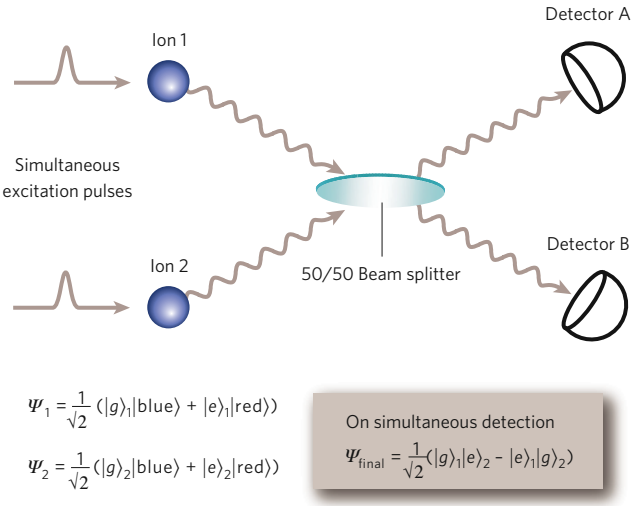

Figure 4 | Entanglement produced by conditional measurements. Entanglement can be created between two separated particles by an interference effect and state projection accompanying a measurement. In this example[25], it is assumed that the qubits of two ions (blue) are encoded in hyperfine levels of the electronic ground states. These qubits are first prepared in superposition states $\frac{1}{\sqrt{2}}(|g\rangle + |e\rangle)$. When excited with laser pulses that are short enough that both qubits simultaneously undergo (single-photon) scattering, the frequencies (denoted 'red' and 'blue') of the emitted photons along a particular direction are correlated with the qubit states, as indicated for entangled states $|\Psi_1\rangle$ and $|\Psi_2\rangle$. These photons can be simultaneously sent into a 50/50 beam splitter and then detected. In the cases when photons are simultaneously detected at detector A and detector B, the ions are projected into the Bell state $|\Psi_{\text{final}}\rangle$, even though the atoms have not directly interacted. For many such experiments, photons do not reach either detector; however, when photons are simultaneously detected, this 'heralds' the formation of the entangled state $|\Psi_{\text{final}}\rangle$, which can then be saved and used later, such as in Bell's inequality measurements of remotely located ions[98]. One potential use of this scheme is for entanglement-assisted communication between ion locations 1 and 2.

increased by a factor of $\sqrt{N}$ by using entangling $\pi/2$ pulses compared with the case of N unentangled atoms[36–38]. Because of technical noise in the experiments, this theoretical improvement is not fully realized; however, a gain in sensitivity compared with the case of unentangled atoms has been realized for up to six entangled ions[38,54,55].

These arguments assume that noise results only from state projection. In experiments, if there is correlated decoherence of qubit phases, then any gain in sensitivity may be lost as a result of the faster decoherence of the cat states[56] or as a result of noise in the oscillator that produces the radiation[18,57]. If these sources of noise can be suppressed, entangled states should be able to improve the signal-to-noise ratio in future spectroscopy experiments.

Another application of quantum-information-processing techniques is increased fidelity of detection[58]. This can be useful if the qubit does not have a cycling transition or if the QND aspect of the shelving detection is not well satisfied. A simple implementation is to assume that there are two qubits, labelled q and d, stored in the same trap. The goal is to detect the state of information qubit q, by using detection qubit d. Before any measurements are taken, qubit q will generally be in a superposition state $\alpha|g\rangle_q + \beta|e\rangle_q$. Using the SWAP operations of the Cirac–Zoller gate, this superposition is first transferred to the qubit composed of the $|0\rangle$ and $|1\rangle$ states of a selected motional mode, and is then mapped to qubit d. Then, qubit d is measured, thereby in effect measuring qubit q. This protocol can be carried out without disturbing the initial probabilities $|\alpha|^2$ and $|\beta|^2$ for qubit q, even if the mapping steps are imperfect. Therefore, it is a QND measurement and can be repeated to increase detection efficiency. This scheme was demonstrated in an experiment[59] in which qubit q was based on an optical transition in a $^{27}Al^+$ ion and qubit d was based on a hyperfine transition in a $^9Be^+$ ion. In that experiment, a single round of detection had a fidelity of only $F = 0.85$; however, by repeating the measurement, and by using real-time bayesian analysis, the fidelity was improved to $F = 0.9994$. It should be noted that this strategy can also be used to prepare an eigenstate of qubit q with high fidelity. In addition to this demonstration, this protocol is now used in a high-accuracy optical clock based on single $^{27}Al^+$ ions[60]. This technique has also been extended so that a single detection qubit can be used to measure the states of multiple ions[59], similar to the measurement of the Fock states of photons by using multiple probe atoms[61].

Finally, entanglement can be used in metrology to create states that allow the measurement of certain parameters while suppressing sensitivity to others. This strategy has been used, for example, to make a precise measurement of the quadrupole moment of a $^{40}Ca^+$ ion by carrying out spectroscopy on an entangled state of two ions that depended on the quadrupole moment but was insensitive to fluctuations in the magnetic field[62].

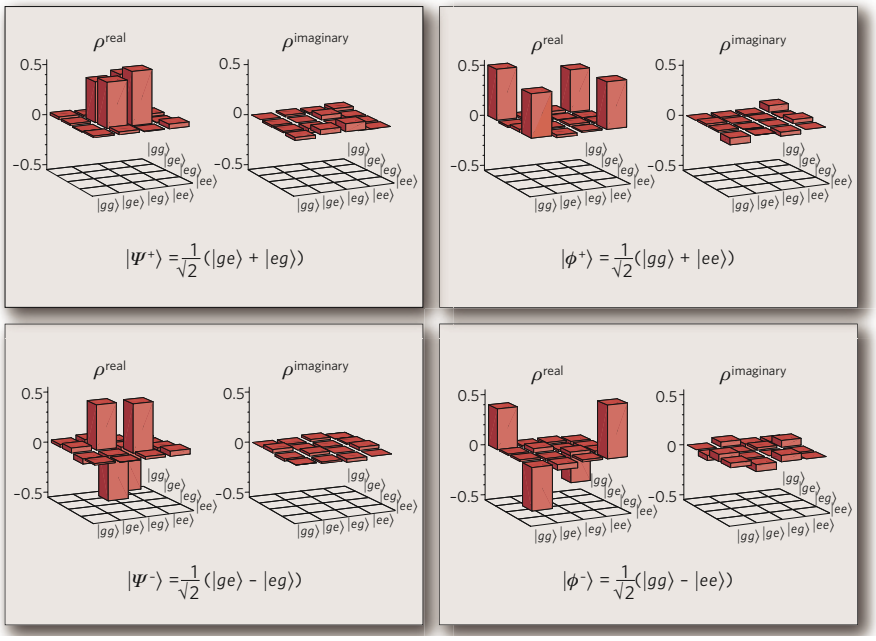

Figure 5 | Measured density matrices of Bell states. The real (left) and imaginary (right) parts of the density matrices obtained for the Bell states $|\Psi^+\rangle$ (upper left), $|\Psi^-\rangle$ (lower left), $|\phi^+\rangle$ (upper right) and $|\phi^-\rangle$ (lower right) prepared deterministically with two trapped $^{40}Ca^+$ ions are shown. The states were analysed by using quantum-state tomography, a technique that provides all of the necessary information to reconstruct the corresponding density matrix[8]. More specifically, the density matrix for a single qubit can be represented by $\rho = \frac{1}{2}(I + \Sigma_i \langle\sigma_i\rangle \sigma_i)$, where σ_i is a Pauli matrix, $i = x, y, z$ and I is the identity matrix. Measurements project a qubit onto its energy eigenstates, which is equivalent to measuring $\langle\sigma_z\rangle$. To determine $\langle\sigma_{x,y}\rangle$, an additional rotation of the Bloch sphere is applied before the measurement. The tomography procedure can be extended to N qubits, requiring of the order of 4^N expectation values to be measured. Owing to statistical errors, the experimentally measured expectation values can result in unphysical elements in the density matrix (with negative eigenvalues). This outcome is avoided by fitting the measured expectation values by using a maximum-likelihood method and then finding the most likely density matrix that describes the state[28].

© 2008 Macmillan Publishers Limited. All rights reserved

Prospects

Although the basic elements of quantum computation have been demonstrated with atomic ions, operation errors must be significantly reduced and the number of ion qubits must be substantially increased if quantum computation is to be practical. Nevertheless, before fidelities and qubit numbers reach those required for a useful factoring machine, worthwhile quantum simulations might be realized.

More ion qubits and better fidelity

To create many-ion entangled states, there are two important goals: improving gate fidelity, and overcoming the additional problems that are associated with large numbers of ions. For fault-tolerant operation, a reasonable guideline is to assume that the probability of an error occurring during a single gate operation should be of the order of 10^{-4} or lower. An important benchmark is the fidelity of two-qubit gates. The best error probability achieved so far is approximately 10^{-2}, which was inferred from the fidelity of Bell-state generation[63]. In general, it seems that gate fidelities are compromised by limited control of classical components (such as fluctuations in the laser-beam intensity at the positions of the ions) and by quantum limitations (such as decoherence caused by spontaneous emission)[64]. These are daunting technical problems; however, eventually, with sufficient care and engineering expertise, these factors are likely to be suppressed.

The multiqubit operations discussed in this review rely on the ability to isolate spectrally a single mode of the motion of an ion. Because there are $3N$ modes of motion for N trapped ions, as N becomes large, the mode spectrum becomes so dense that the gate speeds must be significantly reduced to avoid off-resonance coupling to other modes. Several proposals have been put forward to circumvent this problem[65,66]. Alternatively, a way to solve this problem with gates that have been demonstrated involves distributing the ions in an array of multiple trap zones[18,67–69] (Fig. 6a). In this architecture, multiqubit gate operations could be carried out on a relatively small number of ions in multiple processing zones. Entanglement could be distributed between these zones by physically moving the ions[18,68,69] or by optical means[25,67,70–72]. For quantum communication over large distances, optical distribution seems to be the only practical choice; for experiments in which local entanglement is desirable, moving ions is also an option.

Examples of traps that could be used for scaling up the number of ions used in an algorithm are shown in Fig. 6b. Ions can be moved between zones by applying appropriate control electric potentials to the various electrode segments[46,73–75]. Individual ions have been moved ~1 mm in ~50 μs without loss of coherence; the excitation of the ion's motion (in its local well) was less than one quantum[73]. Multiple ions present in a single zone can be separated[46,73] by inserting an electric potential 'wedge' between the ions. In the teleportation experiment by the NIST group[46], two ions could be separated from a third in ~200 μs, with negligible excitation of the motional mode used for subsequent entangling operations between the two ions. This absence of motional excitation meant that an additional entangling-gate operation on the separated ions could be implemented with reasonable fidelity. For algorithms that operate over long time periods, the ions' motion will eventually become excited as a result of transportation and background noise from electric fields. To counteract this problem, additional laser-cooled ions could be used to cool the qubits 'sympathetically' (Fig. 6a). These 'refrigerator' ions could be identical to the qubit ions[76], of a different isotope[77] or of a different species[60,78]. They could also aid in detection and state preparation (described earlier).

For all multiqubit gates that have been implemented so far, the speeds are proportional to the frequencies of the modes of the ions, which scale as $1/d_{qe}^2$, where d_{qe} is the distance of the ion to the nearest electrode. Therefore, it would be valuable to make traps as small as possible. Many groups have endeavoured to achieve this, but they have all observed significant heating of the ions, compromising gate fidelity. The heating is anomalously large compared with that expected to result from thermal noise, which arises from resistance in, or coupled to, the trap electrodes[18,79–83]. It scales approximately as $1/d_{qe}^4$ (refs 18, 79–83), which is consistent with the presence of independently fluctuating potentials on electrode patches, the extent of which is small compared with d_{qe} (ref. 79). The source of the heating has yet to be understood, but recent experiments[80,82] indicate that it is thermally activated and can be significantly suppressed by operating at low temperature.

For large trap arrays, a robust means of fabrication will be required, as well as means of independently controlling a very large number of electrodes. Microelectromechanical systems (MEMS) fabrication technologies can be used for monolithic construction[83,84], and trap structures can be further simplified by placing all electrodes in a plane[84,85]. To mitigate the problem of controlling many electrodes, it might be possible to incorporate 'on-board' electronics close to individual trap zones[86]. Laser beams must also be applied in several locations simultaneously, because it will be essential to carry out parallel operations when implementing complex algorithms. The recycling of laser beams can be used[86,87], but the overall laser power requirements will still increase. If gates are implemented by using stimulated-Raman transitions, then a

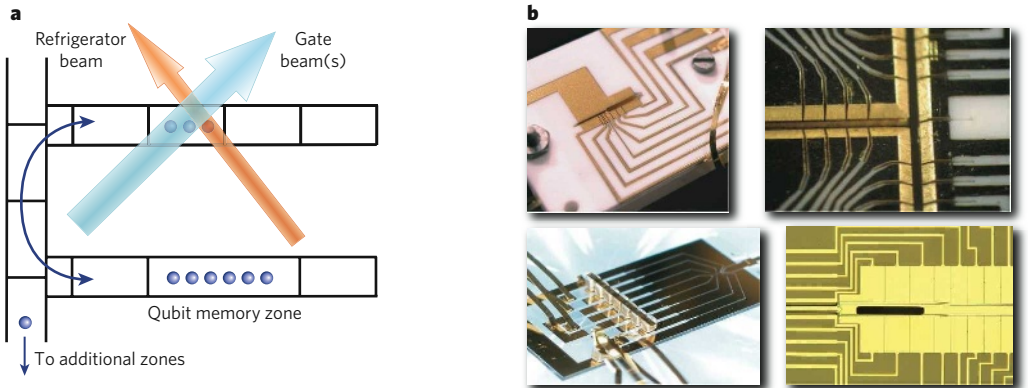

Figure 6 | Multizone trap arrays. a, A schematic representation of a multizone trap array is shown. Each control electrode is depicted as a rectangle. Ions (blue circles) can be separated and moved to specific zones, including a memory zone, by applying appropriate electrical potentials. Because the ions' motion will become excited as a result of transport (bidirectional arrow) and noisy ambient electric fields, refrigerator ions (red; which are cooled by the red laser beam) are used to cool the ions before gate operations, which are implemented with the blue laser beam. **b**, Examples of the electrode configurations of trap arrays are shown. In the upper left is a two-layer, six-zone linear trap in which entangled ions can be separated and used for algorithm demonstrations, including teleportation[46] (width of narrow slot (where the ions are located) = 200 μm). In the upper right is a three-layer, two-dimensional multizone trap that can be used to switch ion positions[99] (width of slot = 200 μm). In the lower left is a single-zone trap in which all of the electrodes lie in a single layer; this design considerably simplifies fabrication[85]. In the lower right is a single-layer, linear multizone trap fabricated on silicon (width of open slot for loading ions ≃ 95 μm), which can enable electronics to be fabricated on the same substrate that contains the trap electrodes. (Image courtesy of R. Slusher, Georgia Tech Research Institute, Atlanta).

© 2008 Macmillan Publishers Limited. All rights reserved

high laser-beam intensity will also be needed to suppress spontaneous emission decoherence to fault-tolerant levels[64]. Detection will also need to be implemented simultaneously in several locations. This issue might be resolved by coupling on-board detectors or other forms of miniature integrated optics to optical fibres.

Future applications

In the early 1980s, Feynman suggested that one quantum system could perhaps be used to simulate another[5]. This simulation could be accomplished efficiently with a large-scale quantum computer. But before this goal is reached, it might be possible to take advantage of the fact that current logic gates are implemented by hamiltonians that can be used to simulate interactions in other systems. A simple example was mentioned earlier in the discussion of spectroscopy with cat states; these experiments simulate the action of electron, photon and atom Mach–Zehnder interferometers that incorporate entangling beam splitters[55]. A more interesting prospect is that the gate hamiltonians might be applied in a strategic way to simulate specific many-body hamiltonians. The basic idea can be considered by noting that the two-ion phase gate (Fig. 3) can be written in the form $R_{Z1}R_{Z2}e^{-i\xi\sigma_{z1}\sigma_{z2}}$, where R_{Z1} and R_{Z2} are rotations about the z axis and ξ is the strength of coupling. Therefore, up to an overall rotation on the qubits, the gate implements the hamiltonian $H=\hbar\kappa\sigma_{z1}\sigma_{z2}$, a spin–spin interaction between the two addressed spins, where κ is the strength of the interaction and $\hbar$ is $h/2\pi$ (and h is Planck's constant). By extending these couplings to many ion qubits in an ensemble, Ising-type spin hamiltonians could, for example, be implemented[88–91]. The interactions between ion pairs could be applied in a stepwise manner but might also be implemented simultaneously, thereby increasing efficiency. Although simulating specific many-body hamiltonians is a challenge given current experimental capabilities, even with a relatively small number of ions, interesting phenomena such as quantum phase transitions might be observable.

Conclusion

As researchers progress towards generating a large-scale quantum-information-processing device, it might be possible to shed light on more fundamental issues of decoherence and why many-particle states with the quantum attributes of Schrödinger's cat are not observed. If it is possible to continue scaling up such devices to a large size, the issue of the absence of cat states becomes more pressing. For example, suppose that, in the future, large-N-qubit cat states in the form of equation (3) can be made. Then, this cat state for N qubits can be rewritten as $|\Psi\rangle=\frac{1}{\sqrt{2}}(|g\rangle_j\pi_{k\neq j}^N|g\rangle_k+|e\rangle_j\pi_{k\neq j}^N|e\rangle_k)$, where the jth qubit has been (arbitrarily) singled out and k represents the other qubits. For large N, this wavefunction has the attributes of Schrödinger's cat in the sense that the states of a single two-level quantum system (the jth qubit) are correlated with states that have macroscopically distinct polarizations. If generating such states is successful, then the existence of, in essence, Schrödinger's cats will have been shown. Such states are, however, more sensitive to the effects of phase decoherence[56], but this seems to be a technical, not a fundamental, problem. Therefore, if it becomes impossible to make such states or to build a large-scale quantum computer for non-technical reasons, this failure might indicate some new physics. ■

1. Ramsey, N. F. *Molecular Beams* (Clarendon, London, 1956).
2. Freedman, S. F. & Clauser, J. F. Experimental test of local hidden-variable theories. *Phys. Rev. Lett.* **28,** 938–941 (1972).
3. Aspect, A., Grangier, P. & Roger, G. Experimental tests of realistic local theories via Bell's theorem. *Phys. Rev. Lett.* **47,** 460–463 (1981).
4. Bell, J. S. *Speakable and Unspeakable in Quantum Mechanics* (Cambridge Univ. Press, Cambridge, UK, 1987).
5. Feynman, R. P. Simulating physics with computers. *Int. J. Theoret. Phys.* **21,** 467–468 (1982).
6. Deutsch, D. Quantum theory, the Church–Turing principle and the universal quantum computer. *Proc. R. Soc. Lond. A* **400,** 97–117 (1985).
7. Shor, P. W. Algorithms for quantum computation: discrete logarithms and factoring. In *Proc. Annu. Symp. Found. Comput. Sci.* 124–134 (1994).
8. Nielsen, M. A. & Chuang, I. L. *Quantum Computation and Quantum Information* (Cambridge Univ. Press, Cambridge, UK, 2000).
9. Cirac, J. I. & Zoller, P. Quantum computations with cold trapped ions. *Phys. Rev. Lett.* **74,** 4091–4094 (1995).
10. Monroe, C. Quantum information processing with atoms and photons. *Nature* **416,** 238–246 (2002).
11. Dehmelt, H. Experiments with an isolated subatomic particle at rest. *Rev. Mod. Phys.* **62,** 525–530 (1990).
12. Paul, W. Electromagnetic traps for charged and neutral particles. *Rev. Mod. Phys.* **62,** 531–540 (1990).
13. Bollinger, J. J., Heinzen, D. J., Itano, W. M., Gilbert, S. L. & Wineland, D. J. A 303-MHz frequency standard based on trapped $^9Be^+$ ions. *IEEE Trans. Instrum. Meas.* **40,** 126–128 (1991).
14. Fisk, P. T. H. *et al.* Very high q microwave spectroscopy on trapped $^{171}Yb^+$ ions: application as a frequencystandard. *IEEE Trans. Instrum. Meas.* **44,** 113–116 (1995).
15. Blatt, R., Häffner, H., Roos, C., Becher, C. & Schmidt-Kaler, F. in *Quantum Entanglement and Information Processing: Les Houches Session LXXIX* (eds Estève, D. Raimond, J.-M. & Dalibard, J.) 223–260 (Elsevier, Amsterdam, 2004).
16. Wineland, D. J. in *Quantum Entanglement and Information Processing: Les Houches Session LXXIX* (eds Estève, D. Raimond, J.-M. & Dalibard, J.) 261–293 (Elsevier, Amsterdam, 2004).
17. Leibfried, D., Blatt, R., Monroe, C. & Wineland, D. Quantum dynamics of single trapped ions. *Rev. Mod. Phys.* **75,** 281–324 (2003).
18. Wineland, D. J. *et al.* Experimental issues in coherent quantum-state manipulation of trapped atomic ions. *J. Res. Natl Inst. Stand. Technol.* **103,** 259–328 (1998).
19. Diedrich, F., Bergquist, J. C., Itano, W. M. & Wineland, D. J. Laser cooling to the zero-point energy of motion. *Phys. Rev. Lett.* **62,** 403–406 (1989).
20. Dehmelt, H. G. Mono-ion oscillator as potential ultimate laser frequency standard. *IEEE Trans. Instrum. Meas.* **31,** 83–87 (1982).
21. Monroe, C., Meekhof, D. M., King, B. E., Itano, W. M. & Wineland, D. J. Demonstration of a fundamental quantum logic gate. *Phys. Rev. Lett.* **75,** 4714–4717 (1995).
22. Schmidt-Kaler, F. *et al.* Realization of the Cirac–Zoller controlled-NOT quantum gate. *Nature* **422,** 408–411 (2003).
23. Schmidt-Kaler, F. *et al.* How to realize a universal quantum gate with trapped ions. *Appl. Phys. B* **77,** 789–796 (2003).
24. Riebe, M. *et al.* Process tomography of ion trap quantum gates. *Phys. Rev. Lett.* **97,** 220407 (2006).
25. Moehring, D. L. *et al.* Entanglement of single-atom quantum bits at a distance. *Nature* **449,** 68–71 (2007).
26. Turchette, Q. A. *et al.* Deterministic entanglement of two trapped ions. *Phys. Rev. Lett.* **81,** 3631–3634 (1998).
27. Rowe, M. A. *et al.* Experimental violation of a Bell's inequality with efficient detection. *Nature* **409,** 791–794 (2001).
28. Roos, C. F. *et al.* Bell states of atoms with ultralong life times and their tomographic state analysis. *Phys. Rev. Lett.* **92,** 220402 (2004).
29. Sackett, C. A. *et al.* Experimental entanglement of four particles. *Nature* **404,** 256–259 (2000).
30. Clauser, J. F., Horne, M. A., Shimony, A. & Holt, R. A. Proposed experiment to test local hidden-variable theories. *Phys. Rev. Lett.* **23,** 880–884 (1969).
31. Moehring, D. L., Madsen, M. J., Blinov, B. B. & Monroe, C. Experimental Bell inequality violation with an atom and a photon. *Phys. Rev. Lett.* **93,** 090410 (2004).
32. Schrödinger, E. Die gegenwärtige Situation in der Quantenmechanik. *Naturwissenschaften* **23,** 807–812 (1935).
33. Greenberger, D. M., Horne, M. A. & Zeilinger, A. in *Going Beyond Bell's Theorem* (ed. Kafatos, M.) 69–72 (Kluwer Academic, Dordrecht, 1989).
34. DiVincenzo, D. P. & Shor, P. W. Fault-tolerant error correction withefficient quantum codes. *Phys. Rev. Lett.* **77,** 3260–3263 (1996).
35. Steane, A. M. Error correcting codes in quantum theory. *Phys. Rev. Lett.* **77,** 793–797 (1996).
36. Bollinger, J. J., Itano, W. M., Wineland, D. J. & Heinzen, D. J. Optimal frequency measurements with maximally correlated states. *Phys. Rev. A* **54,** R4649–R4652 (1996).
37. Leibfried, D. *et al.* Toward Heisenberg-limited spectroscopy with multiparticle entangled states. *Science* **304,** 1476–1478 (2004).
38. Leibfried, D. *et al.* Creation of a six-atom 'Schrödinger cat' state. *Nature* **438,** 639–642 (2005).
39. Roos, C. F. *et al.* Control and measurement of three-qubit entangled states. *Science* **304,** 1478–1480 (2004).
40. Dür, W., Vidal, G. & Cirac, J. I. Three qubits can be entangled in two inequivalent ways. *Phys. Rev. A* **62,** 062314 (2000).
41. Häffner, H. *et al.* Scalable multiparticle entanglement of trapped ions. *Nature* **438,** 643–646 (2005).
42. Deutsch, D. & Jozsa, R. Rapid solution of problems by quantum computation. *Proc. R. Soc. Lond. A* **439,** 553–558 (1992).
43. Chuang, I. L. *et al.* Experimental realization of a quantum algorithm. *Nature* **393,** 143–146 (1998).
44. Gulde, S. *et al.* Implementation of the Deutsch–Jozsa algorithm on an ion-trap quantum computer. *Nature* **421,** 48–50 (2003).
45. Bennett, C. H. *et al.* Teleporting an unknown quantum state via dual classical and Einstein–Podolsky-Rosen channels. *Phys. Rev. Lett.* **70,** 1895–1899 (1993).
46. Barrett, M. D. *et al.* Deterministic quantum teleportation of atomic qubits. *Nature* **429,** 737–739 (2004).
47. Riebe, M. *et al.* Deterministic quantum teleportation with atoms. *Nature* **429,** 734–737 (2004).
48. Reichle, R. *et al.* Experimental purification of two-atom entanglement. *Nature* **443,** 838–841 (2006).
49. Chiaverini, J. *et al.* Realization of quantum error correction. *Nature* **432,** 602–605 (2004).
50. Chiaverini, J. *et al.* Implementation of the semiclassical quantum Fourier transform in a scalable system. *Science* **308,** 997–1000 (2005).
51. Grover, L. K. Quantum mechanics helps in searching for a needle in a haystack. *Phys. Rev. Lett.* **79,** 325–328 (1997).
52. Wineland, D. J., Bollinger, J. J., Itano, W. M., Moore, F. L. & Heinzen, D. J. Spin squeezing and reduced quantum noise in spectroscopy. *Phys. Rev. A* **46,** R6797–R6800 (1992).

© 2008 Macmillan Publishers Limited. All rights reserved

53. Itano, W. M. *et al.* Quantum projection noise: population fluctuations in two-level systems. *Phys. Rev. A* **47,** 3554–3570 (1993).
54. Meyer, V. *et al.* Experimental demonstration of entanglement-enhanced rotation angle estimation using trapped ions. *Phys. Rev. Lett.* **86,** 5870–5873 (2001).
55. Leibfried, D. *et al.* Trapped-ion quantum simulator: experimental application to nonlinear interferometers. *Phys. Rev. Lett.* **89,** 247901 (2002).
56. Huelga, S. F. *et al.* Improvement of frequency standards with quantum entanglement. *Phys. Rev. Lett.* **79,** 3865–3868 (1997).
57. André, A., Sørensen, A. S. & Lukin, M. D. Stability of atomic clocks based on entangled atoms. *Phys. Rev. Lett.* **92,** 230801 (2004).
58. Schaetz, T. *et al.* Enhanced quantum state detection efficiency through quantum information processing. *Phys. Rev. Lett.* **94,** 010501 (2005).
59. Hume, D. B., Rosenband, T. & Wineland, D. J. High-fidelity adaptive qubit detection through repetitive quantum nondemolition measurements. *Phys. Rev. Lett.* **99,** 120502 (2007).
60. Rosenband, T. *et al.* Frequency ratio of Al^+ and Hg^+ single-ion optical clocks; metrology at the 17th decimal place. *Science* **319,** 1808–1812 (2008).
61. Guerlin, C. *et al.* Progressive field-state collapse and quantum non-demolition photon counting. *Nature* **448,** 889–894 (2007).
62. Roos, C. F., Chwalla, M., Kim, K., Riebe, M. & Blatt, R. 'Designer atoms' for quantum metrology. *Nature* **443,** 316–319 (2006).
63. Benhelm, J., Kirchmair, G., Roos, C. F. & Blatt, R. Towards fault-tolerant quantum computing with trapped ions. *Nature Phys.* **4,** 463–466 (2008).
64. Ozeri, R. *et al.* Errors in trapped-ion quantumgates due to spontaneous photon scattering. *Phys. Rev. A* **75,** 042329 (2007).
65. Zhu, S.-L., Monroe, C. & Duan, L.-M. Arbitrary-speed quantum gates within large ion crystals through miminum control of laser beams. *Europhys. Lett.* **73,** 485–491 (2006).
66. Duan, L.-M. Scaling ion trap quantum computation through fast quantum gates. *Phys. Rev. Lett.* **93,** 100502 (2004).
67. DeVoe, R. G. Elliptical ion traps and trap arrays for quantum computation. *Phys. Rev. A* **58,** 910–914 (1998).
68. Cirac, J. I. & Zoller, P. A scalable quantum computer with ions in an array of microtraps. *Nature* **404,** 579–581 (2000).
69. Kielpinski, D., Monroe, C. & Wineland, D. J. Architecture for a large-scale ion-trap quantum computer. *Nature* **417,** 709–711 (2002).
70. Cirac, I., Zoller, P., Kimble, J. & Mabuchi, H. Quantum state transfer and entanglement distribution among distant nodes in a quantum network. *Phys. Rev. Lett.* **78,** 3221–3224 (1997).
71. Duan, L.-M. & Kimble, H. J. Scalable photonic quantum computation through cavity-assisted interactions. *Phys. Rev. Lett.* **92,** 127902 (2004).
72. Duan, L.-M. *et al.* Probabilistic quantum gates between remote atoms through interference of optical frequency qubits. *Phys. Rev. A* **73,** 062324 (2006).
73. Rowe, M. *et al.* Transport of quantum states and separation of ions in a dual rf ion trap. *Quantum Inform. Comput.* **2,** 257–271 (2002).
74. Hucul, D. *et al.* On the transport of atomic ions in linear and multidimensional trap arrays. Preprint at <http://arxiv.org/abs/quant-ph/0702175> (2007).
75. Huber, G. *et al.* Transport of ions in a segmented linear Paul trap in printed-circuit-board technology. *New J. Phys.* **10,** 013004 (2008).
76. Rohde, H. *et al.* Sympathetic ground-state cooling and coherent manipulation with two-ion crystals. *J. Opt. Soc. Am. B* **3,** S34–S41 (2001).
77. Blinov, B. B. *et al.* Sympathetic cooling of trapped Cd^+ isotopes. *Phys. Rev. A* **65,** 040304 (2002).
78. Barrett, M. D. *et al.* Sympathetic cooling of $^9Be^+$ and $^{24}Mg^+$ for quantum logic. *Phys. Rev. A* **68,** 042302 (2003).
79. Turchette, Q. A. *et al.* Heating of trapped ions from the quantum ground state. *Phys. Rev. A* **61,** 063418 (2000).
80. Deslauriers, L. *et al.* Scaling and suppression of anomalous heating in ion traps. *Phys. Rev. Lett.* **97,** 103007 (2006).
81. Leibrandt, D., Yurke, B. & Slusher, R. Modeling ion trap thermal noise decoherence. *Quant. Inform. Comput.* **7,** 52–72 (2007).
82. Labaziewicz, J. *et al.* Suppression of heating rates in cryogenic surface-electrode ion traps. *Phys. Rev. Lett.* **100,** 013001 (2008).
83. Stick, D. *et al.* Ion trap in a semiconductor chip. *Nature Phys.* **2,** 36–39 (2006).
84. Chiaverini, J. *et al.* Surface-electrode architecture for ion-trap quantum information processing. *Quantum Inform. Comput.* **5,** 419–439 (2005).
85. Seidelin, S. *et al.* Microfabricated surface-electrode ion trap for scalable quantum information processing. *Phys. Rev. Lett.* **96,** 253003 (2006).
86. Kim, J. *et al.* System design for large-scale ion trap quantum information processor. *Quant. Inform. Comput.* **5,** 515–537 (2005).
87. Leibfried, D., Knill, E., Ospelkaus, C. & Wineland, D. J. Transport quantum logic gates for trapped ions. *Phys. Rev. A* **76,** 032324 (2007).
88. Wunderlich, C. & Balzer, C. Quantum measurements and new concepts for experiments with trapped ions. *Adv. At. Mol. Opt. Phys.* **49,** 293–376 (2003).
89. Porras, D. & Cirac, J. I. Quantum manipulation of trapped ions in two dimensional Coulomb crystals. *Phys. Rev. Lett.* **96,** 250501 (2006).
90. Taylor, J. M. & Calarco, T. Wigner crystals of ions as quantum hard drives. Preprint at <http://arxiv.org/abs/0706.1951> (2007).
91. Chiaverini, J. & Lybarger Jr, W. E. Laserless trapped-ion quantum simulations without spontaneous scattering using microtrap arrays. *Phys. Rev. A* **77,** 022324 (2008).
92. Mølmer, K. & Sørensen, A. Multiparticle entanglement of hot trapped ions. *Phys. Rev. Lett.* **82,** 1835–1838 (1999).
93. Milburn, G. J., Schneider, S. & James, D. F. Ion trap quantum computing with warm ions. *Fortschr. Physik* **48,** 801–810 (2000).
94. Solano, E., de Matos Filho, R. L. & Zagury, N. Mesoscopic superpositions of vibronic collective states of *N* trapped ions. *Phys. Rev. Lett.* **87,** 060402 (2001).
95. Leibfried, D. *et al.* Experimental demonstration of a robust, high-fidelity geometric two ion-qubit phase gate. *Nature* **422,** 412–415 (2003).
96. Haljan, P. C. *et al.* Entanglement of trapped-ion clock states. *Phys. Rev. A* **72,** 062316 (2005).
97. Home, J. P. *et al.* Deterministic entanglement and tomography of ion spin qubits. *New J. Phys.* **8,** 188 (2006).
98. Matsukevich, D. N., Maunz, P., Moehring, D. L., Olmschenk, S. & Monroe, C. Bell inequality violation with two remote atomic qubits. *Phys. Rev. Lett.* **100,** 150404 (2008).
99. Hensinger, W. K. *et al.* T-junction ion trap array for two-dimensional ion shuttling storage, and manipulation. *Appl. Phys. Lett.* **88,** 034101 (2006).

Acknowledgements We thank H. Häffner, J. Home, E. Knill, D. Leibfried, C. Roos and P. Schmidt for comments on the manuscript.

Author Information Reprints and permissions information is available at www.nature.com/reprints. The authors declare no competing financial interests. Correspondence should be addressed to R.B. (Rainer.Blatt@uibk.ac.at).

© 2008 Macmillan Publishers Limited. All rights reserved

NATURE|Vol 453|19 June 2008|doi:10.1038/nature07126

Quantum coherence and entanglement with ultracold atoms in optical lattices

Immanuel Bloch[1]

At nanokelvin temperatures, ultracold quantum gases can be stored in optical lattices, which are arrays of microscopic trapping potentials formed by laser light. Such large arrays of atoms provide opportunities for investigating quantum coherence and generating large-scale entanglement, ultimately leading to quantum information processing in these artificial crystal structures. These arrays can also function as versatile model systems for the study of strongly interacting many-body systems on a lattice.

Recent advances in the laser cooling of neutral (uncharged) atoms and the creation of ultracold quantum gases[1] have opened up intriguing possibilities for the quantum manipulation of arrays of neutral atoms. Around 15–20 years ago, spectacular progress was made on the trapping and spectroscopy of single particles, and researchers concentrated on studying such single particles with ever-increasing precision. Now, researchers are building on these exquisite manipulation and trapping techniques to extend this control over larger arrays of particles. Not only can neutral atoms be trapped in microscopic potentials engineered by laser light[2–4], but the interactions between these particles can be controlled with increasing precision. Given this success, the creation of large-scale entanglement and the use of ultracold atoms as interfaces between different quantum technologies have come to the forefront of research, and ultracold atoms are among the 'hot' candidates for quantum information processing, quantum simulations and quantum communication.

Two complementary lines of research using ultracold atoms are dominating this field. In a bottom-up approach, arrays of atoms can be built up one by one. By contrast, a top-down approach uses the realization of degenerate ultracold bosonic[5–7] and fermionic[8–10] quantum gases as an alternative way of establishing large-scale arrays of ultracold atoms; this approach allows the creation of large numbers of neutral atoms, with almost perfect control over the motional and electronic degrees of freedom of millions of atoms with temperatures in the nanokelvin range. When such ultracold atoms are loaded into three-dimensional arrays of microscopic trapping potentials, known as optical lattices, the atoms are sorted in such a way that every lattice site is occupied by a single atom, for example, by strong repulsive interactions in the case of bosons or by Pauli blocking in the case of fermions. For bosons, this corresponds to a Mott insulating state[11–15], whereas for fermions a band insulating state is created[16], both of which form a highly regular, ordered, quantum register at close to zero kelvin. After initialization, the interactions and the states of the atoms are controlled to coax them into the correct — possibly entangled — macroscopic (many body) state to be used in quantum information processing, for example, or metrology at the quantum limit.

Ultracold atoms cannot yet rival the pristine control achieved using ion-trap experiments (see page 1008), but some key features nevertheless render them highly attractive. First, neutral atoms couple only weakly to the environment, allowing long storage and coherence times, even in the proximity of bulk materials; this feature has made them highly successful in the field of cavity quantum electrodynamics (see page 1023). Second, ultracold atoms in optical lattices form the only system so far in which a large number (up to millions) of particles can be initialized simultaneously. Eventually, any system proposed for quantum information processing will have to deal with such large arrays, and many of the perspectives (and difficulties) associated with these can already be tested using ultracold atoms today. Ultracold atoms have therefore also become promising candidates in a related line of research — quantum simulations[4,17–19] — in which highly controllable quantum matter is used to unravel some of the most intriguing questions in modern condensed-matter physics involving strongly correlated many-body quantum systems. In this review, I describe basic aspects of optical trapping and optical lattices. I then discuss novel state manipulation and entanglement schemes in optical lattices, and how these might be used to implement measurement-based quantum computing.

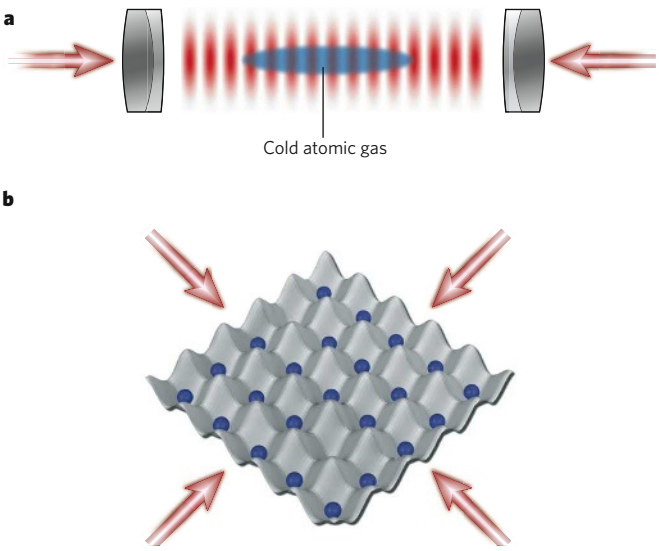

Figure 1 | Formation of optical lattices. a, An optical standing wave is generated by superimposing two laser beams. The antinodes (or nodes) of the standing wave act as a perfectly periodic array of microscopic laser traps for the atoms. The crystal of light in which the cold atoms can move and are stored is called an optical lattice. **b**, If several standing waves are overlapped, higher-dimensional lattice structures can be formed, such as the two-dimensional optical lattice shown here.

[1]Institut für Physik, Johannes Gutenberg-Universität Mainz, 55099 Mainz, Germany.

© 2008 Macmillan Publishers Limited. All rights reserved

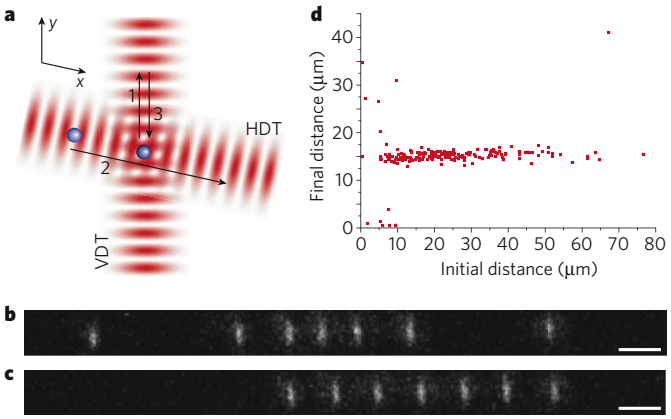

Figure 2 | Atom sorting in an optical lattice. **a**, Strings of atoms can be rearranged by using two crossed standing waves. Atoms can be moved independently in the horizontal or vertical direction by tuning the frequency difference of the counterpropagating laser beams, forming a single one-dimensional optical lattice. HDT, horizontal dipole trap; VDT, vertical dipole trap. **b**, Fluorescence image of the initial atom distribution on the lattice. Scale bar, 15 μm. **c**, Applying distance-control operations on six of the seven atoms creates a string of atoms with equidistant separation. This is carried out by moving the two standing waves through several sequences (for example, 1, 2, and then 3) as shown in **a**. The atoms follow the movement of the nodes of the lattices and can thereby be repositioned. Scale bar, 15 μm. **d**, For initial distances of the atoms larger than 10 μm, the atoms can be sorted to controlled separations of 15 μm. (Reproduced, with permission, from ref. 31.)

Optical trapping and optical lattices

Neutral atoms can be efficiently trapped by laser light thanks to the optical dipole force. This technique — in which cells can be manipulated with optical tweezers, without touching them — is widely used in biophysics. The basic principle is that a particle with an electric dipole moment **d** placed in an external electric field **E** experiences a potential energy: $V_{dip} = -\mathbf{d}\bullet\mathbf{E}$. In the case of an oscillating electric field, an oscillating electric dipole moment is induced, for example when laser light interacts with an atom. Such an induced dipole moment is proportional to the applied electric field strength and results in an optical potential that is generally proportional to the intensity of the applied light field. The optical potential can either be attractive or repulsive, depending on whether the frequency of the applied laser field is smaller or larger than the atomic resonance frequency[2].

Periodic potentials can be formed out of such optical potentials by interfering laser beams propagating along different directions. The resultant periodic pattern of bright and dark fringes is experienced by the atoms as a perfect array of potential maxima and minima in which they move. In the simplest case of two counterpropagating laser beams along the z axis, a periodic potential of the form $V_{lat} = V_0 \sin^2(2\pi z/\lambda)$ is created, with a periodicity of $\lambda/2$, where λ is the wavelength of the light field and V_0 is the potential depth of the lattice (Fig. 1a). By superimposing several of these standing-wave laser fields along different directions, it is possible to create lattice structures, in which atoms can be trapped, in one, two or three dimensions (Fig. 1b). For a three-dimensional lattice, each trapping site can be viewed as an almost perfect harmonic oscillator, with vibrational frequencies in the range of tens to hundreds of kilohertz. Such optical-lattice potentials offer huge flexibility in their design. For example, the potential depth can be changed along different directions independently, and the general lattice geometry can be controlled, for example by interfering laser beams at different angles. It has recently become possible to engineer spin-dependent lattice potentials, where different atomic spin states experience different periodic potentials[20,21], or superlattice structures composed of arrays of double wells[22–24]. When each of these double wells is filled with two atoms, they can mimic the behaviour of electronic double-quantum-dot systems[25–27], and similar strategies can be used to create protected and long-lived qubits and robust quantum gates. The additional strength of optical-lattice-based systems, however, lies in the fact that thousands of potential wells are present in parallel, each of which can be efficiently coupled with the neighbouring well to create massively parallel acting quantum gates.

Atom transport and state manipulation

One important challenge when dealing with ultracold atoms is keeping to a minimum any possible heating, because this could affect the motional or spin degrees of freedom. At the same time, atoms may need to be moved close together to initiate quantum gates between arbitrary pairs of atoms in the array. There has recently been an impressive advance in the control and movement of single atoms. A French research team has shown how a single atom, trapped in a dipole trap, can be moved in a two-dimensional plane in a highly controlled way with sub-micrometre spatial resolution[28]. The researchers also showed that atoms can be moved without detectable perturbation even if they are prepared in a coherent superposition of two internal spin states and when transferred from one dipole trap to another. In another approach, a team from the University of Bonn, Germany, used an 'atomic conveyer belt' to move and position atoms trapped in the nodes of a one-dimensional standing-wave light field[29]. By slightly tuning the frequency difference between the two counterpropagating laser fields, the standing wave can be turned into a 'walking wave', the motion of which the atoms closely track. By crossing two such conveyer belts along orthogonal directions, atoms can be actively sorted in an array. Such an 'atom sorting machine' has been used to sort a lattice randomly filled with seven atoms into a perfectly ordered string of equidistant single atoms[30,31] (Fig. 2). These impressive feats both contain crucial components for the controlled entanglement of atom pairs or strings of atoms in the lattice (discussed in the next section).

The control and imaging of single atoms in an optical lattice remains a huge challenge, but David Weiss and co-workers have recently shown how such imaging can work in a three-dimensional array of atoms[32]. By using a high-resolution optical lens, the researchers were able to image two-dimensional planes in a three-dimensional optical lattice

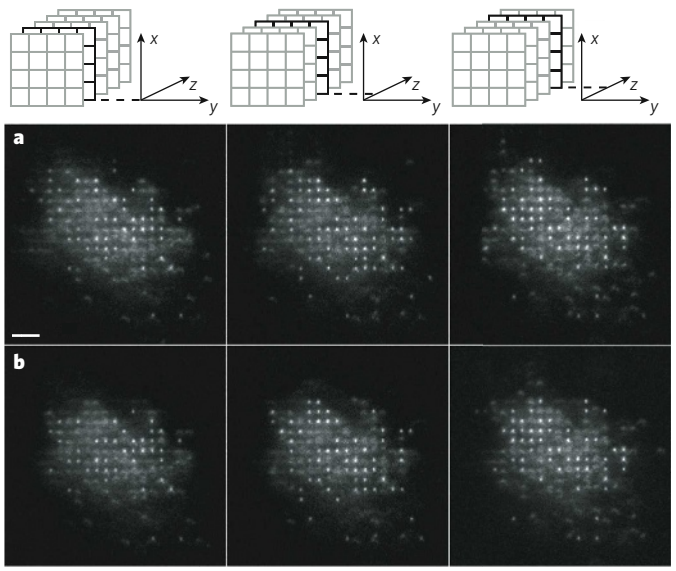

Figure 3 | Imaging of single atoms in a three-dimensional optical lattice. Up to 250 atoms are loaded from a magneto-optical trap into a three-dimensional optical lattice with a spacing of 4.9 μm. (Scale bar, 3 × 4.9 μm.) The atoms can be imaged by collecting their fluorescence light through a high-resolution objective lens. Different planes of the array can be targeted by focusing the imaging plane to different lattice planes (left to right). The same array of atoms can be imaged repeatedly while only minimally affecting the atom distribution in the lattice. Imaging was carried out along the z axis, at time $t = 0$ (**a**) and $t = 3$ s (**b**). (Reproduced, with permission, from ref. 32.)

© 2008 Macmillan Publishers Limited. All rights reserved

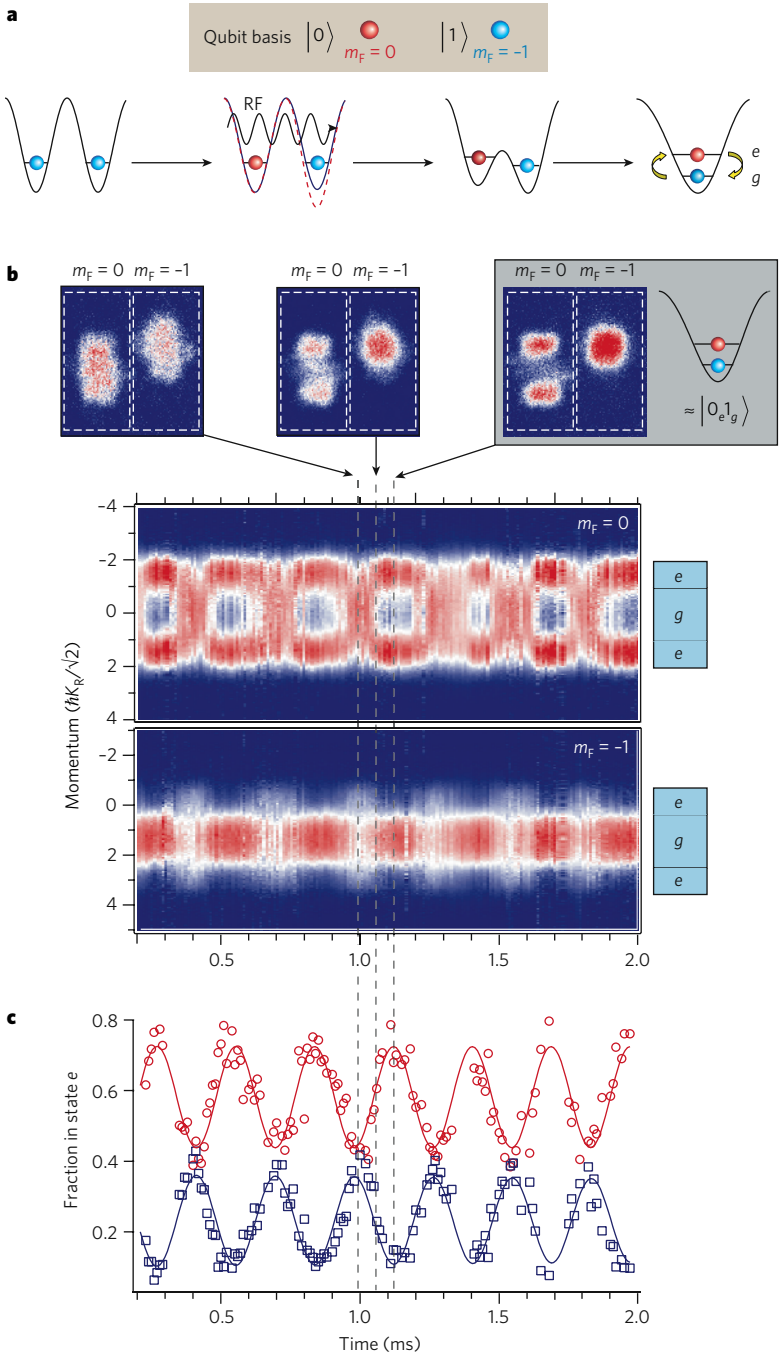

Figure 4 | Demonstration of a SWAP operation using exchange interactions. **a**, Using radio-frequency (RF) waves, two atoms in a double-well potential are brought into different spin states, denoted $|0\rangle$ (red) and $|1\rangle$ (blue), on different sides of the optical double-well potential. The two logical qubits, $|0\rangle$ and $|1\rangle$, are encoded in the electronic hyperfine states with angular momentum $m_F = 0$ and $m_F = -1$ of the atoms, respectively. When merging these into a single well, quantum-mechanical exchange interactions induce an oscillation between the spin populations in the lower and upper vibrational level. **b**, This oscillation can be revealed by using an adiabatic band mapping technique in which the population of different vibrational states is mapped onto different Brillouin zones after slowly turning off the lattice potential. (The Brillouin zones are given in units of $\hbar K_R\sqrt{2}$, where $\hbar K_R$ is the recoil momentum of the lattice photons. The colours reflect the number of atoms with this momentum, increasing from blue to red.) This technique allows the population of the vibrational states of a single lattice site to be measured in a spin-resolved way (upper images are examples of experimental results for the band mapping for three distinct times during the exchange oscillation cycle, with the times denoted by dashed lines through the lower images and images in **c**), revealing the exchange-induced spin dynamics (lower images, which show band mapping results taken at different times in the exchange oscillation cycle). The blue boxes indicate the momenta to which the different vibrational states, $|g\rangle$ and $|e\rangle$, are mapped. **c**, Multiple SWAP cycles are observed, by measuring the population in the excited vibrational state $|e\rangle$ over time (red, atoms in spin state $|0\rangle$; and blue, atoms in spin state $|1\rangle$). These show negligible decay during the oscillations, indicating the robust implementation of the two-qubit interaction. For half of a SWAP cycle, denoted as a $\sqrt{\text{SWAP}}$ operation, two atoms can be entangled to form a Bell pair. (Reproduced, with permission, from ref. 23.)

filled with up to 250 atoms loaded from a laser-cooled cloud of atoms (Fig. 3). To achieve such single-site and single-atom resolution, the team used a wider-spaced optical lattice with a periodicity of 4.9 μm, and the shallow depth of field of the optical detection allowed them to select a single lattice plane. Several groups are already trying to achieve such single-site and single-atom resolution[33–35] for tightly spaced lattices formed by counterpropagating laser beams in the optical regime, with a site spacing of only a few hundred nanometres. When such arrays are loaded from a degenerate bosonic or fermionic quantum gas, the lattice would be filled with hundreds of thousands of atoms, with each plane containing an array of typically 10,000 atoms that could be imaged and manipulated simultaneously.

Entangling neutral atoms

Storing, sorting and controlling atoms in a large-scale array of particles is only one part of the challenge; the other consists of entangling the particles to implement quantum gates or to generate multiparticle entangled resource states for quantum information processing. This requires precise control over the internal-state-dependent interactions between the particles in a lattice. Ideally, the interactions between any pair of atoms in the lattice should be controllable such that they could be coaxed into any desired quantum-mechanical superposition state. One approach is to use a single-atom read-and-write head, moving atoms in optical tweezers to the desired location to interact with other atoms. However, the transport takes precious time, during which harmful decoherence processes could destroy the fragile quantum coherence stored in the register.

Another possibility might be better adapted to the lattice system and takes advantage of the massive parallelism with which operations can be carried out. The interactions between neutral atoms are typically very short-ranged — they are known as 'contact interactions' — and only occur when two particles are brought together at a single lattice site, where they can directly interact. But when each atom is brought into contact with each of its neighbours, the collisions between the particles

© 2008 Macmillan Publishers Limited. All rights reserved

can create a highly entangled multiparticle state[20,21], known as a 'cluster state'[36], which can be used as a resource state for quantum information processing. The superposition principle of quantum mechanics allows this to be achieved in a highly parallel way, using a state-dependent optical lattice, in which different atomic spin states experience different periodic potentials[20,21]. Starting from a lattice where each site is filled with a single atom, the atoms are first brought into a superposition of two internal spin states. The spin-dependent lattice is then moved in such a way that an atom in two different spin states splits up and moves to the left and right simultaneously so that it collides with its two neighbours. In a single operation, a whole string of atoms can thereby be entangled. However, if the initial string of atoms contained defects, an atom moving to the side may have no partner to collide with, so the length of the entangled cluster would be limited to the average length between two defects. The sorted arrays of atoms produced by an 'atomic sorting machine' could prove to be an ideal starting point for such collisional quantum gates, as the initial arrays are defect free. In addition, defects could be efficiently removed by further active cooling of the quantum gases in the lattice. Indeed, such cooling is necessary to enhance the regularity of the filling achieved with the current large-scale ensembles. Several concepts related to 'dark state' cooling methods from quantum optics and laser cooling could help in this case. The atoms could be actively cooled into the desired many-body quantum state, which is tailored to be non-interacting (that is, dark) with the applied cooling laser field[37,38].

When constructing such entangled states, the particles' many degrees of freedom can couple to the environment, leading to decoherence, which will destroy the complex quantum superpositions of the atoms. To avoid such decoherence processes, which affect the system more the larger it becomes, it is desirable to construct many-particle states, which are highly insensitive to external perturbations. Unfortunately, when using the outlined controlled-collisions scheme to create an atomic cluster state, the atomic qubits must be encoded in states that undergo maximal decoherence with respect to magnetic field fluctuations. Two recent experiments have shown how decoherence could be avoided, by implementing controlled exchange interactions between atoms[23,39]; this could lead to new ways of creating robust entangled states (discussed in the next section). Another way to avoid the problem of decoherence is to apply faster quantum gates, so more gate operations could be carried out within a fixed decoherence time. For the atoms of ultracold gases in optical lattices, Feshbach resonances[40,41] can be used to increase the collisional interactions and thereby speed up gate operations. However, the 'unitarity limit' in scattering theory does not allow the collisional interaction energy to be increased beyond the on-site vibrational oscillation frequency, so the lower timescale for a gate operation is typically a few tens of microseconds. Much larger interaction energies, and hence faster gate times, could be achieved by using the electric dipole–dipole interactions between polar molecules[42], for example, or Rydberg atoms[43,44]; in the latter case, gate times well below the microsecond range are possible. For Rydberg atoms, a phase gate between two atoms could be implemented by a dipole-blockade mechanism, which inhibits the simultaneous excitation of two atoms and thereby induces a phase shift in the two-particle state only when both atoms are initially placed in the same quantum state. The first signs of such a Rydberg dipole-blockade mechanism have been observed in mesoscopic cold and ultracold atom clouds[45–48], but it remains to be seen how well they can be used to implement quantum gates between two individual atoms. Rydberg atoms offer an important advantage for the entanglement of neutral atoms: they can interact over longer distances, and addressing single atoms in the lattice to turn the interactions between these two atoms on and off avoids the need for the atoms to move. In addition, the lattice does not have to be perfectly filled for two atoms to be entangled if their initial position is known before applying the Rydberg interaction.

Novel quantum gates via exchange interactions

Entangling neutral atoms requires state-dependent interactions. A natural way to achieve this is to tune the collisional interactions between atoms to different strengths for different spin states, or to allow explicitly only specific spin states into contact for controlled collisions. Another possibility is to exploit the symmetry of the underlying two-particle wavefunctions to create the desired gate operations, even in the case of completely spin-independent interactions between atoms. This principle lies at the heart of two experiments to control the spin–spin interactions between two particles using exchange symmetry[23,39,49], and builds on original ideas and experiments involving double quantum-dot systems[25,26].

Research teams at the National Institute of Standards and Technology (NIST) at Gaithersburg, Maryland, and the University of Mainz, Germany, have demonstrated such interactions for two atoms in a double-well potential. How do these exchange interactions arise, and how can they be used to develop primitives (or building blocks) for quantum information processing? As one of the fundamental principles of quantum mechanics, the total quantum state of two particles (used in two experiments) has to be either symmetrical in the case of bosons or antisymmetrical for fermions, with respect to exchange of the two particles. When trapped on a single lattice site, a two-particle bosonic wavefunction can be factored into a spatial component, which describes the positions of the two particles, and a spin component, which describes

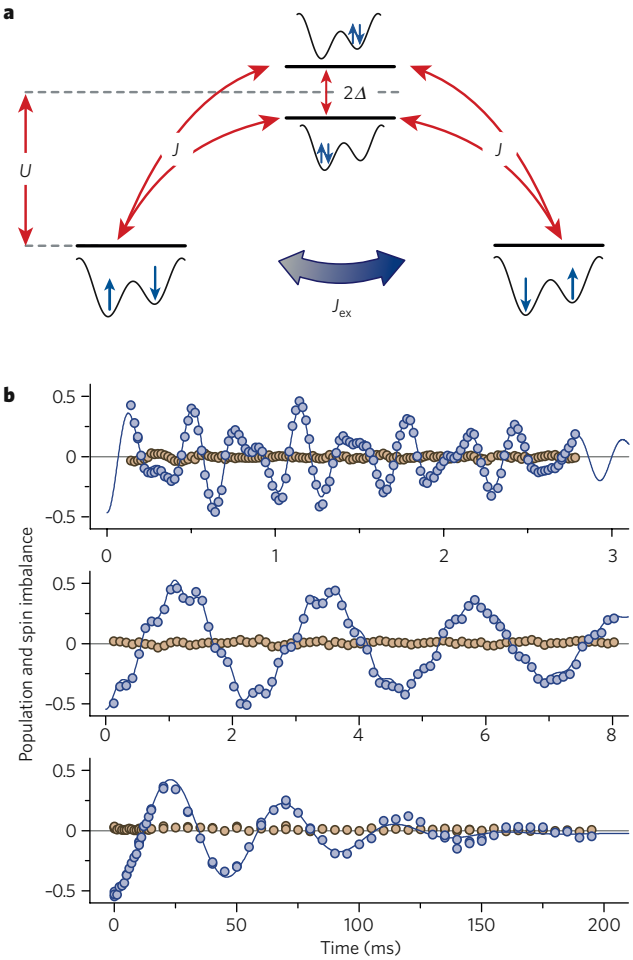

Figure 5 | Superexchange coupling between atoms on neighbouring lattice sites. a, Virtual hopping processes (left to right, and right to left) mediate an effective spin–spin interaction with strength J_{ex} between the atoms, which can be controlled in both magnitude and sign by using a potential bias Δ between the wells. U is the on-site interaction energy between the atoms on a single lattice site, and J is the single-particle tunnel coupling. **b**, The effective spin–spin interaction emerges when increasing the interaction U between the particles relative to their kinetic energy J (top to bottom). It can be observed in the time evolution of the magnetization dynamics in the double well. Blue circles indicate spin imbalance, and brown circles indicate population imbalance. The curves denote a fit to a theoretical model taking into account the full dynamics observed within the Hubbard model. (Reproduced, with permission, from ref. 39.)

© 2008 Macmillan Publishers Limited. All rights reserved

their spin orientations. If the spatial wavefunction part is symmetrical with respect to particle exchange, the spin part must be symmetrical too, or they must both be antisymmetrical, so the total wavefunction always retains the correct symmetry. The two combinations, however, have different interaction energies: in the case of a symmetrical spatial wavefunction, both particles are more likely to be located in the same position, whereas for an antisymmetrical one they are never found at the same location. The former leads to strong collisional interactions between the particles, whereas the latter leads to a vanishing interaction energy. It is this energy difference between the 'singlet' (antisymmetrical) and 'triplet' (symmetrical) spin states that gives rise to an effective spin–spin interaction between the two particles.

When the NIST team placed two atoms onto a lattice site, with the spin-up particle in the vibrational ground state $|\uparrow, g\rangle$ and the spin-down particle in the first excited vibrational state $|\downarrow, e\rangle$, the effective spin interaction led to exchange oscillations between the qubit states $|\uparrow, g\rangle|\downarrow, e\rangle \Leftrightarrow |\downarrow, g\rangle|\uparrow, e\rangle$. In computer terminology this is called a SWAP operation and is one of the fundamental primitives of quantum computing[25]. In fact, the exchange operation allows for any transformations by an angle θ of the form $|a, b\rangle = \cos(\theta)|a, b\rangle + i\sin(\theta)|b, a\rangle$, for any spin state $|a\rangle$, $|b\rangle$ of the particles. When the SWAP operation is carried only halfway through, denoted by $\sqrt{\text{SWAP}}$, the two particles end up as an entangled Bell pair. The NIST researchers observed such SWAP operations by first preparing a $|\uparrow\rangle_L|\downarrow\rangle_R$ state configuration in the double-well potential (where L is the left well and R is the right well) and then actively deforming the double well, so both particles ended up on the same lattice site. Exchange oscillations then flipped the spin configurations over time; these were observed in the experiment over up to 12 SWAP cycles without any noticeable damping of the exchange oscillation signal[23] (Fig. 4). In the NIST experiments, the atoms had to be brought onto the same lattice site to initiate exchange interactions, but virtual tunnelling processes[24] can achieve this without moving the particles. In these processes, atoms constantly probe their neighbouring lattice site, after which either they or their neighbouring particle return to the original lattice site. Such a process can either leave the initial position of the atoms intact or swap them over, thereby giving rise to an effective spin–spin interaction between the two particles of the form $H_{\text{eff}} = -J_{\text{ex}}\mathbf{S}_i \bullet \mathbf{S}_j$, where $\mathbf{S}_i$ and $\mathbf{S}_j$ are the spin operators on neighbouring lattice sites i and j. Such 'super-exchange' interactions therefore do not require any direct wavefunction overlap of the two particles, as this overlap is established during the atoms' virtual hopping process. The strength and the sign of the coupling constant J_{ex} can be evaluated through second-order perturbation theory, resulting in $J_{\text{ex}} = 4J^2/U$, where J is the single-particle tunnelling coupling and U is the spin-independent interaction energy between two particles occupying the same lattice site[50–52]. The Mainz researchers could directly observe and control such superexchange spin couplings between two neighbouring atoms in the double-well potential created by an optical superlattice (Fig. 5). These controllable superexchange interactions form the basic building block of quantum magnetism in strongly correlated electronic media and give rise, for example, to the antiferromagnetic ordering of a two-component Fermi gas on a lattice[50]. For quantum information processing, they too can be used to implement SWAP operations, but their control over the spin states between pairs of atoms could find other uses as well. For example, by first creating an array of Bell pairs in optical superlattices using exchange interactions or spin-changing collisions[53], these Bell pairs could be connected to each other using Ising-type superexchange interactions to directly create cluster states or other useful resource states[54] (Fig. 6). Compared with the controlled-collision approaches, however, these cluster states can be encoded in substates with vanishing total magnetization and so could be more robust to global field fluctuations leading to decoherence.

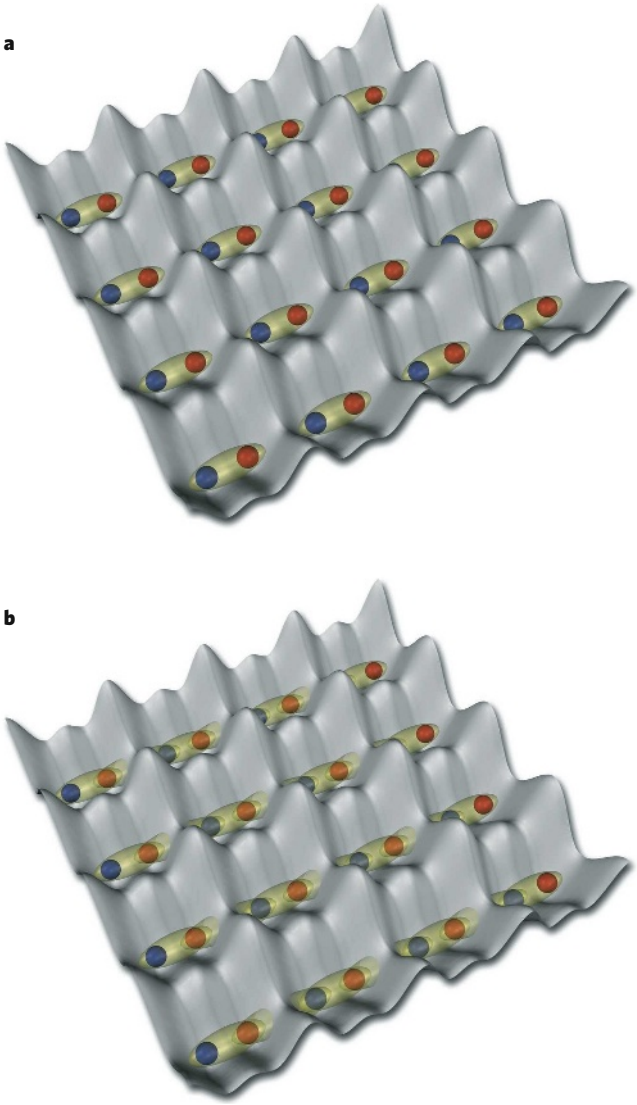

Figure 6 | Array of entangled Bell pairs obtained using optical superlattices. a, Using exchange-mediated $\sqrt{\text{SWAP}}$ operations, arrays of Bell pairs (yellow) consisting of two atoms in different spin states (red and blue) can be created in a massively parallel way. **b**, These two-particle entangled states can be extended to larger multiparticle entangled states, by using spin–spin interactions to connect atoms on the edges of a Bell pair (marked by additional yellow bonds between the edges of previously unconnected Bell pairs). Applying this operation additionally along the orthogonal direction leads to the creation of large two-dimensional cluster states or other useful entangled resource states[54].

Measurement-based quantum computing

In the field of quantum computing, there are several computational models, such as the quantum circuit model[55–57], adiabatic quantum computation[58], the quantum Turing machine[59,60], teleportation-based models[61–63] and the one-way quantum computer[64,65], giving rise to a large number of possibilities for how to carry out a quantum computation. In the circuit model, for example, information is processed through a series of unitary gate operations, after which the desired calculation result is obtained at the output. In the measurement-based one-way quantum computer, information is processed through a sequence of adaptive measurements on an initially prepared, highly entangled resource state. Measurement-based quantum computing (MBQC) lays out a wholly new concept for the practical implementation of quantum information processing that is extremely well suited to large arrays of particles, such as neutral atoms in optical lattices. First, a large, multiparticle, entangled resource state, such as a cluster state, is created by means of controlled collisions or the methods outlined above. A computational algorithm is then implemented by carrying out a sequence of adaptive single-particle measurements, together with local single-particle unitary operations (Fig. 7). The size of the initial entangled cluster is thereby crucial, as it determines the length of the calculation that can be carried out. Single-site addressing techniques that are currently being implemented in labs

© 2008 Macmillan Publishers Limited. All rights reserved

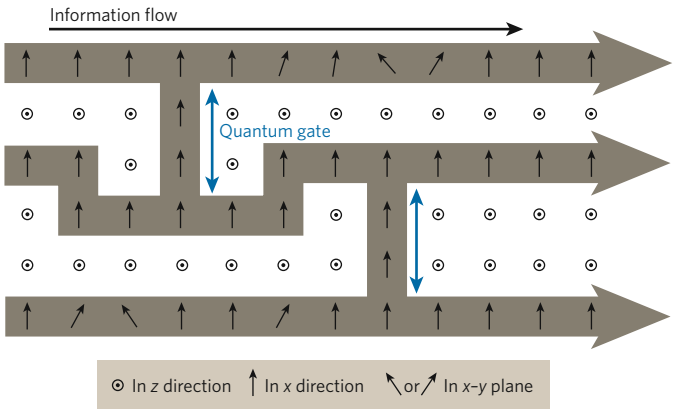

Figure 7 | Information processing in a one-way quantum computer. After initially creating a multiparticle entangled cluster state, a sequence of adaptive single-particle measurements is carried out. In each step of the computation, the measurement basis for the next qubit depends on the specific program and on the outcome of previous measurement results. Finally, after all the measurements have been carried out, the state of the system is given by $|\xi^{\{\alpha\}}\rangle|\Psi_{\rm out}^{\{\alpha\}}\rangle$, where the measured qubits are given by the product state $|\xi^{\{\alpha\}}\rangle$ and the final output state is $|\Psi_{\rm out}^{\{\alpha\}}\rangle$, which contains the computation result up to a unitary operation that depends on all of the previous measurement results, $\{\alpha\}$. The short black arrows in the figure denote the direction of the measurement basis for the corresponding qubit, and the large brown arrows indicate the directions of information flow. When measuring the qubits between two chains (blue arrows), a quantum gate is realized. (Reproduced, with permission, from ref. 36.)

could one day lead to cluster-state computing in lattice-based systems. Proof-of-principle demonstrations have already been carried out using photon-based cluster states[66,67], and the model could be implemented in any system consisting of an array of qubits.

So far, MBQC has already become a major research field, currently mainly driven by theory, with interdisciplinary connections to entanglement theory, graph theory, computational complexity, logic and statistical physics. Several fundamental questions regarding MBQC have now been answered, such as, which multiparticle entangled states can serve as 'universal resources'[68–71]. Universality in this context is defined as the ability to generate every possible quantum state from the resource through single-qubit operations alone. Using this definition, it can be shown that the two-dimensional cluster state is a universal resource state, whereas the one-dimensional cluster state is not. Furthermore, a universal resource state must be maximally entangled with respect to all types of entanglement measure. If this were not the case, there could be a state with a higher degree of entanglement that could not be generated from the resource state through single-qubit operations. Because single-qubit operations cannot add entanglement to the system, the initial state could not have been a universal resource state.

For MBQC to be implemented in practice, it is important to know how defects, such as missing atoms or doubly occupied sites, can limit its computational power. Active cooling of the lattice gases could help to reduce such defects[37,38], although a finite residual number of defects will always be present. Astonishingly, the computational power degrades sharply only when the number of defects is increased above the percolation threshold[72] of statistical physics. In addition, a cluster state can be a universal resource even in the presence of defects, although the location of the defects would need to be known in order to adapt a measurement sequence to them. In an effort to understand the computational power of MBQC, several teams have also shown how MBQC can be connected to other measurement-based quantum computing schemes, such as teleportation based ones[73–76].

Any real-world quantum computer will also need to overcome the adverse effects of decoherence arising from interactions with the environment, which affect the fragile quantum superpositions and the entangled many-body states in the system and result in errors in quantum computation. In the drive to create a scalable quantum computer, quantum error correction has a crucial role in correcting such errors[77], while maintaining the greater computational speed of a quantum computer over a classical computer. Quantum error correction allows an arbitrarily long quantum computation to be carried out with arbitrary accuracy, if the error level of the underlying operations is below a threshold value[78–80]. By combining topological error-correction schemes originating from Alexei Kitaev's toric code[81] and 'magic-state distillation' into the one-way quantum computer, it has recently been shown that an error threshold of up to 7.5×10^{-3} can be realized[82]. For a local model in two dimensions, in which only nearest-neighbour interactions between the particles are allowed, this is the highest threshold known, but it is still beyond the reach of current experiments.

Quantum simulations

Ultracold quantum gases in optical lattices are also being used to simulate the behaviour of strongly interacting electronic systems[4,17,19], where they might be able to shed light on complex problems emerging from condensed-matter physics. A prominent example is the Hubbard model, which forms a simple theoretical description of interacting fermions on a lattice. Although the basic hamiltonian for such a system can be easily written down, solving it is one of the hardest problems in condensed-matter physics. One problem that ultracold atoms might help to answer is whether a high-temperature superconducting phase can emerge from within the Hubbard model[83]. Such a scenario is widely thought to lie at the heart of the mystery of high-temperature superconductors[84]. A starting point for such studies could be an antiferromagnetically ordered gas of fermions, which after doping has been proposed to transform into a spin-liquid phase[84,85] that can support the formation of a high-temperature superconductor. Several research groups are currently trying to establish an antiferromagnetically ordered Mott insulator in fermionic atom clouds with two spin components. The temperature requirements to achieve this seem to be demanding[86], however, and progress will again depend on finding ways to cool the quantum gases within the lattice[37].

Outlook

From both an experimental and a theoretical point of view, optical lattices offer outstanding possibilities for implementing new designs for quantum information processing and quantum simulations. Some of the major experimental challenges in the field are lowering the temperatures of the lattice-based quantum gases and achieving single-site addressing, the latter being, for example, a crucial requirement for the MBQC model. Although there might be special situations in which this can be avoided, such addressability would provide a fresh impetus for the field of quantum simulations. Imagine being able to observe and control a spin system in two dimensions with 10,000 particles simultaneously in view, all with single-site and single-atom resolution. Observing dynamic evolutions in these systems, probing their spatial correlations and finally implementing quantum information processing in a truly large-scale system would all become possible. ■

1. Pitaevskii, L. & Stringari, S. *Bose–Einstein Condensation* (Oxford Univ. Press, Oxford, 2003).
2. Grimm, R., Weidemüller, M. & Ovchinnikov, Y. B. Optical dipole traps for neutral atoms. *Adv. At. Mol. Opt. Phys.* **42,** 95–170 (2000).
3. Jessen, P. S. & Deutsch, I. H. Optical lattices. *Adv. At. Mol. Opt. Phys.* **37,** 95–139 (1996).
4. Bloch, I., Dalibard, J. & Zwerger, W. Many-body physics with ultracold gases. Preprint at ⟨http://arxiv.org/abs/0704.3011⟩ (2007).
5. Anderson, M. H., Ensher, J. R., Matthews, M. R., Wieman, C. E. & Cornell, E. A. Observation of Bose–Einstein condensation in a dilute atomic vapor. *Science* **269,** 198–201 (1995).
6. Davis, K. B. *et al.* Bose–Einstein condensation in a gas of sodium atoms. *Phys. Rev. Lett.* **75,** 3969–3973 (1995).
7. Bradley, C. C., Sackett, C. A., Tollett, J. J. & Hulet, R. G. Evidence of Bose–Einstein condensation in an atomic gas with attractive interactions. *Phys. Rev. Lett.* **75,** 1687–1690 (1995).
8. DeMarco, B. & Jin, D. D. Onset of Fermi degeneracy in a trapped atomic gas. *Science* **285,** 1703–1706 (1999).
9. Schreck, F. *et al.* Quasipure Bose–Einstein condensate immersed in a Fermi Sea. *Phys. Rev. Lett.* **87,** 080403 (2001).
10. Truscott, A. G., Strecker, K. E., McAlexander, W. I., Partridge, G. P. & Hulet, R.G. Observation of Fermi pressure in a gas of trapped atoms. *Science* **291,** 2570–2572 (2001).

© 2008 Macmillan Publishers Limited. All rights reserved

11. Fisher, M. P. A., Weichman, P. B., Grinstein, G. & Fisher, D. S. Boson localization and the superfluid-insulator transition. *Phys. Rev. B* **40,** 546–570 (1989).
12. Jaksch, D., Bruder, C., Cirac, J. I., Gardiner, C. W. & Zoller, P. Cold bosonic atoms in optical lattices. *Phys. Rev. Lett.* **81,** 3108–3111 (1998).
13. Greiner, M., Mandel, M. O., Esslinger, T., Hänsch, T. & Bloch, I. Quantum phase transition from a superfluid to a Mott insulator in a gas of ultracold atoms. *Nature* **415,** 39–44 (2002).
14. Stöferle, T., Moritz, H., Schori, C., Köhl, M. & Esslinger, T. Transition from a strongly interacting 1D superfluid to a Mott insulator. *Phys. Rev. Lett.* **92,** 130403 (2004).
15. Spielman, I. B., Phillips, W. D. & Porto, J. V. The Mott insulator transition in two dimensions. *Phys. Rev. Lett.* **98,** 080404 (2007).
16. Köhl, M., Moritz, H., Stöferle, T., Günter, K. & Esslinger, T. Fermionic atoms in a three dimensional optical lattice: observing Fermi surfaces, dynamics, and interactions. *Phys. Rev. Lett.* **94,** 080403 (2005).
17. Jaksch, D. & Zoller, P. The cold atoms Hubbard toolbox. *Ann. Phys. (NY)* **315,** 52–79 (2005).
18. Bloch, I. Ultracold quantum gases in optical lattices. *Nature Phys.* **1,** 23–30 (2005).
19. Lewenstein, M. *et al.* Ultracold atomic gases in optical lattices: mimicking condensed matter physics and beyond. *Adv. Phys.* **56,** 243–379 (2007).
20. Jaksch, D., Briegel, H. J., Cirac, J. I., Gardiner, C. W. & Zoller, P. Entanglement of atoms via cold controlled collisions. *Phys. Rev. Lett.* **82,** 1975–1978 (1999).
21. Mandel, O. *et al.* Controlled collisions for multiparticle entanglement of optically trapped atoms. *Nature* **425,** 937–940 (2003).
22. Sebby-Strabley, J., Anderlini, M., Jessen, P. S. & Porto, J. V. Lattice of double wells for manipulating pairs of cold atoms. *Phys. Rev. A* **73,** 033605 (2006).
23. Anderlini, M. *et al.* Controlled exchange interaction between pairs of neutral atoms in an optical lattice. *Nature* **448,** 452–456 (2007).
24. Fölling, S. *et al.* Direct observation of second-order atom tunnelling. *Nature* **448,** 1029–1032 (2007).
25. Loss, D. & DiVincenzo, D. P. Quantum computation with quantum dots. *Phys. Rev. A* **57,** 120–126 (1998).
26. Petta, J. R. *et al.* Coherent manipulation of coupled electron spins in semiconductor quantum dots. *Science* **309,** 2180–2184 (2005).
27. Hanson, R., Kouwenhoven, L. P., Petta, J. R., Tarucha, S. & Vandersypen, L. M. K. Spins in few-electron quantum dots. *Rev. Mod. Phys.* **79,** 1217–1265 (2007).
28. Beugnon, J. *et al.* Two-dimensional transport and transfer of a single atomic qubit in optical tweezers. *Nature Phys.* **3,** 696–699 (2007).
29. Schrader, D. *et al.* A neutral atom quantum register. *Phys. Rev. Lett.* **93,** 150501 (2004).
30. Miroshnychenko, Y. *et al.* Precision preparation of strings of trapped neutral atoms. *New J. Phys.* **8,** 191 (2006).
31. Miroshnychenko, Y. *et al.* An atom-sorting machine. *Nature* **442,** 151 (2006).
32. Nelson, K. D., Li, X. & Weiss, D. S. Imaging single atoms in a three-dimensional array. *Nature Phys.* **3,** 556–560 (2007).
33. Cho, J. Addressing individual atoms in optical lattices with standing-wave driving fields. *Phys. Rev. Lett.* **99,** 020502 (2007).
34. Joo, J., Lim, Y. L., Beige, A. & Knight, P. L. Single-qubit rotations in two-dimensional optical lattices with multiqubit addressing. *Phys. Rev. A* **74,** 042344 (2006).
35. Gorshkov, A. V., Jiang, L., Greiner, M., Zoller, P. & Lukin, M. D. Coherent quantum optical control with subwavelength resolution. Preprint at ⟨http://arxiv.org/abs/0706.3879⟩ (2007).
36. Briegel, H. J. & Raussendorf, R. Persistent entanglement in arrays of interacting particles. *Phys. Rev. Lett.* **86,** 910–913 (2001).
37. Griessner, A., Daley, A. J., Clark, S. R., Jaksch, D. & Zoller, P. Dark-state cooling of atoms by superfluid immersion. *Phys. Rev. Lett.* **97,** 220403 (2006).
38. Griessner, A., Daley, A. J., Clark, S. R., Jaksch, D. & Zoller, P. Dissipative dynamics of atomic Hubbard models coupled to a phonon bath: dark state cooling of atoms within a Bloch band of an optical lattice. *New J. Phys.* **9,** 44 (2007).
39. Trotzky, S. *et al.* Time-resolved observation and control of superexchange interactions with ultracold atoms in optical lattices. *Science* **319,** 295–299 (2008).
40. Inouye, S. *et al.* Observation of Feshbach resonances in a Bose–Einstein condensate. *Nature* **392,** 151–154 (1998).
41. Courteille, P., Freeland, R. S., Heinzen, D. J., van Abeelen, F. A. & Verhaar, B. J. Observation of a Feshbach resonance in cold atom scattering. *Phys. Rev. Lett.* **81,** 69–72 (1998).
42. Micheli, A., Brennen, G. K. & Zoller, P. A toolbox for lattice-spin models with polar molecules. *Nature Phys.* **2,** 341–347 (2006).
43. Jaksch, D. *et al.* Fast quantum gates for neutral atoms. *Phys. Rev. Lett.* **85,** 2208–2211 (2000).
44. Lukin, M. D. *et al.* Dipole blockade and quantum information processing in mesoscopic atomic ensembles. *Phys. Rev. Lett.* **87,** 037901 (2001).
45. Tong, D. *et al.* Local blockade of Rydberg excitation in an ultracold gas. *Phys. Rev. Lett.* **93,** 063001 (2004).
46. Singer, K., Reetz-Lamour, M., Amthor, T., Marcassa, L. G. & Weidemüller, M. Suppression of excitation and spectral broadening induced by interactions in a cold gas of Rydberg atoms. *Phys. Rev. Lett.* **93,** 163001 (2004).
47. Liebisch, T. C., Reinhard, A., Berman, P. R. & Raithel, G. Atom counting statistics in ensembles of interacting Rydberg atoms. *Phys. Rev. Lett.* **95,** 253002 (2005).
48. Heidemann, R. *et al.* Evidence for coherent collective Rydberg excitation in the strong blockade regime. *Phys. Rev. Lett.* **99,** 163601 (2007).
49. Hayes, D., Julienne, P. S. & Deutsch, I. H. Quantum logic via the exchange blockade in ultracold collisions. *Phys. Rev. Lett.* **98,** 070501 (2007).
50. Auerbach, A. *Interacting Electrons and Quantum Magnetism* (Springer, New York, 2006).
51. Duan, L.-M., Demler, E. & Lukin, M. D. Controlling spin exchange interactions of ultracold atoms in an optical lattice. *Phys. Rev. Lett.* **91,** 090402 (2003).
52. Kuklov, A. B. & Svistunov, B. V. Counterflow superfluidity of two-species ultracold atoms in a commensurate optical lattice. *Phys. Rev. Lett.* **90,** 100401 (2003).
53. Widera, A. *et al.* Coherent collisional spin dynamics in optical lattices. *Phys. Rev. Lett.* **95,** 190405 (2005).
54. Vaucher, B., Nunnenkamp, A. & Jaksch, D. Creation of resilient entangled states and a resource for measurement-based quantum computation with optical superlattices. Preprint at ⟨http://arxiv.org/abs/0710.5099⟩ (2007).
55. Deutsch, D. Quantum computational networks. *Proc. R. Soc. Lond. A* **425,** 73–90 (1989).
56. Yao, A. in *Proc. 34th Annu. Symp. Found. Comput. Sci.* 352–361 (IEEE Computer Soc., Los Alamitos, 1993).
57. Barenco, A. *et al.* Elementary gates for quantum computation. *Phys. Rev. A* **52,** 3457–3467 (1995).
58. Farhi, E. *et al.* A quantum adiabatic evolution algorithm applied to random instances of an NP-complete problem. *Science* **292,** 472–476 (2001).
59. Deutsch, D. Quantum-theory, the Church–Turing principle and the universal quantum computer. *Proc. R. Soc. Lond. A* **400,** 97–117 (1985).
60. Bernstein, E. & Vazirani, U. in *Proc. 25th Annu. ACM Symp. Theor. Comput.* 11–20 (ACM Press, New York, 1993).
61. Gottesman, D. & Chuang, I. L. Demonstrating the viability of universal quantum computation using teleportation and single-qubit operations. *Nature* **402,** 390–393 (1999).
62. Knill, E., Laflamme, R. & Milburn, G. J. A scheme for efficient quantum computation with linear optics. *Nature* **409,** 46–52 (2001).
63. Nielsen, M. A. Quantum computation by measurement and quantum memory. *Phys. Lett. A* **308,** 96–100 (2003).
64. Raussendorf, R. & Briegel, H. J. A One-way quantum computer. *Phys. Rev. Lett.* **86,** 5188–5191 (2001).
65. Raussendorf, R. & Briegel, H. J. Computational model underlying the one-way quantum computer. *Quant. Info. Comput.* **2,** 443–486 (2002).
66. Walther, P. *et al.* Experimental one-way quantum computing. *Nature* **434,** 169–176 (2005).
67. Kiesel, N. *et al.* Experimental analysis of a four-qubit photon cluster state. *Phys. Rev. Lett.* **95,** 210502 (2005).
68. Gross, D., Eisert, J., Schuch, N. & Perez-Garcia, D. Measurement-based quantum computation beyond the one-way model. *Phys. Rev. A* **76,** 052315 (2007).
69. Van den Nest, M., Miyake, A., Dür, W. & Briegel, H. J. Universal resources for measurement-based quantum computation. *Phys. Rev. Lett.* **97,** 150504 (2006).
70. Van den Nest, M., Dür, W., Miyake, A. & Briegel, H. J. Fundamentals of universality in one-way quantum computation. *New J. Phys.* **9,** 204 (2007).
71. Gross, D. & Eisert, J. Novel schemes for measurement-based quantum computation. *Phys. Rev. Lett.* **98,** 220503 (2007).
72. Browne, D. E. *et al.* Phase transition of computational power in the resource states for one-way quantum computation. Preprint at ⟨http://arxiv.org/abs/0709.1729⟩ (2007).
73. Verstraete, F. & Cirac, J. I. Valence-bond states for quantum computation. *Phys. Rev. A* **70,** 060302 (2004).
74. Aliferis, P. & Leung, D. W. Computation by measurements: a unifying picture. *Phys. Rev. A* **70,** 062314 (2004).
75. Childs, A. M., Leung, D. W. & Nielsen, M. A. Unified derivations of measurement-based schemes for quantum computation. *Phys. Rev. A* **71,** 032318 (2005).
76. Jorrand, P. & Perdrix, S. Unifying quantum computation with projective measurements only and one-way quantum computation. Preprint at ⟨http://arxiv.org/abs/quant-ph/0404125⟩ (2004).
77. Shor, P. W. in *Proc. 37th Annu. Symp. Found. Comput. Sci.* 56–65 (IEEE Computer Soc., Los Alamitos, 1996).
78. Aharonov, D. & Ben-Or, M. in *Proc. 29th Annu. ACM Symp. Theor. Comput.* 176–188 (ACM Press, New York, 1997).
79. Gottesman, D. *Stabilizer Codes and Quantum Error Correction*. PhD thesis, California Inst. Technol. (1997).
80. Knill, E., Laflamme, R. & Zurek, W. H. Resilient quantum computation: error models and thresholds. *Proc. R. Soc. Lond. A* **454,** 365–384 (1998).
81. Kitaev, A. Y. Fault-tolerant quantum computation by anyons. *Ann. Phys. (NY)* **303,** 2–30 (2003).
82. Raussendorf, R. & Harrington, J. Fault-tolerant quantum computation with high threshold in two dimensions. *Phys. Rev. Lett.* **98,** 190504 (2007).
83. Hofstetter, W., Cirac, J. I., Zoller, P., Demler, E. & Lukin, M. D. High-temperature superfluidity of fermionic atoms in optical lattices. *Phys. Rev. Lett.* **89,** 220407 (2002).
84. Lee, P. A., Nagaosa, N. & Wen, X.-G. Doping a Mott insulator: physics of high-temperature superconductivity. *Rev. Mod. Phys.* **78,** 17–85 (2006).
85. Anderson, P. W. The resonating valence bond state in La_2CuO_4 and superconductivity. *Science* **235,** 1196–1198 (1987).
86. Werner, F., Parcollet, O., Georges, A. & Hassan, S. R. Interaction-induced adiabatic cooling and antiferromagnetism of cold fermions in optical lattices. *Phys. Rev. Lett.* **95,** 056401 (2005).

Acknowledgements I thank H. Briegel for discussions, and the German Research Foundation (DFG), the European Union (through the OLAQUI and SCALA projects) and the Air Force Office of Scientific Research (AFOSR) for support.

Author Information Reprints and permissions information is available at www.nature.com/reprints. The author declares no competing financial interests. Correspondence should be addressed to the author (bloch@uni-mainz.de).

© 2008 Macmillan Publishers Limited. All rights reserved

The quantum internet

H. J. Kimble[1]

Quantum networks provide opportunities and challenges across a range of intellectual and technical frontiers, including quantum computation, communication and metrology. The realization of quantum networks composed of many nodes and channels requires new scientific capabilities for generating and characterizing quantum coherence and entanglement. Fundamental to this endeavour are quantum interconnects, which convert quantum states from one physical system to those of another in a reversible manner. Such quantum connectivity in networks can be achieved by the optical interactions of single photons and atoms, allowing the distribution of entanglement across the network and the teleportation of quantum states between nodes.

In the past two decades, a broad range of fundamental discoveries have been made in the field of quantum information science, from a quantum algorithm that places public-key cryptography at risk to a protocol for the teleportation of quantum states[1]. This union of quantum mechanics and information science has allowed great advances in the understanding of the quantum world and in the ability to control coherently individual quantum systems[2]. Unique ways in which quantum systems process and distribute information have been identified, and powerful new perspectives for understanding the complexity and subtleties of quantum dynamical phenomena have emerged.

In the broad context of quantum information science, quantum networks have an important role, both for the formal analysis and the physical implementation of quantum computing, communication and metrology[2–5]. A notional quantum network based on proposals in refs 4, 6 is shown in Fig. 1a. Quantum information is generated, processed and stored locally in quantum nodes. These nodes are linked by quantum channels, which transport quantum states from site to site with high fidelity and distribute entanglement across the entire network. As an extension of this idea, a 'quantum internet' can be envisaged; with only moderate processing capabilities, such an internet could accomplish tasks that are impossible in the realm of classical physics, including the distribution of 'quantum software'[7].

Apart from the advantages that might be gained from a particular algorithm, there is an important advantage in using quantum connectivity, as opposed to classical connectivity, between nodes. A network of quantum nodes that is linked by classical channels and comprises k nodes each with n quantum bits (qubits) has a state space of dimension $k2^n$, whereas a fully quantum network has an exponentially larger state space, 2^{kn}. Quantum connectivity also provides a potentially powerful means to overcome size-scaling and error-correlation problems that would limit the size of machines for quantum processing[8]. At any stage in the development of quantum technologies, there will be a largest size attainable for the state space of individual quantum processing units, and it will be possible to surpass this size by linking such units together into a fully quantum network.

A different perspective of a quantum network is to view the nodes as components of a physical system that interact by way of the quantum channels. In this case, the underlying physical processes used for quantum network protocols are adapted to simulate the evolution of quantum many-body systems[9]. For example, atoms that are localized at separate nodes can have effective spin–spin interactions catalysed by single-photon pulses that travel along the channels between the nodes[10]. This 'quantum wiring' of the network allows a wide range for the effective hamiltonian and for the topology of the resultant 'lattice'. Moreover, from this perspective, the extension of entanglement across quantum networks can be related to the classical problem of percolation[11].

These exciting opportunities provide the motivation to examine research related to the physical processes for translating the abstract illustration in Fig. 1a into reality. Such considerations are timely because scientific capabilities are now passing the threshold from a learning phase with individual systems and advancing into a domain of rudimentary functionality for quantum nodes connected by quantum channels.

In this review, I convey some basic principles for the physical implementation of quantum networks, with the aim of stimulating the involvement of a larger community in this endeavour, including in systems-level studies. I focus on current efforts to harness optical processes at the level of single photons and atoms for the transportation of quantum states reliably across complex quantum networks.

Two important research areas are strong coupling of single photons and atoms in the setting of cavity quantum electrodynamics (QED)[12] and quantum information processing with atomic ensembles[13], for which crucial elements are long-lived quantum memories provided by the atomic system and efficient, quantum interfaces between light and matter. Many other physical systems are also being investigated and are discussed elsewhere (ref. 2 and websites for the Quantum Computation Roadmap (http://qist.lanl.gov/qcomp_map.shtml), the SCALA Integrated Project (http://www.scala-ip.org/public) and Qubit Applications (http://www.qubitapplications.com)).

A quantum interface between light and matter

The main scientific challenge in the quest to distribute quantum states across a quantum network is to attain coherent control over the interactions of light and matter at the single-photon level. In contrast to atoms and electrons, which have relatively large long-range interactions for their spin and charge degrees of freedom, individual photons typically have interaction cross-sections that are orders of magnitude too small for non-trivial dynamics when coupled to single degrees of freedom for a material system.

The optical physics community began to address this issue in the 1990s, with the development of theoretical protocols for the coherent transfer of quantum states between atoms and photons in the setting of cavity QED[6,14,15]. Other important advances have been made in the past

[1]Norman Bridge Laboratory of Physics 12–33, California Institute of Technology, Pasadena, California 91125, USA.

© 2008 Macmillan Publishers Limited. All rights reserved

decade[2,4], including with atomic ensembles[13,16]. The reversible mapping of quantum states between light and matter provides the basis for quantum-optical interconnects and is a fundamental primitive (building block) for quantum networks. Although the original schemes for such interconnects are sensitive to experimental imperfections, a complete set of theoretical protocols has subsequently been developed for the robust distribution of quantum information over quantum networks, including, importantly, the quantum repeater[4,17] and scalable quantum networks with atomic ensembles[13].

A generic quantum interface between light and matter is depicted in Fig. 1b. This interface is described by the interaction hamiltonian $H_{int}(t)$, where for typical states $H_{int}(t)\rangle \approx \hbar\chi(t)$, with $\hbar$ being $h/2\pi$ (where h is Planck's constant) and $\chi(t)$ being the time-dependent coupling strength between the internal material system and the electromagnetic field. Desirable properties for a quantum interface include that $\chi(t)$ should be 'user controlled' for the clocking of states to and from the quantum memory (for example, by using an auxiliary laser), that the physical processes used should be robust in the face of imperfections (for example, by using adiabatic transfer) and that mistakes should be efficiently detected and fixed (for example, with quantum error correction). In qualitative terms, the rate κ, which characterizes the bandwidth of the input–output channel, should be large compared with the rate γ, which characterizes parasitic losses, and both of these rates should be small compared with the rate of coherent coupling χ.

Examples of physical systems for realizing a quantum interface and distributing coherence and entanglement between nodes are shown in Fig. 1c, d. In the first example (Fig. 1c), single atoms are trapped in optical cavities at nodes A and B, which are linked by an optical fibre. External fields control the transfer of the quantum state $|\Psi\rangle$ stored in the atom at node A to the atom at node B by way of photons that propagate from node A to node B[6,18]. In the second example (Fig. 1d), a single-photon pulse that is generated at node A is coherently split into two

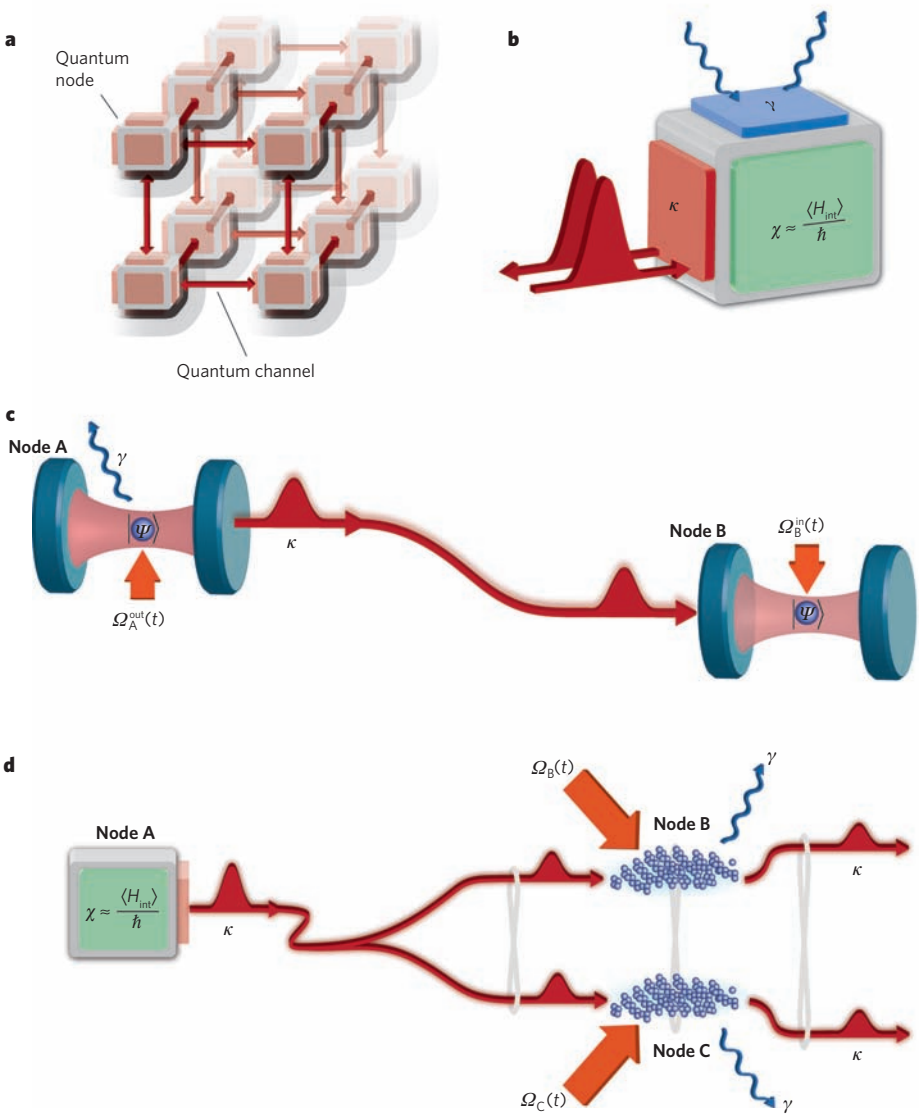

Figure 1 | Quantum networks. a, Shown is a notional quantum network composed of quantum nodes for processing and storing quantum states and quantum channels for distributing quantum information. Alternatively, such a network can be viewed as a strongly correlated many-particle system. **b**, The quantum interface between matter (coloured cube) and light (red curves) is depicted. Coherent interactions in the node are characterized by the rate χ; coupling between the node and photons in the external channel occurs at the rate κ; and parasitic losses occur at the rate γ. **c**, Quantum state transfer and entanglement distribution from node A to node B is shown in the setting of cavity quantum electrodynamics (QED)[6]. At node A, a pulse of the control field $\Omega_A^{out}(t)$ causes the transformation of atomic state $|\Psi\rangle$ into the state of a propagating optical field (that is, into a flying photon). At node B, the pulse $\Omega_B^{in}(t)$ is applied to map the state of the flying photon into an atom in the cavity, thereby realizing the transfer of the state $|\Psi\rangle$ from node A to node B (ref. 18). **d**, The distribution of entanglement by using ensembles of a large number of atoms is shown[13]. A single-photon pulse at node A is coherently split into two entangled components that propagate to node B and node C and then are coherently mapped by the control fields $\Omega_{B,C}^{in}(t)$ into a state that is entangled between collective excitations in each ensemble at node B and node C. At later times, components of the entangled state can be retrieved from the quantum memories by separate control fields, $\Omega_{B,C}^{out}(t)$ (ref. 19). $H_{int}(t)$, interaction hamiltonian; $\hbar$, $h/2\pi$ (where h is Planck's constant).

© 2008 Macmillan Publishers Limited. All rights reserved

components and propagates to nodes B and C, where the entangled photon state is coherently mapped into an entangled state between collective excitations at each of the two nodes[13,19]. Subsequent read-out of entanglement from the memories at node B and/or node C as photon pulses is implemented at the 'push of a button'.

Cavity QED

At the forefront of efforts to achieve strong, coherent interactions between light and matter has been the study of cavity QED[20]. In both the optical[12,21] and the microwave[22–25] domains, strong coupling of single atoms and photons has been achieved by using electromagnetic resonators of small mode volume (or cavity volume) V_m with quality factors $Q \approx 10^7$–10^{11}. Extensions of cavity QED to other systems[26] include quantum dots coupled to micropillars and photonic bandgap cavities[27], and Cooper pairs interacting with superconducting resonators (that is, circuit QED; see ref. 28 for a review).

Physical basis of strong coupling

Depicted in Fig. 2a is a single atom that is located in an optical resonator and for which strong coupling to a photon requires that a single intracavity photon creates a 'large' electric field. Stated more quantitatively, if the coupling frequency of one atom to a single mode of an optical resonator is g (that is, $2g$ is the one-photon Rabi frequency), then

$$g = \sqrt{\frac{|\boldsymbol{\varepsilon}\cdot\boldsymbol{\mu}_0|^2\,\omega_C}{2\hbar\varepsilon_0 V_m}} \qquad (1)$$

where $\boldsymbol{\mu}_0$ is the transition dipole moment between the relevant atomic states (with transition frequency ω_A), and $\omega_C \approx \omega_A$ is the resonant frequency of the cavity field, with polarization vector $\boldsymbol{\varepsilon}$. Experiments in cavity QED explore strong coupling with $g >> (\gamma, \kappa)$, where γ is the atomic decay rate to modes other than the cavity mode and κ is the decay rate of the cavity mode itself. Expressed in the language of traditional optical physics, the number of photons required to saturate the intracavity atom is $n_0 \approx \gamma^2/g^2$, and the number of atoms required to have an appreciable effect on the intracavity field is $N_0 \approx \kappa\gamma/g^2$. Strong coupling in cavity QED moves beyond traditional optical physics, for which $(n_0, N_0) >> 1$, to explore a qualitatively new regime with $(n_0, N_0) << 1$ (ref. 12).

In the past three decades, a variety of approaches have been used to achieve strong coupling in cavity QED[12,20–25]. In the optical domain, a route to strong coupling is the use of high-finesse optical resonators ($F \approx 10^5$–10^6) and atomic transitions with a large $\boldsymbol{\mu}_0$ (that is, oscillator strengths near unity). Progress along this path is illustrated in Fig. 2c, with research now far into the domain $(n_0, N_0) << 1$.

As the cavity volume V_m is reduced to increase g (equation (1)), the requirement for atomic localization becomes more stringent. Not surprisingly, efforts to trap and localize atoms in high-finesse optical cavities in a regime of strong coupling have been central to studies of cavity QED in the past decade, and the initial demonstration was in 1999 (ref. 29). Subsequent advances include extending the time for which an atom is trapped to 10 s (refs 30, 31); see ref. 32 for a review. Quantum control over both internal degrees of freedom (that is, the atomic dipole and the cavity field) and external degrees of freedom (that is, atomic motion) has now been achieved for a strongly coupled atom–cavity system[33]. And an exciting prospect is cavity QED with single trapped ions, for which the boundary for strong coupling has been reached[34].

Coherence and entanglement in cavity QED

Applying these advances to quantum networks has allowed single photons to be generated 'on demand' (Box 1). Through strong coupling of the cavity field to an atomic transition, an external control field $\Omega(t)$ transfers one photon into the cavity mode and then to free space by way of the cavity output mirror, leading to a single-photon pulse $|\phi_1(t)\rangle$ as a collimated beam. The temporal structure (both amplitude and phase) of the resultant 'flying photon' $|\phi_1(t)\rangle$ can be tailored by way of the control field $\Omega(t)$ (refs 6, 35), with the spatial structure of the wave packet being set by the cavity mode.

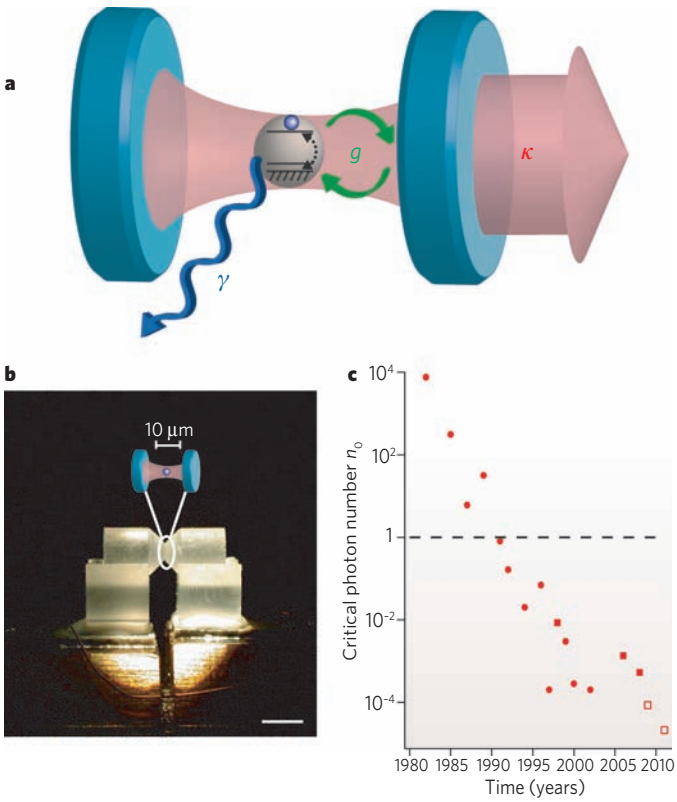

Figure 2 | Elements of cavity QED. a, Shown is a simple schematic of an atom–cavity system depicting the three governing rates (g, κ, γ) in cavity QED, where $g \approx \chi$ in Fig. 1. Coherent exchange of excitation between the atom and the cavity field proceeds at rate g, as indicated by the dashed arrow for the atom and the green arrows for the cavity field. **b**, A photograph of two mirror substrates that form the Fabry–Pérot cavity, which is also shown schematically. The cavity length $l = 10\,\mu m$, waist $w_0 = 12\,\mu m$ transverse to the cavity axis, and finesse $F \approx 5 \times 10^5$. The supporting structure allows active servo control of the cavity length to $\delta l \approx 10^{-14}$ m (ref. 12). Scale bar, 3 mm. **c**, The reduction in the critical photon number n_0 over time is shown for a series of experiments in cavity QED that were carried out by the Caltech Quantum Optics Group. These experiments involved either spherical-mirror Fabry–Pérot cavities (circles) or the whispering-gallery modes of monolithic SiO_2 resonators (squares). The data points shown for 2006 and 2008 are for a microtoroidal SiO_2 resonator[75,76]; those for 2009 and 2011 (open squares) are projections for this type of resonator[77].

Several experiments have confirmed the essential aspects of this process for the deterministic generation of single photons[30,34,36]. Significantly, in the ideal (adiabatic) limit, the excited state $|e\rangle$ of the atom is not populated because of the use of a 'dark state' protocol[37]. By deterministically generating a bit stream of single-photon pulses from single trapped atoms, these experiments are a first step in the development of quantum networks based on flying photons.

Compared with the generation of single photons by a variety of other systems[38], one of the distinguishing aspects of the dark-state protocol (Box 1) is that it should be reversible. That is, a photon that is emitted from a system A should be able to be efficiently transferred to another system B by applying the time-reversed (and suitably delayed) field $\Omega(t)$ to system B (Fig. 1c). Such an advance was made[18] by implementing the reversible mapping of a coherent optical field to and from internal states of a single trapped caesium atom. Although this experiment was imperfect, it provides the initial verification of the fundamental primitive on which the protocol for the physical implementation of quantum networks in ref. 6 is based (an important theoretical protocol that has been adapted to many theoretical and experimental settings).

© 2008 Macmillan Publishers Limited. All rights reserved

Box 1 | Mapping quantum states between atoms and photons

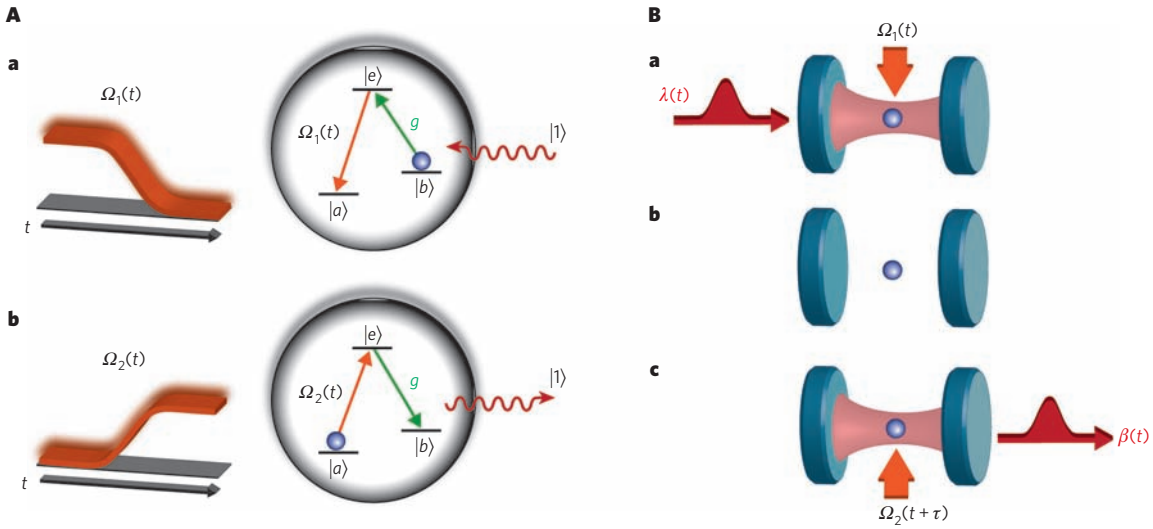

Reversible transfer of a state between light and a single trapped atom can be achieved through the mappings $|b\rangle|1\rangle \rightarrow |a\rangle|0\rangle$ and $|a\rangle|0\rangle \rightarrow |b\rangle|1\rangle$ for the coherent absorption and emission of single photons (in panel **A**, **a** and **b** of the figure, respectively)[18]. In this case, $|a\rangle$ and $|b\rangle$ represent internal states of the atom with long-lived coherence (for example, atomic hyperfine states in the $6S_{1/2}$, $F = 3$ and $F = 4$ manifolds of atomic caesium), and $|0\rangle$ and $|1\rangle$ are Fock states of the photons in the intracavity field with $n = 0$ and $n = 1$ excitations, respectively. The transition between $|b\rangle$ and $|e\rangle$ is strongly coupled to a mode of an optical cavity with interaction energy $\hbar g$, where g (in green) is the coherent coupling rate of the atom and the photon. In this simple setting, the interaction hamiltonian for atom and cavity field has a dark state $|D\rangle$ (that is, there is no excited state component $|e\rangle$)[37], as given by $|D\rangle = \cos\theta|a\rangle|0\rangle + \sin\theta|b\rangle|1\rangle$, where

$$\cos\theta = \left[1 + \frac{\Omega^2(t)}{g^2}\right]^{-1/2} \quad (1)$$

with $\Omega(t)$ as a classical control field[14]. For $\Omega(t = 0) = 0$, then $|D\rangle = |a\rangle|0\rangle$. By contrast, for $\Omega(t \rightarrow \infty) >> g$, $|D\rangle \rightarrow |b\rangle|1\rangle$.

Panel **A**, **a** of the figure shows that by adiabatically ramping a control field $\Omega_1(t) >> g$ from on to off over a time Δt that is slow compared with $1/g$, the atomic state is mapped from $|b\rangle$ to $|a\rangle$ with the accompanying coherent absorption of one intracavity photon. Conversely, in panel **A**, **b** of the figure, by turning a control field $\Omega_2(t)$ from off to on, the atomic state is mapped from $|a\rangle$ to $|b\rangle$ with the transfer of one photon into the cavity mode.

These two processes can be combined to achieve the coherent transfer of the state of a propagating optical field $\lambda(t) = |\phi_{\text{field}}(t)\rangle$ into and out of a quantum memory formed by the atomic states $|a\rangle$ and $|b\rangle$ (ref. 18; figure, panel **B**). In the ideal case, the mapping is specified by $|\phi_{\text{field}}(t)\rangle|b\rangle \rightarrow |0\rangle(c_1|a\rangle + c_0|b\rangle) \ldots$ (storage) $\ldots |0\rangle(c_1|a\rangle + c_0|b\rangle) \rightarrow |\phi_{\text{field}}(t+\tau)\rangle|b\rangle$, where the field state is taken to be a coherent superposition of zero (c_0) and one (c_1) photon, $|\phi_{\text{field}}(t)\rangle = E(t)[c_0|0\rangle_{\text{field}} + c_1|1\rangle_{\text{field}}]$. $E(t)$ is the envelope of the field external to the cavity, with $\int|E(t)|^2dt = 1$; $t+\tau$ is a user-selected time (discussed below). Given timing information for the incoming field $|\phi_{\text{field}}(t)\rangle$, the first step in this process (figure, panel **B**, **a**) is accomplished by adiabatically ramping the control field $\Omega_1(t)$ from on to off, as in **A**, **a**. After this step, the internal states of the atom provide a long-lived quantum memory (figure, panel **B**, **b**). At a user-selected later time $t+\tau$, the final step is initiated (figure, panel **B**, **c**) by turning $\Omega_2(t+\tau)$ from off to on (as in **A**, **b**), thereby coherently mapping the atomic state $c_1|a\rangle + c_0|b\rangle$ back to the 'flying' field state $\beta(t) = |\phi_{\text{field}}(t+\tau)\rangle$.

The adiabatic transfer of quantum states (as described in Box 1, as well as related possibilities[10,35]) relies on strong coupling between an atom and a single polarization of the intracavity field. However, by extending the ideas in Box 1 to the two polarization eigenmodes of the cavity for given transverse and longitudinal mode orders, it is possible to generate entanglement between the internal states of the atom and the polarization state of a coherently generated photon[39–41]. An initial control field $\Omega_1(t_1)$ results in entanglement between internal states of the atom b, $|b_\pm\rangle$, and the polarization state of a flying photon $|\phi^{\pm}_{\text{field}}(t_1)\rangle$ that is coherently generated by the coupled atom–cavity system. Applying a second control field $\Omega_2(t_2)$ returns the atom to its initial (unentangled) state while generating a second flying photon $|\xi^{\pm}_{\text{field}}(t_2)\rangle$, thereby leading to entanglement between the polarizations of the fields, $\phi^{\pm}_{\text{field}}$ and $\xi^{\pm}_{\text{field}}$, emitted at times t_1 and t_2.

Such a sequence of operations has been applied to single rubidium atoms falling through a high-finesse optical cavity[21]. In this study, entangled photons were generated with a time separation $\tau = t_2 - t_1$ limited by the atomic transit time. Although the atoms arrived randomly into the cavity mode in this case, the protocol itself is intrinsically deterministic. With trapped atoms, it will be possible to generate entangled states at user selected times (t_1, t_2) at the 'push of a button.' Moreover, the scheme is inherently reversible, so the entanglement between atom and field can be used to distribute entanglement to a second atom–cavity system in a network.

In a broader context, important advances have been made in the generation and transfer of quantum states in other physical systems, including quantum dots[42] and circuits[28] coupled to cavities.

With the maturation of experimental capabilities in cavity QED that is now evident, many previously developed theoretical protocols will become possible. These include the sequential generation of entangled multiqubit states[43], the teleportation of atomic states from one node to another[15], photonic quantum computation by way of photon–photon interactions at the nodes[35] and reversible mapping of quantum states of atomic motion to and from light[44]. Clearly, new technical capabilities beyond conventional (Fabry–Pérot) cavities will be required to facilitate such scientific investigations; several candidate systems are discussed in Box 2.

Quantum networks with atomic ensembles

An area of considerable research activity in the quest to distribute coherence and entanglement across quantum networks has been the interaction of light with atomic ensembles that consist of a large collection of identical atoms. For the regime of continuous variables, entanglement has been achieved between two atomic ensembles, each of which consists of ~10^{12} atoms[45], and the quantum teleportation of light to matter has been demonstrated by mapping coherent optical states to the collective spin states of an atomic memory[46]. Further research of the continuous variables regime is reviewed elsewhere[47]. Here I focus, instead, on the regime of discrete variables, with photons and atomic excitations considered one by one.

© 2008 Macmillan Publishers Limited. All rights reserved

Box 2 | A new paradigm for cavity QED

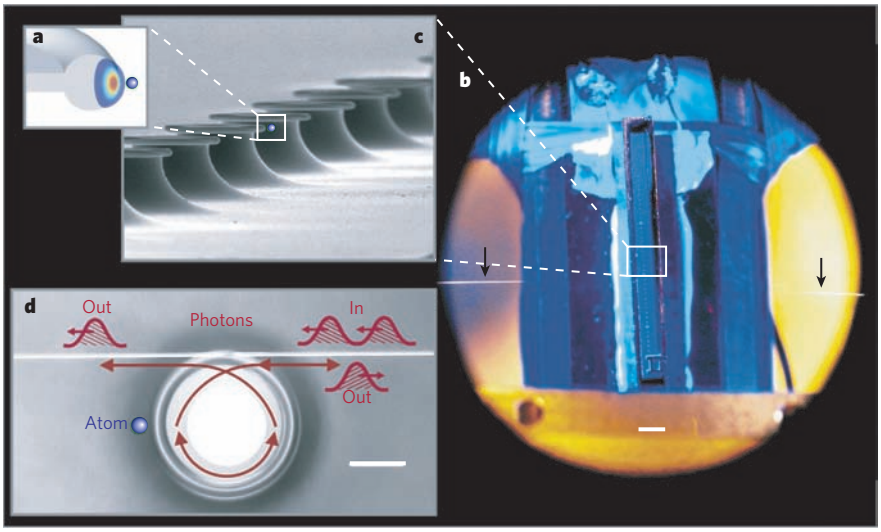

To build large-scale quantum networks[4,6], many quantum nodes will need to be interconnected over quantum channels. Because conventional (Fabry–Pérot) configurations are ill suited for this purpose, there have been efforts to develop alternative microcavity systems[26], both for single atoms[75,76,78] and for atom-like systems (such as nitrogen-vacancy centres in diamond[79]). A quantitative comparison of candidate systems is provided in ref. 77.

A remarkable resonator for this purpose is the microtoroidal cavity that is formed from fused SiO_2 (refs 80,81) (shown in the figure). Such a resonator supports a whispering-gallery mode[82] circulating around the outer circumference of the toroid (shown in cross-section in grey, in panel **a** of the figure), with an evanescent field external to the resonator. The intensity of the resonator mode is indicated by the coloured contours. Because of the small mode volume V_m and large quality factor Q, an atom (blue) interacting with the evanescent field of a whispering-gallery mode can be far into the regime of strong coupling, with projected values for the critical photon n_0 and atom N_0 numbers ($n_0 \approx 2 \times 10^{-5}$ and $N_0 \approx 10^{-6}$)[77] that are significantly greater than current[12] and projected[77] values for cavity QED with Fabry–Pérot cavities (Fig. 2c).

Pioneering fabrication techniques[80,81] lend themselves to the integration of many microtoroidal resonators to form optical networks, as illustrated in panel **b** and **c** of the figure. Panel **b** shows a photograph of a silicon chip with a linear array of microtoroidal resonators within an ultrahigh-vacuum apparatus[76]. The toroids appear as small scattering centres on a silicon chip that runs vertically down the centre of the picture. Black arrows indicate a horizontal SiO_2 fibre taper for coupling light to and from one resonator. Scale bar, 2 mm. Panel **c** is a scanning electron micrograph of an array of microtoroidal resonators (a magnification of the region bounded by the white box in panel **b**), showing toroids of fused SiO_2 on silicon supports[80].

These resonators have the capability for input–output coupling with small parasitic loss[81] for the configuration shown in panel **d** (scale bar, 10 μm), which is a micrograph of an individual toroid and fibre taper from panel **b**[76]. $Q = 4 \times 10^8$ has been realized at $\lambda = 1{,}550$ nm, and $Q \approx 10^8$ at $\lambda = 850$ nm, with good prospects for improvement to $Q \approx 10^{10}$ (ref. 77). For these parameters, the efficiency ε for coupling quantum fields into and out of the resonator could approach $\varepsilon \approx 0.99$–0.999 while remaining firmly in the regime of strong coupling[77]. Such high efficiency is crucial for the realization of complex quantum networks, including for distributing and processing quantum information[4,6,35] and for investigating the association between quantum many-body systems and quantum networks[9,11].

The initial step in this quest to realize a quantum network was the demonstration of strong coupling between individual atoms and the field of a microtoroidal resonator[75]. More recently, non-classical fields have been generated from the interaction of single atoms with a microtoroidal resonator by way of a 'photon turnstile', for which a single atom dynamically regulates the transport of photons one by one through the microtoroidal resonator[76] (figure, panel **d**). Only single photons can be transmitted in the forward direction (from right to left in the figure), with excess photons $n > 1$ dynamically rerouted to the backward direction.

Writing and reading collective spin excitations

Research on discrete quantum variables is based on the remarkable theoretical protocol described in ref. 13, in which Luming Duan, Mikhail Lukin, Juan Ignacio Cirac and Peter Zoller presented a realistic scheme for entanglement distribution by way of a quantum-repeater architecture[4,17]. Fundamental to this protocol, which is known as the DLCZ protocol, is the generation and retrieval of single 'spin' excitations within an ensemble of a large number of atoms[48] (Box 3). Together with photoelectric detection of field 1, a laser pulse ('write' pulse) creates a single excitation $|1_a\rangle$ that is stored collectively within the atomic ensemble. At a later time, a second laser pulse ('read' pulse) deterministically converts excitation stored within the atomic memory in the state $|1_a\rangle$ into a propagating field, denoted field 2.

The basic processes illustrated in Box 3 can be extended to create an entangled pair of ensembles, L and R (ref. 13; Fig. 3a). The entangled state is generated in a probabilistic but heralded[49] manner from quantum interference in the measurement process. That is, detection of a photon from one atomic ensemble or the other in an indistinguishable manner results in an entangled state with one collective spin excitation shared coherently between the ensembles. In the ideal case, and to lowest-order probability, a photoelectric detection event at either of the two detectors projects the ensembles into the entangled state $|\Psi_{L,R}\rangle = \frac{1}{\sqrt{2}}(|0_a\rangle_L|1_a\rangle_R \pm e^{i\eta_1}|1_a\rangle_L|0_a\rangle_R)$, with the sign (+ or −) set by whether detector 1 or detector 2 records the event. The phase η_1 is determined by the difference between the phase shifts along the two channels, $\eta_1 = \beta_L - \beta_R$ (ref. 49), which must be stable. Any given trial with a 'write' pulse is unlikely to produce a detection event at either detector, and such failed trials require the system to be reinitialized. However, a photoelectric detection event at either detector unambiguously heralds the creation of the entangled state. Limited by the coherence time between the metastable lower atomic states $|g\rangle_i$ and $|s\rangle_i$ for all atoms $i = 1, 2, \ldots, N_a$ within the ensemble (ref. 50; Box 3), this entangled state is stored in the quantum memory provided by the ensembles and is available 'on demand' for subsequent tasks, such as entanglement connection[13,51].

Although the above description is for an ideal case and neglects higher-order terms, the DLCZ protocol is designed to be resilient to

© 2008 Macmillan Publishers Limited. All rights reserved

Box 3 | Writing and reading single atomic excitations

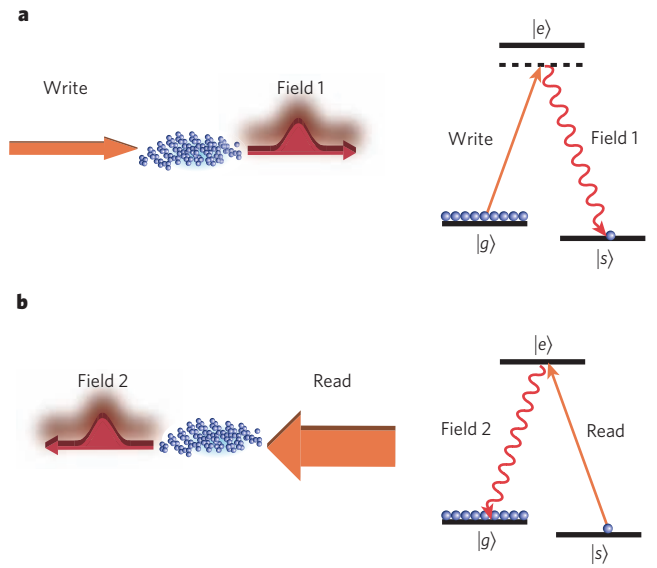

The DLCZ protocol[13] is based on ensembles of N_a identical atoms (blue) with a Λ-level configuration, as shown in the figure. The metastable lower states $|g\rangle$ and $|s\rangle$ can be, for example, atomic hyperfine states of the electronic ground level to ensure a long lifetime for coherence. All atoms are initially prepared in state $|g\rangle$ with no excitation (figure, panel **a**), namely $|0_a\rangle \equiv \otimes_i^{N_a}|g\rangle_i$, and a weak off-resonant 'write' pulse is then sent through the ensemble. This results in a small probability of amplitude $\sqrt{p}$ that one of the N_a atoms will be transferred from $|g\rangle$ to $|s\rangle$ and will emit a photon into the forward-scattered optical mode (designated field 1) with a frequency and/or polarization distinct from the write field.

For small excitation probability $p<<1$, in most cases nothing happens as a result of the writing pulse, so the resultant state $|\phi_{a,1}\rangle$ for the atomic ensemble and field 1 in the ideal case is given by

$$|\phi_{a,1}\rangle \quad |0_a\rangle|0_1\rangle + e^{i\beta}\sqrt{p}|1_a\rangle|1_1\rangle + O(p) \qquad (1)$$

where $|n_1\rangle$ is the state of the forward-propagating field 1 with n_1 photons ($n_1 = 0$ or 1), the phase β is determined by the propagation phases of the write pulse and field 1, and $O(p)$ denotes of order p. The atomic state $|1_a\rangle$ in equation (1) (above) is a collective (entangled) state with one excitation shared symmetrically between the N_a atoms (that is, one 'spin flip' from $|g\rangle$ to $|s\rangle$), where in the ideal case[13]

$$|1_a\rangle = \frac{1}{\sqrt{N_a}}\sum_{i=1}^{N_a}|g\rangle_i \cdots |s\rangle_i \cdots |g\rangle_{N_a} \qquad (2)$$

Field 1 is directed to a single-photon detector, where a detection event is recorded with probability p. Such an event for field 1 heralds that a single excitation (or spin flip from $|g\rangle$ to $|s\rangle$) has been created and stored in the atomic ensemble in the state $|1_a\rangle$ with high probability. Higher-order processes with multiple atomic and field 1 excitations are also possible and ideally occur, to lowest order, with probability p^2.

After a user-defined delay (subject to the finite lifetime of the quantum memory), the collective atomic excitation $|1_a\rangle$ can be efficiently converted to a propagating beam (designated field 2) by way of a strong 'read' pulse (figure, panel **b**), where in the ideal case there is a one-to-one transformation of atomic excitation to field excitation, $|1_a\rangle$ to $|1_2\rangle$. In the case of resonance with the transition from $|s\rangle$ to $|e\rangle$, the reading process utilizes the phenomenon of electromagnetically induced transparency[16,66].

important sources of imperfections, including losses in propagation and detection, and detector dark counts. Indeed, the scheme functions with 'built-in entanglement purification'[13] and enables entanglement to be extended beyond the separation of two ensembles in an efficient and scalable manner. Theoretical extensions[52,53] of the DLCZ protocol have examined related network architectures for optimizing scalability in view of laboratory capabilities (discussed below).

Coherence and entanglement with atomic ensembles

The initial, enabling, steps in the implementation of the DLCZ protocol were observations of quantum correlations both for single photon pairs[54,55] and for a large number of photons (10^3–10^4) (ref. 56) generated in the collective emission from atomic ensembles. Single photons were generated by the efficient mapping of stored collective atomic excitation to propagating wave packets for field 2 (refs 57–61; Box 3). Conditional read-out efficiencies of 50% in free space[58] and 84% in a cavity[62] were realized for state transfer from a single collective 'spin' excitation stored in the atomic ensemble to a single photon for field 2.

With these capabilities for coherent control of collective atomic emission, heralded entanglement between ensembles separated by 3 m was achieved in 2005 (ref. 49). More recent work has led to the inference that the concurrence C (ref. 63) of entanglement stored between the two ensembles in Fig. 3 is $C = 0.9\pm0.3$ (ref. 50), with the associated density matrix shown in Fig. 3b.

The DLCZ protocol is based on a quantum-repeater architecture involving independent operations on parallel chains of quantum systems[13], with scalability relying crucially on conditional control of quantum states stored in remote quantum memories[64]. The experiment shown in Fig. 3c took an important step towards this goal by achieving the minimal functionality required for scalable quantum networks[65].

Apart from the DLCZ protocol, which involves measurement-induced entanglement, it is also possible to achieve deterministic mapping of quantum states of light into and out of atomic ensembles by using electromagnetically induced transparency[16,66]. Pioneering work[67,68] demonstrated the storage and retrieval of classical pulses to and from an atomic ensemble. This work was then extended into the quantum regime of single photons[69,70]. Entanglement between two ensembles coupled to a cavity mode was achieved by adiabatic transfer of excitation[71], thereby providing a means for on-demand entanglement. In addition, the reversible mapping of photonic entanglement into and out of pairs of quantum memories has been achieved[19] by an electromagnetically-induced-transparency process, which should assist the distribution of entanglement over quantum networks (Fig. 1d).

Contemporary with this work on heralded and deterministic entanglement, a variety of experiments based on entanglement as a postdiction have been carried out[72] (that is, for cases in which a physical state is not available for use in a scalable network but which are nonetheless significant). An important advance in this regard is the use of a pair of ensembles for entanglement generation to achieve *a posteriori* teleportation of light to an atomic memory[73].

There has also been considerable effort devoted to the detailed characterization of decoherence for stored atomic excitation and entanglement[50,65,73]. Decoherence of entanglement between distinct atomic ensembles has been observed in the decay of the violation of Bell's inequality[65] and of the fidelity for teleportation[73]. By measuring concurrence $C(t)$, quantitative characterizations of the relationship between the global evolution of the entangled state and the temporal dynamics of various local correlations were also able to be made[50].

Extending entanglement for quantum networks

The entangled states that have been created so far both in cavity QED and by using the DLCZ protocol are between pairs of systems (known as bipartite entanglement) for which there are definitive procedures for operational verification[72]. The creation of more-general classes of entangled state shared between more than two nodes would be of great interest. However, as researchers progress towards more-complex quantum networks, the issue of entanglement verification becomes increasingly problematic. At present, the theoretical tools and experimental

© 2008 Macmillan Publishers Limited. All rights reserved

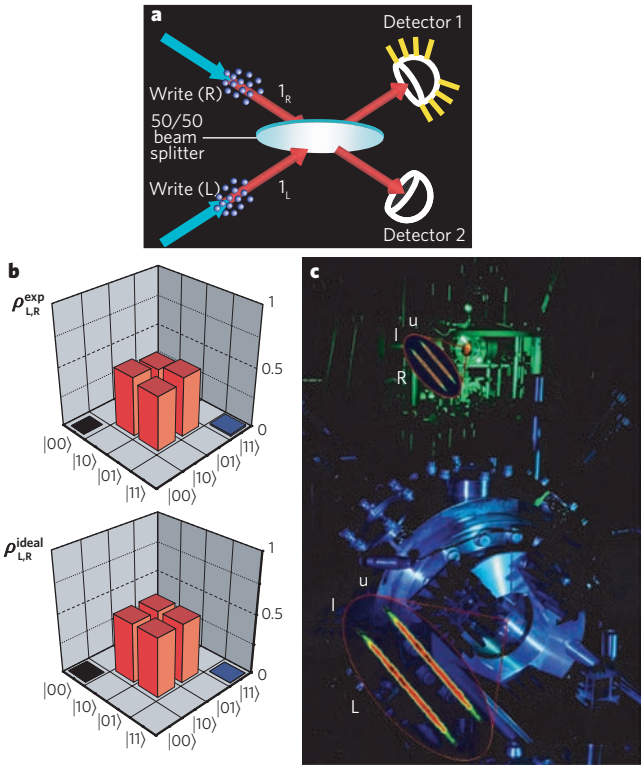

Figure 3 | Fundamentals of the DLCZ protocol. A realistic scheme for entanglement distribution by way of a quantum-repeater architecture was proposed by Duan, Lukin, Cirac and Zoller and is known as the DLCZ protocol[13]. **a**, Measurement-induced entanglement between two atomic ensembles[13,49], L and R, is shown. Synchronized laser pulses incident on the ensembles (denoted write beams, blue arrows) generate small amplitudes for optical fields from spontaneous Raman scattering[48]; these fields are denoted 1_L and 1_R (red arrows). These fields interfere at a 50/50 beam splitter, with outputs directed to two single-photon detectors. A measurement event at either detector (shown for detector 1) projects the ensembles into the entangled state $|\Psi_{L,R}\rangle$ with one quantum of excitation shared remotely between the ensembles. Entanglement is stored in the quantum memory provided by the ensembles and can subsequently be converted to propagating light pulses by a set of 'read' laser pulses (Box 3). **b**, Experimentally determined components of the density matrix $\rho^{exp}_{L,R}$ for entanglement between two atomic ensembles are shown[50], corresponding to concurrence $C = 0.9 \pm 0.3$, where $C = 0$ for an unentangled state. The first number in each ket refers to the excitation number for the ensemble L, and the second is for the ensemble R. For comparison, the density matrix $\rho^{ideal}_{L,R}$ for the ideal state $|\Psi_{L,R}\rangle$ is shown, with concurrence $C = 1$. **c**, The laboratory set-up is shown for the entanglement of two pairs of atomic ensembles to generate the functional quantum nodes L and R, which are separated by 3 m (ref. 65). Each of the four elongated ovals shows a cylinder of 10^5 caesium atoms, which forms an atomic ensemble at each site. Entangled states between the upper u and lower l pairs at the L and R nodes, $|\Psi^u_{L,R}\rangle|\Psi^l_{L,R}\rangle$, are generated and stored in an asynchronous manner for each pair (u and l) as is the case in panel **a**. Atomic excitations for the pairs L_u, L_l and R_u, R_l are subsequently converted to flying photons at each node, with a polarization encoding that results in violation of Bell's inequality[65]. The entire experiment functions under the quantum control of single photon detection events.

capabilities for characterizing the general states of quantum networks do not exist.

Perhaps surprisingly, a non-trivial task will be to find out whether a quantum network 'works'. As moderately complex quantum networks are realized in the laboratory, it will become increasingly more difficult to assess the characteristics of a network quantitatively, including whether entanglement extends across the whole network. One strategy, motivated by the underlying physical processes of the network, could be to try to determine the density matrix $\rho(t)$ for the network. However, this approach would fail because of the exponential growth in $\rho(t)$ with the size of a network.

An alternative strategy could be based on more functional issues of algorithmic capability. An attempt could be made to implement a quantum algorithm for computation or communication to test whether the purported quantum network has greater capabilities than any classical counterpart. This course is, however, problematic because the advantage of a quantum network might only be realized above some threshold in the size of the network. Furthermore, from an experimental perspective, this strategy does not offer much in the way of diagnostics for 'fixing' the network when it fails.

Another, less obvious, approach might be to adopt more seriously the perspective of a quantum network as a quantum many-body system and to search for more 'physical' characteristics of the network (for example, the scaling behaviour of pair correlation functions and multipartite entanglement). Indeed, an active area of research is the nature of entanglement for systems that undergo quantum phase transitions, and there have been pioneering advances in the study of one-dimensional spin chains[74].

Conclusion

Progress has been made towards the development of quantum networks, but the current state of the art is primitive relative to that required for the robust and scalable implementation of sophisticated network protocols, whether over short or long distances. The realization of quantum memories, local quantum processing, quantum repeaters and error-corrected teleportation are ambitious goals. Nevertheless, there is considerable activity directed towards these goals worldwide.

Here cavity-QED-based networks and networks implemented using the DLCZ protocol were considered separately, but it is clear that quantum networks will evolve as heterogeneous entities. For example, the same protocol that creates the entanglement between the two ensembles shown in Fig. 3a can be used to create an entangled state with one excitation shared between an atom in a cavity and an atomic ensemble. A crucial task will be the development of unambiguous procedures for verifying entanglement, a non-trivial undertaking that has not always been carried out correctly[72].

I have used quantum networks as a unifying theme, but the research described here has broader value, including advancing the understanding of quantum dynamical systems and, for the cases considered here, creating new physics from controlled nonlinear interactions of single photons and atoms. These are exciting times in quantum information science as researchers pass from the regime of individual building blocks (for example, a single atom–cavity system) to the realm of complex quantum systems that are assembled block by block from many such units. ■

1. Nielsen, M. A. & Chuang, I. L. *Quantum Computation and Quantum Information* (Cambridge Univ. Press, Cambridge, UK, 2000).
2. Zoller, P. *et al.* Quantum information processing and communication. Strategic report on current status, visions and goals for research in Europe. *Eur. Phys. J. D* **36,** 203–228 (2005).
3. Bennett, C. H., Brassard, G. & Ekert, A. K. Quantum cryptography. *Sci. Am.* **267** (4), 50–57 (1992).
4. Bouwmeester, D., Ekert, A. & Zeilinger, A. (eds) *The Physics of Quantum Information* (Springer, Berlin, 2000).
5. Giovannetti, V., Lloyd, S. & Maccone, L. Quantum-enhanced measurements: beating the standard quantum limit. *Science* **306,** 1330–1336 (2004).
6. Cirac, J. I., Zoller, P., Kimble, H. J. & Mabuchi, H. Quantum state transfer and entanglement distribution among distant nodes in a quantum network. *Phys. Rev. Lett.* **78,** 3221–3224 (1997).
7. Preskill, J. P. Plug-in quantum software. *Nature* **402,** 357–358 (1999).
8. Copsey, D. *et al.* Toward a scalable, silicon-based quantum computing architecture. *IEEE J. Quantum Electron.* **9,** 1552–1569 (2003).
9. Illuminati, D. Light does matter. *Nature Phys.* **2,** 803–804 (2006).
10. Duan, L.-M., Wang, B. & Kimble, H. J. Robust quantum gates on neutral atoms with cavity-assisted photon scattering. *Phys. Rev. A* **72,** 032333 (2005).
11. Acín, A., Cirac, J. I. & Lewenstein, M., Entanglement percolation in quantum networks. *Nature Phys.* **3,** 256–259 (2007).
12. Miller, R. *et al.* Trapped atoms in cavity QED: coupling quantized light and matter. *J. Phys. B.* **38,** S551–S565 (2005).
13. Duan, L.-M., Lukin, M. D., Cirac, J. I. & Zoller, P. Long-distance quantum communication with atomic ensembles and linear optics. *Nature* **414,** 413–418 (2001).
14. Parkins, A. S., Marte, P., Zoller, P. & Kimble, H. J. Synthesis of arbitrary quantum states via adiabatic transfer of Zeeman coherence. *Phys. Rev. Lett.* **71,** 3095–3098 (1993).

© 2008 Macmillan Publishers Limited. All rights reserved

15. van Enk, S. J., Cirac, J. I. & Zoller, P. Photonic channels for quantum communication. *Science* **279,** 205–208 (1998).
16. Lukin, M. D. Trapping and manipulating photon states in atomic ensembles. *Rev. Mod. Phys.* **75,** 457–472 (2003).
17. Briegel, H.-J., Dür, W., Cirac, J. I. & Zoller, P. Quantum repeaters: the role of imperfect local operations in quantum communication. *Phys. Rev. Lett.* **81,** 5932–5935 (1998).
18. Boozer, A. D., Boca, A., Miller, R., Northup, T. E. & Kimble, H. J. Reversible state transfer between light and a single trapped atom. *Phys. Rev. Lett.* **98,** 193601 (2007).
19. Choi, K. S., Deng, H., Laurat, J. & Kimble, H. J. Mapping photonic entanglement into and out of a quantum memory. *Nature* **452,** 67–71 (2008).
20. Berman, P. (ed.) *Cavity Quantum Electrodynamics* (Academic, San Diego, 1994).
21. Wilk, T., Webster, S. C., Kuhn, A. & Rempe, G. Single-atom single-photon quantum interface. *Science* **317,** 488–490 (2007).
22. Walther, H. Quantum optics of single atoms. *Fortschr. Phys.* **52,** 1154–1164 (2004).
23. Meschede, D., Walther, H. & Mueller, G. One-atom maser. *Phys. Rev. Lett.* **54,** 551–554 (1985).
24. Raimond, J. M. *et al.* Probing a quantum field in a photon box. *J. Phys. B* **38,** S535–S550 (2005).
25. Guerlin, C. *et al.* Progressive field-state collapse and quantum non-demolition photon counting. *Nature* **448,** 889–893 (2007).
26. Vahala, K. J. Optical microcavities. *Nature* **424,** 839–846 (2004).
27. Khitrova, G., Gibbs, H. M., Kira, M., Koch, S. W. & Scherer, A. Vacuum Rabi splitting in semiconductors. *Nature Phys.* **2,** 81–90 (2006).
28. Schoelkopf, R. J. & Girvin, S. M. Wiring up quantum systems. *Nature* **451,** 664–669 (2008).
29. Ye, J., Vernooy, D. W. & Kimble, H. J. Trapping of single atoms in cavity QED. *Phys. Rev. Lett.* **83,** 4987–4990 (1999).
30. Hijlkema, M. *et al.* A single-photon server with just one atom. *Nature Phys.* **3,** 253–255 (2007).
31. Fortier, K. M., Kim, S. Y., Gibbons, M. J. Ahmadi, P. & Chapman, M. S. Deterministic loading of individual atoms to a high-finesse optical cavity. *Phys. Rev. Lett.* **98,** 233601 (2007).
32. Ye, J., Kimble, H. J. & Katori, H. Quantum state engineering and precision metrology using state-insensitive light traps. *Science* (in the press).
33. Boozer, A. D., Boca, A., Miller, R., Northup, T. E. & Kimble, H. J. Cooling to the ground state of axial motion for one atom strongly coupled to an optical cavity. *Phys. Rev. Lett.* **97,** 083602 (2006).
34. Keller, M., Lange, B., Hayasaka, K., Lange, W. & Walther, H. Continuous generation of single photons with controlled waveform in an ion-trap cavity system. *Nature* **431,** 1075–1078 (2004).
35. Duan, L.-M. & Kimble, H. J. Scalable photonic quantum computation through cavity-assisted interactions. *Phys. Rev. Lett.* **92,** 127902 (2004).
36. McKeever, J. *et al.* Deterministic generation of single photons from one atom trapped in a cavity. *Science* **303,** 1992–1994 (2004).
37. Bergmann, K., Theuer, H. & Shore, B. W. Coherent population transfer among quantum states of atoms and molecules. *Rev. Mod. Phys.* **70,** 1003–1025 (1998).
38. Lounis, B. & Orrit, M. Single-photon sources. *Rep. Prog. Phys.* **68,** 1129–1179 (2005).
39. Lange, W. & Kimble, H. J. Dynamic generation of maximally entangled photon multiplets by adiabatic passage. *Phys. Rev. A* **61,** 063817 (2000).
40. Duan, L.-M. & Kimble, H. J. Efficient engineering of multiatom entanglement through single-photon detections. *Phys. Rev. Lett.* **90,** 253601 (2003).
41. Sun, B., Chapman, M. S. & You, L. Atom–photon entanglement generation and distribution. *Phys. Rev. A* **69,** 042316 (2004).
42. Englund, D., Faraon, A., Zhang, B., Yamamoto, Y. & Vuckovic, J. Generation and transfer of single photons on a photonic crystal chip. *Opt. Express* **15,** 5550–5558 (2007).
43. Schön, C., Solano, E., Verstraete, F., Cirac, J. I. & Wolf, M. M. Sequential generation of entangled multiqubit states. *Phys. Rev. Lett.* **95,** 110503 (2005).
44. Parkins, A. S. & Kimble, H. J. Quantum state transfer between motion and light. *J. Opt. B* **1,** 496–504 (1999).
45. Julsgaard, B., Kozhekin, A. & Polzik, E. S. Experimental long-lived entanglement of two macroscopic objects. *Nature* **413,** 400–403 (2001).
46. Sherson, J. F. *et al.* Quantum teleportation between light and matter. *Nature* **443,** 557–560 (2006).
47. Cerf, N. J., Leuchs, G. & Polzik, E. S. (eds) *Quantum Information with Continuous Variables of Atoms and Light* (World Scientific, New Jersey, 2007).
48. Raymer, M. G., Walmsley, I. A., Mostowski, J. & Sobolewska, B. Quantum theory of spatial and temporal coherence properties of stimulated Raman scattering. *Phys. Rev. A* **32,** 332–344 (1985).
49. Chou, C.-W. *et al.* Measurement-induced entanglement for excitation stored in remote atomic ensembles. *Nature* **438,** 828–832 (2005).
50. Laurat, J., Choi, K. S., Deng, H., Chou, C.-W. & Kimble, H. J. Heralded entanglement between atomic ensembles: preparation, decoherence, and scaling. *Phys. Rev. Lett.* **99,** 180504 (2007).
51. Laurat, J. *et al.* Towards experimental entanglement connection with atomic ensembles in the single excitation regime. *New J. Phys.* **9,** 207–220 (2007).
52. Jiang, L., Taylor, J. M. & Lukin, M. D. Fast and robust approach to long-distance quantum communication with atomic ensembles. *Phys. Rev. A* **76,** 012301 (2007).
53. Sangouard, N. *et al.* Robust and efficient quantum repeaters with atomic ensembles and linear optics. Preprint at http://arxiv.org/abs/0802.1475) (2008).
54. Kuzmich, A. *et al.* Generation of nonclassical photon pairs for scalable quantum communication with atomic ensembles. *Nature* **423,** 731–734 (2003).
55. Balic, V., Braje, D. A., Kolchin, P., Yin, G. Y. & Harris, S. E. Generation of paired photons with controllable waveforms. *Phys. Rev. Lett.* **94,** 183601 (2005).
56. van der Wal, C. H. *et al.* Atomic memory for correlated photon states. *Science* **301,** 196–200 (2003).
57. Chou, C. W., Polyakov, S. V., Kuzmich, A. & Kimble, H. J. Single-photon generation from stored excitation in an atomic ensemble. *Phys. Rev. Lett.* **92,** 213601 (2004).
58. Laurat, J. *et al.* Efficient retrieval of a single excitation stored in an atomic ensemble. *Opt. Express* **14,** 6912–6918 (2006).
59. Thompson, J. K., Simon, J., Loh, H. & Vuletic, V. A high-brightness source of narrowband, identical-photon pairs. *Science* **313,** 74–77 (2006).
60. Matsukevich, D. N. *et al.* Deterministic single photons via conditional quantum evolution. *Phys. Rev. Lett.* **97,** 013601 (2006).
61. Chen, S. *et al.* Deterministic and storable single-photon source based on a quantum memory. *Phys. Rev. Lett.* **97,** 173004 (2006).
62. Simon, J., Tanji, H., Thompson, J. K. & Vuletic, V. Interfacing collective atomic excitations and single photons. *Phys.Rev. Lett.* **98,** 183601 (2007).
63. Wootters, W. K. Entanglement of formation of an arbitrary state of two qubits. *Phys. Rev. Lett.* **80,** 2245–2248 (1998).
64. Felinto, D. *et al.* Conditional control of the quantum states of remote atomic memories for quantum networking. *Nature Phys.* **2,** 844–848 (2006).
65. Chou, C.-W. *et al.* Functional quantum nodes for entanglement distribution over scalable quantum networks. *Science* **316,** 1316–1320 (2007).
66. Harris, S. E. Electromagnetically induced transparency. *Phys. Today* **50,** 36–40 (1997).
67. Liu, C., Dutton, Z., Behroozi, C. H. & Hau, L. V. Observation of coherent optical information storage in an atomic medium using halted light pulses. *Nature* **409,** 490–493 (2001).
68. Phillips, D. F., Fleischhauer, A., Mair, A., Walsworth, R. L. & Lukin, M. D. Storage of light in atomic vapor. *Phys. Rev. Lett.* **86,** 783–786 (2001).
69. Chanelière, T. *et al.* Storage and retrieval of single photons transmitted between remote quantum memories. *Nature* **438,** 833–836 (2005).
70. Eisaman, M. D. *et al.* Electromagnetically induced transparency with tunable single-photon pulses. *Nature* **438,** 837–841 (2005).
71. Simon, J., Tanji, H., Ghosh, S. & Vuletic, V. Single-photon bus connecting spin-wave quantum memories. *Nature Phys.* **3,** 765–769 (2007).
72. van Enk, S. J., Lütkenhaus, N. & Kimble, H. J. Experimental procedures for entanglement verification. *Phys. Rev. A* **75,** 052318 (2007).
73. Chen, Y.-A. *et al.* Memory-built-in quantum teleportation with photonic and atomic qubits. *Nature Phys.* **4,** 103–107 (2008).
74. Vidal, G., Latorre, J. I., Rico, E. & Kitaev, A. Entanglement in quantum critical phenomena. *Phys. Rev. Lett.* **90,** 227902 (2003).
75. Aoki, T. *et al.* Observation of strong coupling between one atom and a monolithic microresonator. *Nature* **443,** 671–674 (2006).
76. Dayan, B. *et al.* A photon turnstile dynamically regulated by one atom. *Science* **319,** 1062–1065 (2008).
77. Spillane, S. M. *et al.* Ultrahigh-*Q* toroidal microresonators for cavity quantum electrodynamics. *Phys. Rev. A* **71,** 013817 (2005).
78. Trupke, M. *et al.* Atom detection and photon production in a scalable, open, optical microcavity. *Phys. Rev. Lett.* **99,** 063601 (2007).
79. Park, Y.-S., Cook, A. K. & Wang, H. Cavity QED with diamond nanocrystals and silica microspheres. *Nano Lett.* **6,** 2075–2079 (2006).
80. Armani, D. K., Kippenberg, T. J., Spillane, S. M. & Vahala, K. J. Ultra-high-*Q* toroid microcavity on a chip. *Nature* **421,** 925–928 (2003).
81. Spillane, S. M., Kippenberg, T. J., Painter, O. J. & Vahala, K. J. Ideality in a fiber-taper-coupled microresonator system for application to cavity quantum electrodynamics. *Phys. Rev. Lett.* **91,** 043902 (2003).
82. Braginsky, V. B., Gorodetsky, M. L. & Ilchenko, V. S. Quality-factor and nonlinear properties of optical whispering-gallery modes. *Phys. Lett. A* **137,** 393–397 (1989).

Acknowledgements I am grateful for the contributions of members of the Caltech Quantum Optics Group, especially K. S. Choi, B. Dayan and R. Miller. I am indebted to J. P. Preskill and S. J. van Enk for critical insights. My research is supported by the National Science Foundation, IARPA and Northrop Grumman Space Technology.

Author Information Reprints and permissions information is available at www.nature.com/reprints. The author declares no competing financial interests. Correspondence should be addressed to the author (hjkimble@caltech.edu).

© 2008 Macmillan Publishers Limited. All rights reserved

Superconducting quantum bits

John Clarke[1,2] & Frank K. Wilhelm[3]

Superconducting circuits are macroscopic in size but have generic quantum properties such as quantized energy levels, superposition of states, and entanglement, all of which are more commonly associated with atoms. Superconducting quantum bits (qubits) form the key component of these circuits. Their quantum state is manipulated by using electromagnetic pulses to control the magnetic flux, the electric charge or the phase difference across a Josephson junction (a device with nonlinear inductance and no energy dissipation). As such, superconducting qubits are not only of considerable fundamental interest but also might ultimately form the primitive building blocks of quantum computers.

The theory of quantum mechanics was originally developed to account for the observed behaviour of electrons in atoms. More than 80 years later, it is being used to explain the behaviour of superconducting circuits that can be hundreds of nanometres wide and can contain trillions of electrons. The quantum nature of these circuits is observable because they can be engineered to be isolated from the electrical environment and are thus represented by a single degree of freedom. Significant coupling to other degrees of freedom causes rapid decoherence, destroying the quantum state of the circuit so that it behaves classically. Unlike atoms, these circuits can be designed and constructed to tailor their characteristic frequencies, as well as other parameters. These frequencies can be controlled by adjusting an external parameter, and the coupling energy between two quantum bits (qubits) can be turned on and off at will.

Superconducting quantum circuits are the subject of intense research at present, in part because they have opened up a new area of fundamental science and in part because of their long-term potential for quantum computing. In this review, we begin with a brief discussion of superconductivity and two of the superconducting properties that underlie how qubits operate: flux quantization and Josephson tunnelling. The three fundamental types of superconducting qubit — flux, charge and phase — are then described. This is followed by a review of the real-time, quantum-coherent dynamics of qubits and the limitations imposed by relaxation and decoherence, as well as the mechanisms of decoherence. We then discuss schemes for controlling the coupling between two qubits, a feature that greatly simplifies the implementation of proposed quantum-computing architectures. And we finish by discussing quantum optics on a chip, a new research direction in which the electromagnetic fields associated with control and read-out signals are treated quantum mechanically.

Flux quantization and Josephson tunnelling

Why do superconductors enable atomic-scale phenomena to be observed at the macroscopic level? The reason, as explained elegantly by the theory of Bardeen, Cooper and Schrieffer[1], is that in a given superconductor all of the Cooper pairs of electrons (which have charge $2e$, mass $2m_e$ and spin zero, and are responsible for carrying a supercurrent) are condensed into a single macroscopic state described by a wavefunction $\Psi(\mathbf{r}, t)$ (where $\mathbf{r}$ is the spatial variable and t is time.) Like all quantum-mechanical wavefunctions, $\Psi(\mathbf{r}, t)$ can be written as $|\Psi(\mathbf{r}, t)| \exp[i\phi(\mathbf{r}, t)]$ (where $i = \sqrt{-1}$): that is, as the product of an amplitude and a factor involving the phase ϕ. Furthermore, in 'conventional' superconductors such as Nb, Pb and Al, the quasiparticles (electron-like and hole-like excitations) are separated in energy from the condensate[2] by an energy gap $\Delta_s(T) = 1.76k_BT_c$ (where k_B is the Boltzmann constant and T_c is the superconducting transition temperature). Thus, at temperatures $T << T_c$, the density of quasiparticles becomes exponentially small, as does the intrinsic dissipation for frequencies of less than $2\Delta_s(0)/h$ (where h is Planck's constant) — roughly 10^{11} Hz for Al.

The macroscopic wavefunction leads to two phenomena that are essential for qubits. The first phenomenon is flux quantization. When a closed ring is cooled through its superconducting transition temperature in a magnetic field and the field is then switched off, the magnetic flux Φ in the ring — maintained by a circulating supercurrent — is quantized[2] in integer values of the flux quantum $\Phi_0 \equiv h/2e \approx 2.07 \times 10^{-15}$ T m^2. This quantization arises from the requirement that $\Psi(\mathbf{r}, t)$ be single valued. The second phenomenon is Josephson tunnelling[2]. A Josephson junction consists of two superconductors separated by an insulating barrier of appropriate thickness, typically 2–3 nm, through which Cooper pairs can tunnel coherently. Brian Josephson showed that the supercurrent I through the barrier is related to the gauge-invariant phase difference $\delta(t)$ between the phases of the two superconductors by the current–phase relationship

$$I = I_0 \sin\delta \tag{1}$$

Here I_0 is the maximum supercurrent that the junction can sustain (that is, the critical current). This phase difference is an electrodynamic variable that, in the presence of a potential difference V between the superconductors, evolves in time as

$$\hbar\dot{\delta} = \hbar\omega = 2eV \tag{2}$$

where $\hbar = h/2\pi$ and ω is the angular frequency at which the supercurrent oscillates. The dynamical behaviour of Josephson junctions is described in Box 1.

The variables have, so far, been regarded as being classical, but to show quantum-mechanical behaviour, these variables must be replaced by operators. The two relevant operators are that for δ, which is associated with the Josephson coupling energy $E_j \equiv I_0\Phi_0/2\pi$, and that for the Cooper-pair number difference N across the capacitance, which is associated with the charging energy $E_c \equiv (2e)^2/2C$, where C is the junction capacitance.

Furthermore — just like the familiar position and momentum operators x and p_x — the operators for δ and for the charge on the capacitor Q

[1]Department of Physics,366 LeConte Hall, University of California, Berkeley, California 94720, USA. [2]Materials Sciences Division, Lawrence Berkeley National Laboratory, 1 Cyclotron Road, Berkeley, California 94720, USA. [3]Institute for Quantum Computing, University of Waterloo, 200 University Avenue West, Waterloo, Ontario N2L 3G1, Canada.

© 2008 Macmillan Publishers Limited. All rights reserved

Box 1 | The Josephson junction as a nonlinear circuit element

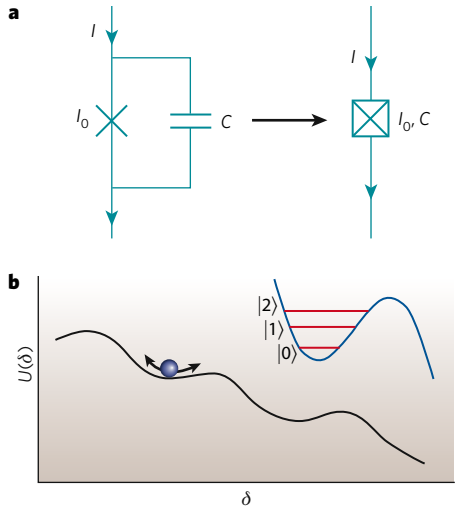

Equations (1) and (2) contain the crucial information that the Josephson junction is a dissipationless device with a nonlinear inductance. It is these unique features that make the junction the primitive building block of all superconducting qubits.

The nonlinear inductance is easily deduced by noting that the time derivative of equation (1) yields $\dot{I} = (I_0\cos\delta)\dot{\delta} = (I_0\cos\delta)\omega = V(2eI_0/\hbar)\cos\delta$ from equation (2). Invoking Faraday's law $V = -L\dot{I}$ (where L is the inductance) then leads to the Josephson inductance

$$|L_j| = \Phi_0/(2\pi I_0\cos\delta) = \Phi_0/2\pi(I_0^2 - I^2)^{1/2} \text{ (where } I < I_0) \qquad (6)$$

The Josephson junction, denoted by an X in panel **a** of the figure, has an intrinsic capacitance C; this combination is often denoted by an X in a box. I_0 denotes the critical current. It is immediately apparent from equation (6) that the junction is also a nonlinear oscillator with a resonant angular frequency $\omega_p(I) = (L_jC)^{-1/2} = (2\pi I_0/\Phi_0C)^{1/2}/(1 - I^2/I_0^2)^{1/4}$.

Considerable insight into the dynamics of a Josephson junction can be gleaned by considering the flow of a current J through the junction: $J = I_0\sin\delta + C\dot{V}$. Writing $\dot{V} = (\hbar/2e)\ddot{\delta}$ and rearranging this yields $(\hbar C/2e)\ddot{\delta} = I - I_0\sin\delta = -(2e/\hbar)\partial U/\partial\delta$. $U \equiv -(\Phi_0/2\pi)\partial U/\partial\delta$ is the potential of a tilted washboard for a particle of mass $\hbar C/2e$ (as illustrated in panel **b** of the figure). In the absence of fluctuations, for $I < I_0$ the particle remains trapped in one of the potential wells; classically, it oscillates in the well at the plasma oscillation frequency $\omega_p(I)/2\pi$. Thus, $\langle\dot{\delta}\rangle = 0$, and the junction is in the zero-voltage state; in the quantum picture, the energy in the well is quantized, as shown in the inset (figure, panel **b**). By contrast, when I is increased so that $I > I_0$, the particle runs down the washboard, $\langle\dot{\delta}\rangle > 0$, and there is a voltage across the junction. When I is subsequently reduced so that $I < I_0$, the particle will continue to propagate until I is close to 0. Thus, the current–voltage characteristic is hysteretic.

are canonically conjugate, as expressed by the commutator bracket $[\delta, Q] = i2e$. The fact that δ and Q are subject to Heisenberg's uncertainty principle has far-reaching consequences. On the one hand, when $E_j >> E_c$, δ is well defined, and Q has large quantum fluctuations; therefore, the Josephson behaviour of the junction dominates. On the other hand, when $E_j << E_c$, N is well defined, and δ has large quantum fluctuations; therefore, the charging behaviour of the capacitor dominates. Using these ideas, the parameters of superconducting quantum circuits can be designed[3].

The first evidence of quantum behaviour in a Josephson junction came from experiments in which macroscopic quantum tunnelling was found to occur and energy levels were shown to be quantized. In macroscopic quantum tunnelling[4,5], the junction tunnels from the ground state $|0\rangle$ (Box 1 figure), when $I < I_0$, through the potential barrier that separates it from its neighbouring energy well, which is at a lower energy. Then, the particle runs freely down the washboard potential, generating a voltage $2\Delta_s/e$ that is readily detected. These results[5] were found to be in strong agreement with theory[6]. Energy quantization[7] was found in the initial well by irradiating the junction with microwaves. The escape rate from the zero-voltage state was increased when the microwave frequency f_m corresponded to the energy difference between two adjacent energy levels. A crucial point is that the anharmonic nature of the well, which results from the nonlinear inductance of Josephson junctions (equation (6), Box 1), causes the energy spacing to decrease as the quantum number progressively increases, so each transition has a distinct frequency. If the well were harmonic, the energy spacings would be identical, and the quantum case would not be distinguishable from the classical case.

These experiments showed unequivocally that δ is a quantum variable. The next step in the demonstration of macroscopic quantum physics was to implement devices showing the superposition of two quantum states $|\Psi_1\rangle$ and $|\Psi_2\rangle$ in the form $|\Psi\rangle = \alpha|\Psi_1\rangle + \beta|\Psi_2\rangle$, as first proposed by Anthony Leggett[8] in the 1980s in his discussion of macroscopic quantum coherence in superconducting devices. In 1997, Yasunobu Nakamura *et al.*[9] carried out the first such experiment on a charge qubit, showing spectroscopically the superposition of the Cooper-pair states $|n\rangle$ and $|n+1\rangle$, where the integer n is the quantum number specifying the number of Cooper pairs. Subsequently, in 2000, Jonathan Friedman *et al.*[10] and Caspar van der Wal *et al.*[11] showed the superposition of states in a flux qubit. A flux qubit consists of a superconducting loop interrupted by one[10] or three[11] Josephson junctions. The two quantum states are flux pointing up and flux pointing down or, equivalently, supercurrent flowing in an anticlockwise direction and supercurrent flowing in a clockwise direction. In 2002, Denis Vion *et al.*[12] described 'quantronium', a qubit in which two small junctions are connected by a superconducting island, involving the superposition of the Cooper-pair states $|n\rangle$ and $|n+1\rangle$. Also in 2002, John Martinis *et al.*[13] demonstrated a phase qubit, a reinvention of the device used earlier to observe quantized energy levels[7]. The relevant quantum states are the ground state and the first excited state. Some of the experimental difficulties encountered when operating superconducting qubits are described in Box 2.

Flux qubits

A flux qubit, as indicated earlier, consists of a superconducting loop interrupted by one[10] or three[11] Josephson junctions (Fig. 1a). Although both designs function similarly, we focus on the three-junction design, which has been adopted more widely. In this device, one junction is smaller in area and thus has a smaller critical current than the other two, which function to increase the inductance of the loop. The small junction has a large value for E_j/E_c, typically 50, so the phase difference δ (or, equivalently, the magnetic flux Φ in the loop) is the relevant quantum variable. The two quantum states are magnetic flux pointing up $|\uparrow\rangle$ and magnetic flux pointing down $|\downarrow\rangle$ or, equivalently, anticlockwise qubit supercurrent I_q circulating in the loop and clockwise supercurrent. The qubit is represented by a double-well potential, which is generally asymmetrical. The two states are coupled by the quantum-mechanical tunnelling of δ through the barrier separating the wells, giving rise to the superposition of the two basis states

$$|\Psi\rangle = \alpha|\uparrow\rangle \pm \beta|\downarrow\rangle \qquad (3)$$

When the externally applied magnetic flux $\Phi_e = \Phi_0/2$, the double-well potential becomes symmetrical (Fig. 1b), and the two eigenfunctions become symmetrical and antisymmetrical superpositions of the two basis states, with $\alpha = \beta = 1/\sqrt{2}$. At this degeneracy point, the splitting of the energy levels of the ground state $|0\rangle$ and the first excited state $|1\rangle$ is Δ; away from the degeneracy point, the energy difference is

$$\nu = (\Delta^2 + \varepsilon^2)^{1/2} \qquad (4)$$

where $\varepsilon = 2I_q(\Phi_e - \Phi_0/2)$ (Fig. 1c). The probabilities of observing the states $|\uparrow\rangle$ and $|\downarrow\rangle$ in the ground and first excited states as a function

© 2008 Macmillan Publishers Limited. All rights reserved

Box 2 | Experimental issues with superconducting qubits

Experiments on superconducting qubits are challenging. Most superconducting qubits are created by using electron-beam lithography, need millikelvin temperatures and an ultralow-noise environment to operate, and can be studied only by using very sensitive measurement techniques.

Superconducting qubits generally require Josephson junctions with dimensions of the order of $0.1 \times 0.1\,\mu m^2$ — corresponding to a self-capacitance of about 1 fF — and are patterned by using shadow evaporation and electron-beam lithography[79]; an exception is the phase qubit, which typically has a junction of $1 \times 1\,\mu m^2$ and can be patterned photolithographically. The Josephson junctions are usually Al–Al_xO_y–Al (where $x \leq 2$ and $y \leq 3$), and the oxidation must be controlled to yield relatively precise values of E_J and E_C. Because qubit frequencies are usually 5–10 GHz (which corresponds to 0.25–0.5 K), the circuits are operated in dilution refrigerators, typically at temperatures of 10–30 mK, to minimize thermal population of the upper state.

Great efforts are made to attenuate external electrical and magnetic noise. The experiment is invariably enclosed in a Faraday cage — either a shielded room or the metal Dewar of the refrigerator with a contiguous metal box on top. The electrical leads that are connected to the qubits and their read-out devices are heavily filtered or attenuated. For example, lines carrying quasistatic bias currents usually have multiple low-pass filters at the various temperature stages of the refrigerator. These include both inductor–capacitor and resistor–capacitor filters that operate up to a few hundred megahertz, as well as wires running through copper powder, which results in substantial loss at higher frequencies[5]. The overall attenuation is typically 200 dB. Finally, the read-out process for probing a quantum system is very delicate.

of Φ_e are shown in Fig. 1d. At the degeneracy point, the probability of observing either state is ½. As Φ_e is reduced, the probability of observing $|\uparrow\rangle$ increases while that of observing $|\downarrow\rangle$ decreases.

The first observation of quantum superposition in a flux qubit was made spectroscopically. The state of the flux qubit is measured with a d.c. superconducting quantum interference device (SQUID)[14]. This device consists of two Josephson junctions, each with critical current I_0, connected in parallel on a superconducting loop of inductance L. The critical current of the SQUID $I_c(\Phi_s)$ is periodic in the externally applied magnetic flux Φ_s with period Φ_0. In the limit $\beta_L \equiv 2LI_0/\Phi_0 << 1$ in which the Josephson inductance dominates the geometrical inductance, the critical current for $\Phi_s = (m + ½)\Phi_0$ (m is an integer) is reduced to almost zero, and the flux dependence of the critical current takes the approximate form[14] $I_c(\Phi_s) \approx 2I_0|\cos(\pi\Phi_s/\Phi_0)|$. Thus, by biasing the SQUID with a constant magnetic flux near $\Phi_0/2$, and measuring the critical current, the changes in flux produced by a nearby qubit can be measured with high sensitivity. In most experiments with qubits, a pulse of current is applied to the SQUID, which either remains in the zero-voltage state or makes a transition to the voltage state, producing a voltage $2\Delta_s/e$. Because its current–voltage characteristic is hysteretic, the SQUID remains at this voltage until the current bias has been removed, allowing researchers to determine whether the SQUID has switched. For sufficiently small current pulses, the probability of the SQUID switching is zero, whereas the probability is one for sufficiently large pulses. The switching event is a stochastic process and needs to be repeated many times for the flux in the SQUID to be measured accurately.

The first step in spectroscopic observation of quantum superposition is to determine the height of the current pulse at which the SQUID switches — with, for example, a probability of ½ — as a function of Φ_e over a narrow range (perhaps $\pm 5m\Phi_0$). Subsequently, a pulse of microwave flux is applied at frequency f_m, which is of sufficient amplitude and duration to equalize the populations of the ground state and first excited state when the energy-level splitting difference $\nu = hf_m$. Assuming that $|\uparrow\rangle$ is measured, then, on resonance, there will be a peak in the switching probability for $\Phi_e < \Phi_0/2$ and a corresponding dip for $\Phi_e > \Phi_0/2$. An example of these results[11,15] is shown in Fig. 2. The configuration of the qubit and the SQUID is shown in Fig. 2a, and the peaks and dips in the amplitude of the switching current

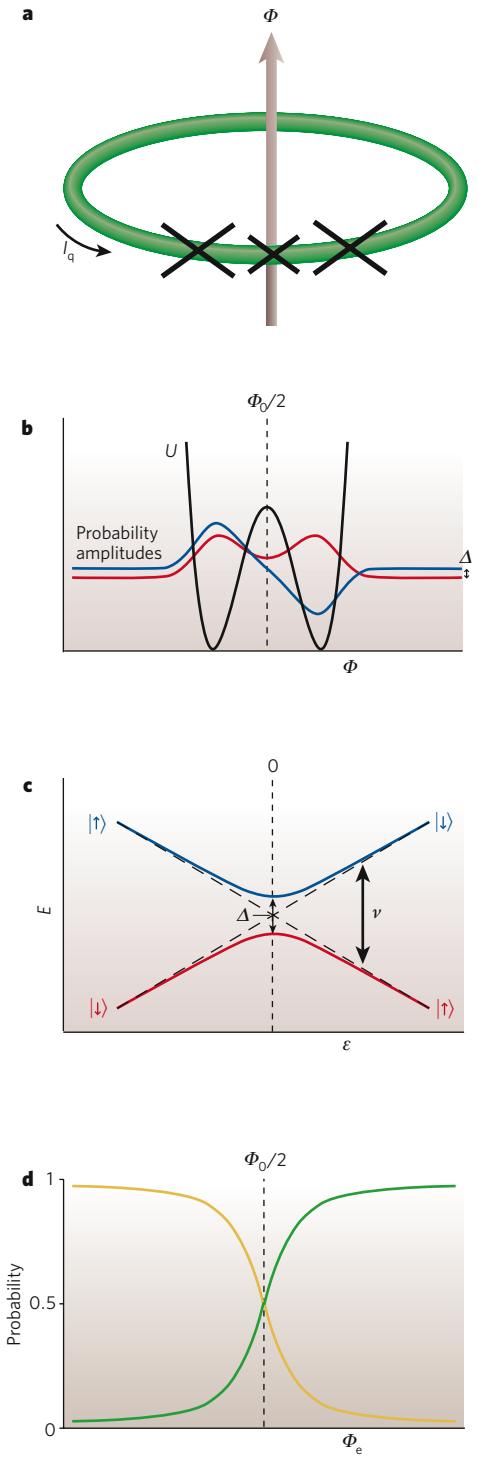

Figure 1 | The theory underlying flux qubits. **a**, Flux qubits consist of a superconducting loop interrupted by either one or three (shown) Josephson junctions. The two quantum states are magnetic flux Φ pointing up $|\uparrow\rangle$ and Φ pointing down $|\downarrow\rangle$ or, equivalently, supercurrent I_q circulating in the loop anticlockwise and I_q circulating clockwise. **b**, The double-well potential (black) versus total flux Φ contained in a flux qubit is shown. The two wells are symmetrical when the externally applied magnetic flux Φ_e is $(n + ½)\Phi_0$, where n is an integer (n = 0 in this case). The coloured curves are the eigenfunctions (probability amplitudes) for the ground state (symmetrical; red) and first excited state (antisymmetrical; blue). **c**, The energy E of the two superpositions states in **b** versus the energy bias $\varepsilon = 2I_q(\Phi_e - \Phi_0/2)$ is shown. The diagonal dashed black lines show the classical energies. The energy-level splitting is Δ at the degeneracy point, $\varepsilon = 0$, and is ν for $\varepsilon \neq 0$. **d**, The probabilities of the qubit flux pointing up (green) or down (yellow) in the ground state versus applied flux are shown.

© 2008 Macmillan Publishers Limited. All rights reserved

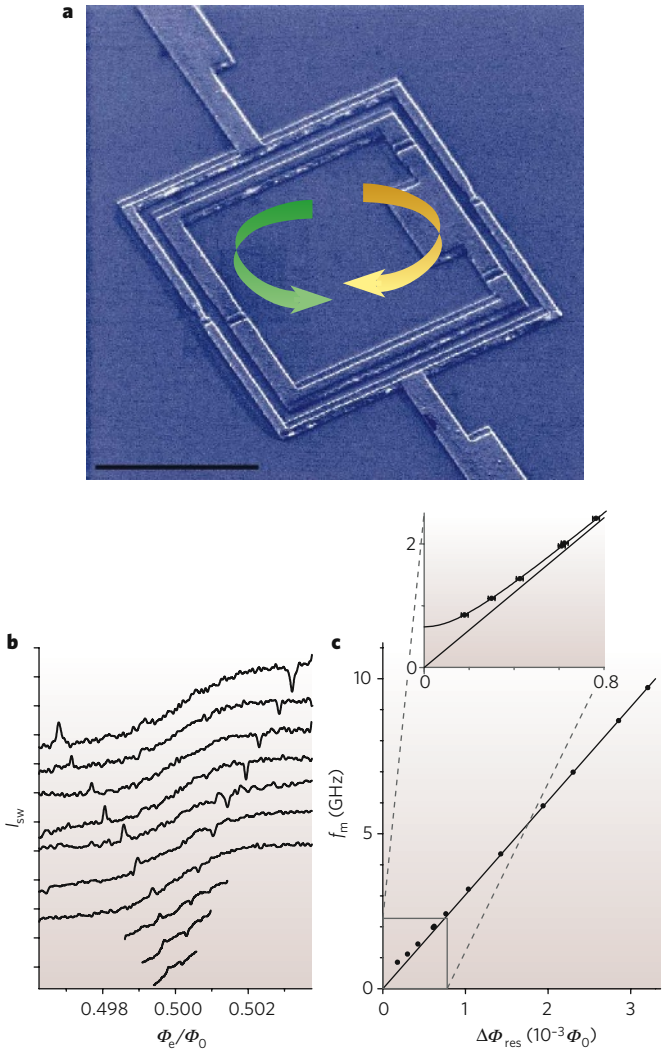

Figure 2 | Experimental properties of flux qubits. a, The configuration of the original three-junction flux qubit is shown. Arrows indicate the current flow in the two qubit states (green denotes $|\uparrow\rangle$, and yellow denotes $|\downarrow\rangle$). Scale bar, 3 μm. (Image courtesy of C. H. van der Wal, Rijksuniversiteit Groningen, the Netherlands). **b**, Radiation of microwave frequency f_m induces resonant peaks and dips in the switching current I_{sw} with respect to the externally applied magnetic flux Φ_e normalized to the flux quantum Φ_0. Frequencies range from 9.711 GHz to 0.850 GHz. Tick marks on the *y* axis show steps of 0.4 nA. (Panel reproduced, with permission, from ref. 15.) **c**, Microwave frequency f_m is plotted against half of the separation in magnetic flux, $\Delta\Phi_{res}$, between the peak and the dip at each frequency. The line is a linear fit through the data at high frequencies and represents the classical energy. The inset is a magnified view of the lower part of the graph; the curved line in the inset is a fit to equation (4). The deviation of the data points from the straight line demonstrates quantum coherence of the $|\uparrow\rangle$ and $|\downarrow\rangle$ flux states. (Panel reproduced, with permission, from ref. 15.)

versus applied flux are shown in Fig. 2b for a succession of microwave frequencies. As expected, the difference in the applied flux at which the peaks and dips appear, $2\Delta\Phi_{res}$, becomes greater as the microwave frequency increases. The microwave frequency versus $\Delta\Phi_{res}$ is shown in Fig. 2c. The data have been fitted to equation (4) with $I_q = (\frac{1}{2})\mathrm{d}\nu/\mathrm{d}\Phi_e$ in the limit $\nu >> \Delta$, using Δ as a fitting parameter. The data reveal the existence of an anticrossing (that is, an avoided crossing) at $\Phi_e = \Phi_0/2$.

Charge qubits

A charge qubit (also known as a Cooper-pair box) is shown in Fig. 3a, b. The key component is a tiny superconducting island that is small enough that the electrostatic charging energy required to place a charge of 2*e* on the island at zero voltage, $(2e)^2/2C_\Sigma$, is much greater than the thermal energy k_BT (where $C_\Sigma = C_g + C_j$ is the total capacitance). For $T = 1\,K$, this requires C_Σ to be much less than 1 fF. The Cooper-pair box is connected to ground by a gate capacitance C_g in series with a potential V_g and by a small Josephson junction with $E_j << E_c$. Given their weak connection to the 'outside world', the number of Cooper pairs on the island is a discrete variable *n*. The qubit states correspond to adjacent Cooper-pair number states $|n\rangle$ and $|n+1\rangle$.

To understand how to control a single Cooper pair, it is useful to first examine the electrostatic problem with an infinite junction resistance ($E_j = 0$). The total electrostatic energy of the circuit is $E_{ch} = (2e^2/C_g)(n - n_g)^2$, where $n_g = C_gV_g/2e$ (representing the gate voltage in terms of the gate charge, namely the polarization charge that the voltage induces on the gate capacitor). Although *n* is an integer, n_g is a continuous variable. E_{ch} versus n_g is shown in Fig. 3c for several values of *n*. It should be noted that the curves for *n* and $n+1$ cross at $n_g = n + \frac{1}{2}$, the charge degeneracy point. At this point, the gate polarization corresponds to half a Cooper pair for both charge basis states.

By restoring the Josephson coupling to a small value, the behaviour close to these crossing points is modified. The Josephson junction allows Cooper pairs to tunnel onto the island one by one. The resultant coupling between neighbouring charge states $|n\rangle$ and $|n+1\rangle$ makes the quantum superposition of charge eigenstates analogous to the superposition of flux states in equation (3) (identifying $|\downarrow\rangle = |n\rangle$ and $|\uparrow\rangle = |n+1\rangle$). The next excited charge state is higher in energy by E_c and can safely be neglected. At the charge degeneracy point, where the Josephson coupling produces an avoided crossing, the symmetrical and antisymmetrical superpositions are split by an energy E_j. By contrast, far from this point, $E_c >> E_j$, and the eigenstates are very close to being charge states. Again, the energy level structure is analogous to that of flux qubits, with Δ replaced with E_j and ε with $E_c \times (n_g - n - \frac{1}{2})$. Similarly, the probabilities of measuring the ground state or excited state depend on the gate voltage rather than the applied flux.

To make the qubit fully tunable, the Josephson junction is usually replaced by a d.c. SQUID with low inductance ($\beta_L << 1$). E_j is then adjusted by applying the appropriate magnetic flux, which is kept constant throughout the subsequent measurements.

The read-out of a charge qubit involves detecting the charge on the island to a much greater accuracy than 2*e*. This is accomplished by using a single-electron transistor (SET), a sensitive electrometer[16]. The SET (Fig. 3d), also based on a tiny island, is connected to two superconducting leads by two Josephson junctions. When the voltages across both junctions are close to the degeneracy point ($n_g = n + \frac{1}{2}$), charges cross the junctions to produce a net current flow through the SET. Thus, the current near the degeneracy points depends strongly on the gate voltage (Fig. 3c). Capacitively coupling the Cooper-pair-box island to the SET island makes a contribution to the SET gate voltage so that the SET current strongly depends on the Cooper-pair-box state. This scheme converts the measurement of charge into a measurement of charge transport through a SET. In fact, for small Josephson junctions, this charge transport is usually dissipative, because the phase coherence is destroyed by environmental fluctuations. Thus, the read-out actually involves measuring the resistance of the SET, which depends on the state of the Cooper-pair box. The preferred read-out device is a radio-frequency SET[17], in which a SET is embedded in a resonant circuit. Thus, the *Q* of the resonant circuit is determined by the resistance of the SET and ultimately by the charge on the Cooper-pair box. A pulse of microwaves slightly detuned from the resonant frequency is applied to the radio-frequency SET, and the phase of the reflected signal enables the state of the qubit to be determined.

Many of the initial studies of superconducting qubits involved charge qubits. That crossing is avoided at the degeneracy point was first shown spectroscopically by studying a charge qubit[9], and charge measurements revealed the continuous, quantum-rounded form of the transition between quantum states[18]. The coherent oscillations that occur with time at this avoided energy-level crossing were also first discovered by studying a charge qubit[19].

© 2008 Macmillan Publishers Limited. All rights reserved

Cooper-pair boxes are particularly sensitive to low-frequency noise from electrons moving among defects (see the section 'Decoherence') and can show sudden large jumps in n_g. The development of more advanced charge qubits such as the transmon[20] and quantronium[12] has greatly ameliorated this problem. The transmon is a small Cooper-pair box that is made relatively insensitive to charge by shunting the Josephson junction with a large external capacitor to increase E_c and by increasing the gate capacitor to the same size. Consequently, the energy bands of the type shown in Fig. 3c are almost flat, and the eigenstates are a combination of many Cooper-pair-box charge states. For reasons that will be discussed later (see the section 'Decoherence'), the transmon is thus insensitive to low-frequency charge noise at all operating points. At the same time, the large gate capacitor provides strong coupling to external microwaves even at the level of a single photon, greatly increasing the coupling for circuit quantum electrodynamics (QED) (see the section 'Quantum optics on a chip').

The principle by which quantronium operates is shown in Fig. 4a, and an actual circuit is shown in Fig. 4b. The Cooper-pair box involves two Josephson junctions, with a capacitance C_g connected to the island separating them. The two junctions are connected across a third, larger, junction, with a higher critical current, to form a closed superconducting circuit to which a magnetic flux Φ_e is applied. The key to eliminating the effects of low-frequency charge and flux noise is to maintain the qubit at the double degeneracy point at which the two qubit states are (to first order) insensitive to these noise sources. To achieve insensitivity to charge noise, the qubit is operated at $n_g = ½$, where the energy levels have zero slope and the energy-level splitting is E_j (Fig. 3c). Insensitivity to flux noise is achieved by applying an integer number of half-flux quanta to the loop. The success of this optimum working point has been elegantly shown experimentally[21]. The insensitivity to both flux and charge implies, however, that the two states of the qubit cannot be distinguished at the double degeneracy point. To measure the qubit state, a current pulse that moves the qubit away from the flux degeneracy point is applied to the loop, and this produces a clockwise or anticlockwise current in the loop, depending on the state of the qubit. The direction of the current is determined by the third (read-out) junction: the circulating current either adds to or subtracts from the applied current pulse, so the read-out junction switches out of the zero-voltage state at a slightly lower or slightly higher value of the bias current, respectively. Thus, the state of the qubit can be inferred by measuring the switching currents. With the advent of quantronium, much longer relaxation and decoherence times can be achieved than with a conventional Cooper-pair box.

Although this switching read-out scheme is efficient, it has two major drawbacks. First, the resultant high level of dissipation destroys the quantum state of the qubit, making sequential measurements of the state impossible. Second, the temperature of the read-out junction and substrate increase because of the energy that is deposited while the SQUID is in the voltage state — typically for 1 μs — and the equilibrium is not restored for ~1 ms. This limits the rate at which measurements can be made to ~1 kHz, resulting in long data-acquisition times.

These drawbacks have been overcome by the introduction of the Josephson bifurcation amplifier (JBA)[22], a particularly powerful read-out device in which there is no dissipation because the junction remains in the zero-voltage state (Fig. 4c). The JBA exploits the nonlinearity of the Josephson junction when a capacitor is connected across it, resulting in the formation of a resonant (or tank) circuit. When small-amplitude microwave pulses are applied to the resonant circuit, the amplitude and phase of the reflected signal are detected, with the signal strength boosted by a cryogenic amplifier. From this measurement, the resonant frequency of the tank circuit can be determined, then the inductance of the junction — which depends on the current flowing through it — and, finally, the state of the quantronium. For larger-amplitude microwaves, however, the behaviour of the circuit is strongly nonlinear, with the resonance frequency decreasing as the amplitude increases. In particular, strong driving at frequencies slightly below the plasma frequency leads to a bistability: a weak, off-resonance lower branch during which the particle does not explore the nonlinearity, and a high-amplitude response at which frequency matches the driving frequency (Fig. 4d). The two qubit states can be distinguished by choosing driving frequencies and currents that cause the JBA to switch to one response or the other, depending on the qubit state. This technique is extremely fast and, even though it is based on a switching process, it never drives the junction into the voltage state. Furthermore, the JBA remains in the same state after the measurement has been made.

The JBA has been shown to approach the quantum non-demolition (QND) limit[22]. This limit is reached when the perturbation of the quantum state during the measurement does not go beyond that required by the measurement postulate of quantum mechanics, so repeated measurements of the same eigenstate lead to the same outcome[23]. Reaching the QND limit is highly desirable for quantum computing.

A similar scheme that approaches the QND limit has been implemented for the flux qubit, with the single Josephson junction replaced by a read-out SQUID[24]. Dispersive read-out for a flux qubit has also been achieved by inductively coupling a flux qubit to the inductor of a resonant circuit and then measuring the flux state from the shift in the resonance frequency[25].

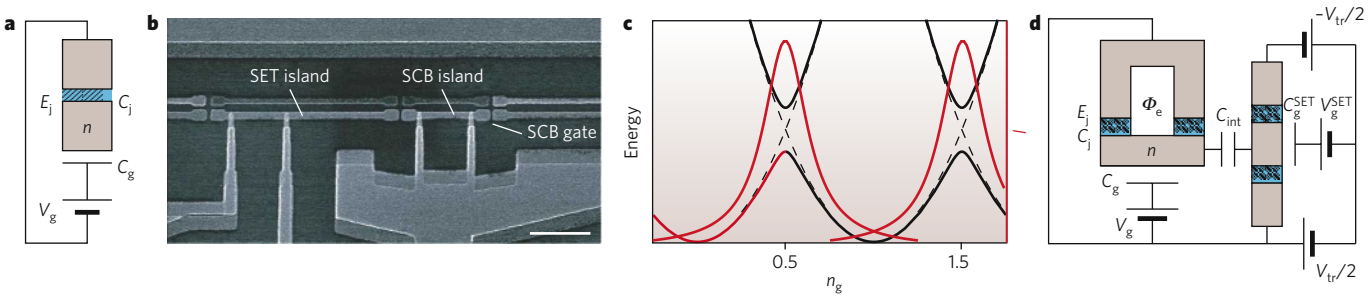

Figure 3 | Charge qubits. **a**, A single Cooper-pair-box (SCB) circuit is shown. The superconducting island is depicted in brown and the junction in blue. E_j and C_j are the Josephson coupling energy and self-capacitance, respectively, and n is the number of Cooper pairs on the island, which is coupled to a voltage source with voltage V_g by way of a capacitor with capacitance C_g. (Panel reproduced, with permission, from ref. 28.) **b**, A micrograph of a Cooper-pair box coupled to a single-electron transistor (SET) is shown. Scale bar, 1 μm. (Panel reproduced, with permission, from ref. 78.) **c**, Black curves show the energy of the Cooper-pair box as a function of the scaled gate voltage $n_g = C_g V_g/2e$ for different numbers (n) of excess Cooper pairs on the island. The parabola on the far left corresponds to $n = 0$ and the central parabola to $n = 1$. Dashed lines indicate the contribution of the charging energy $E_{ch}(n, n_g)$ alone. The energy-level splitting at $n_g = ½$ is E_j. Red curves show the current I through the SET as a function of n_g. Transport is possible at the charge degeneracy points, where the gate strongly modulates the current. (Panel reproduced, with permission, from ref. 28.) **d**, A charge qubit with two junctions (left) coupled to a SET biased to a transport voltage V_{tr} (right) is shown. The critical current of the junctions coupled to the island is adjusted by means of an externally applied magnetic flux Φ_e. The gate of the SET is coupled to an externally controlled charge induced on the capacitor with capacitance C_g^{SET} by the voltage V_g^{SET}, as well as to the qubit charge by way of the interaction capacitance C_{int}. (Panel reproduced, with permission, from ref. 28.)

© 2008 Macmillan Publishers Limited. All rights reserved

Phase qubits

In essence, a phase qubit[13] consists of a single current-biased Josephson junction (Box 1 figure). For a bias current I just below the critical current I_0, the anharmonic potential is approximately cubic, and the energy-level spacing becomes progressively smaller as the quantum number n increases. As I approaches I_0, the (classical) plasma oscillation frequency, $\omega_p(I) = 2^{1/4}(2\pi I_0/\Phi_0 C)^{1/2}(1 - I/I_0)^{1/4}$, decreases slowly, while the potential barrier height, $\Delta U(I) = (2\sqrt{2}\, I_0\Phi_0/3\pi)(1 - I/I_0)^{3/2}$, decreases rapidly. Thus, the probability of escape from the state $|n\rangle$ by macroscopic quantum tunnelling increases exponentially as n increases. The qubit involves transitions between the ground state $|0\rangle$ and the first excited state $|1\rangle$. To measure the quantum state of the qubit, a microwave pulse is applied with frequency $(E_2 - E_1)/h$. If, on the one hand, the qubit is in the state $|1\rangle$, then the pulse excites a transition to the state $|2\rangle$, from which macroscopic quantum tunnelling causes the junction to switch to the voltage state. If, on the other hand, the junction is initially in the state $|0\rangle$, then no such transition occurs. Operation of the phase qubit depends crucially on the anharmonicity of the well potential, which ensures that $E_2 - E_1 < E_1 - E_0$.

The first phase qubit that was designed involved a $10 \times 10\,\mu m^2$ Nb–Al_xO_y–Nb tunnel junction (where $x \leq 2$ and $y \leq 3$), which was created photolithographically. To measure the occupation probability p_1 of the state $|1\rangle$, Martinis *et al.*[13] applied a long microwave pulse of angular frequency $\omega_{10} = (E_1 - E_0)/\hbar$, followed by a read-out pulse of frequency $\omega_{21} = (E_2 - E_1)/\hbar$ (Fig. 5a). If the state $|1\rangle$ is occupied, the second pulse switches the junction to the voltage state, which is detected by a low-noise amplifier. If, conversely, the junction is in the state $|0\rangle$, the probability of switching is very small. As the power P_{10} in the first pulse is increased, the probability of $|1\rangle$ being occupied increases until it reaches a plateau at 0.5. The results of the measurement are shown in Fig. 5a, where p_1 is defined as the ratio of the number of trials in which switching to the voltage state occurs to the total number of trials. As expected, p_1 approaches 0.5 as P_{10} increases.

In early designs of phase qubits, the junction switched to the voltage state, resulting in energy dissipation. In a later, improved, design[26], the qubits remain in the zero-voltage state (Fig. 5b, c). The qubit junction is embedded in a superconducting loop that is inductively coupled to a SQUID and to a line through which static and pulsed currents can be passed. With appropriately chosen parameters, the potential energy of the qubit displays the two asymmetrical wells shown in Fig. 5c. The states $|0\rangle$ and $|1\rangle$ in the left well are the qubit states; their energy separation and the depth of the well can be controlled by varying the flux in the loop. To read out the state of the phase qubit, a short adiabatic pulse that reduces the depth ΔU of the qubit potential well is applied to the flux bias line. If the qubit is in the state $|1\rangle$, it tunnels rapidly into the right well; in the state $|0\rangle$, no tunnelling occurs. Depending on whether tunnelling occurs, the flux in the qubit loop differs by a single flux quantum, which can easily be detected subsequently by the read-out SQUID. This scheme enables the state of the qubit to be measured rapidly, typically in 5 ns, which is still adiabatic (slow) on the timescale of transitions between the qubit states. Subsequent measurement of the flux in these qubit loops can be made much more slowly.

Time-domain measurements

Spectroscopy is important for establishing that a given qubit is a functional device, and it enables energy-level splitting to be measured as a function of relevant control parameters. But measurements in the

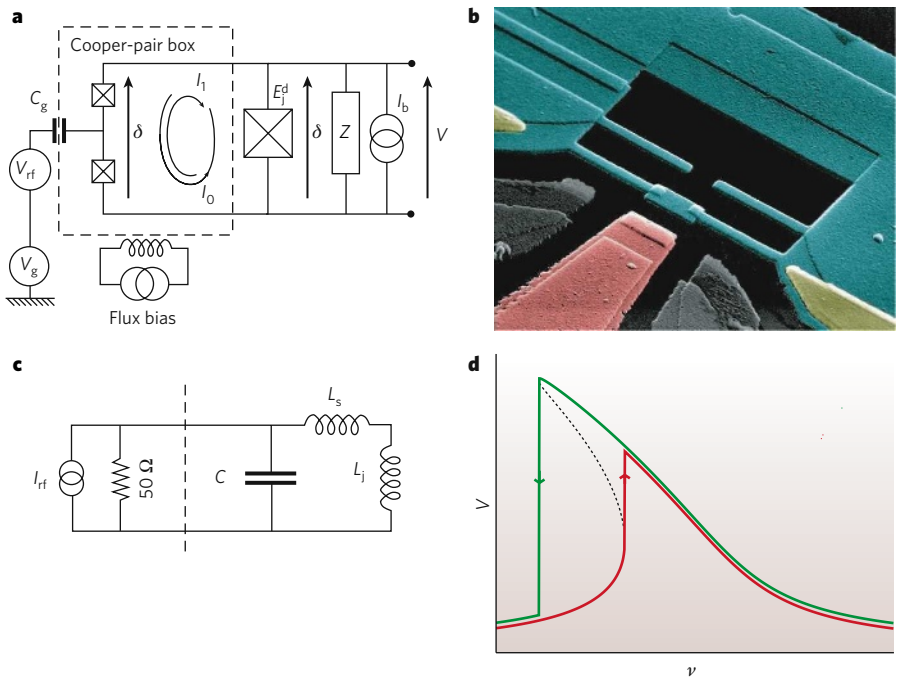

Figure 4 | Quantronium. a, A quantronium circuit is depicted. The Cooper-pair box is connected by way of two Josephson junctions to the detector Josephson junction, which has Josephson energy E_j^d (right), and by way of a capacitor (with gate capacitance C_g) to the static voltage bias V_g and the radio-frequency gate voltage V_{rf} that prepares the state of the Cooper-pair box. The dashed lines enclose the qubit. I_b is the bias current of the detector junction, and Z is an engineered environmental impedance. The flux through the loop formed by the three Josephson junctions is controlled by an external bias circuit. The read-out is the phase δ across the two box junctions, measured by combining the bias current I_b with the circulating loop currents I_0 or I_1. (Panel reproduced, with permission, from ref. 12.) **b**, A micrograph of quantronium is shown. The Cooper-pair box and leads are depicted in blue, and the gate electrode in red. (In gold are normal metal films that are used to remove quasiparticles from the superconducting films.) (Image courtesy of D. Esteve, Commissariat à l'Énergie Atomique, Saclay, France.) **c**, A Josephson bifurcation amplifier (JBA) is depicted. In a JBA, a Josephson junction, represented by the nonlinear inductance L_j, is shunted with a capacitance C via a stray inductance L_S; I_{rf} is the radio-frequency current bias. The dashed line separates the off-chip circuitry (left) from the on-chip circuitry (right). (Panel reproduced, with permission, from ref. 22.) **d**, The response curve (voltage V versus frequency ν) of the JBA driven at high radio-frequency current amplitude at a frequency slightly below resonance is shown, and the hysteresis that results from dynamical bifurcation is indicated (arrows). The red line shows the low-amplitude response of the JBA, and the green line shows the high-amplitude response; the dashed line indicates metastable states.

© 2008 Macmillan Publishers Limited. All rights reserved

time domain are also necessary to determine the dynamical behaviour of a qubit. These measurements involve manipulating the state of the qubit by using appropriate microwave pulses — which are also required to implement single-qubit gates for quantum computing. In broad terms, qubits are characterized by two times, named T_1 and T_2 by analogy with nuclear magnetic resonance (NMR) spectroscopy[27]. The relaxation time T_1 is the time required for a qubit to relax from the first excited state to the ground state; this process involves energy loss. The dephasing time T_2 is the time over which the phase difference between two eigenstates becomes randomized. Theoretically, both relaxation and dephasing are described by weak coupling to the quantum noise produced by the environment[27–29]. This approach predicts that energy relaxation arises from fluctuations at the energy-level splitting frequency of the two states in question. The dephasing rate, by contrast, has two contributions:

$$1/T_2 = 1/(2T_1) + 1/\tau_\phi \quad (5)$$

The first contribution arises from the relaxation process, and the second, 'pure dephasing', arises from low-frequency fluctuations with exchange of infinitesimal energy. (The pure dephasing time is τ_ϕ.)

The simplest way to measure relaxation is to irradiate the qubit with microwaves at the frequency corresponding to the energy-level splitting between the ground and first excited states for a time much greater than T_1. After the pulse has been turned off, the qubit has an equal probability of being in either state; the probability p_1 of its being in the excited state $|1\rangle$ subsequently decays with time t as $\exp(-t/T_1)$. Measurements of p_1 as a function of t yield the value of T_1. It should be emphasized that each measurement of p_1 at a given time delay involves a large number of measurements, typically 10^4 or 10^5. T_1 can vary from values of the order of 1 ns to many microseconds.

To understand the various pulse measurements, it is useful to consider the Bloch sphere (Fig. 6a), which enables any arbitrary quantum superposition of the quantum states $|0\rangle$ and $|1\rangle$ to be considered as a vector. The states $|0\rangle$ and $|1\rangle$ point along the positive and negative z axis, respectively. The superpositions $|0\rangle \pm |1\rangle$ lie along the $\pm x$ axes, and the superpositions $|0\rangle \pm i|1\rangle$ along the $\pm y$ axes. Thus, a given point on the surface of the sphere defines a specific superposition of these states.

The Bloch sphere can be used to describe Rabi oscillations in a flux qubit. Microwaves are applied at the energy-level splitting frequency for the qubit for a time τ with the magnetic-field component along the y axis. During the pulse, the state vector rotates in the y–z plane about the x axis with the Rabi frequency ν_R, which is proportional to the microwave amplitude. After time τ, the state vector is at an angle $2\pi\nu_R\tau$ to the z axis. Subsequent measurements of the probability of the qubit being in the state $|0\rangle$ or $|1\rangle$ yield Rabi oscillations as a function of τ. An example is shown in Fig. 6b. Rabi oscillations are a convenient means of calibrating the amplitude of the magnetic-field component of the microwave field that is coupled to the qubit.

In measuring the dephasing time, it is crucial to distinguish T_2 (equation (5)) — an intrinsic timescale for the decoherence of a single qubit — from $T_2^\star$, the result of an ensemble measurement. The ensemble is formed because experiments on a single qubit need to be carried out repeatedly so that sufficiently precise data are acquired. Even though the different measurements are nominally identical, slow fluctuations on the timescale of a single run result in a change in the operating conditions between runs. This reduces the observed coherence time to $T_2^\star$ (which is $< T_2$).

$T_2^\star$ and T_2 can be measured separately: $T_2^\star$, which includes the effects of low-frequency noise, by using Ramsey fringes[30]; and T_2, by using a spin-echo technique[27], which eliminates certain low-frequency contributions. To observe Ramsey fringes, a $\pi/2$ microwave pulse is first applied at a frequency f_m — with amplitude calibrated from the Rabi oscillations — that tips the qubit state vector into the equatorial (x–y) plane. The vector precesses freely on the Bloch sphere around the static magnetic field B_0, with a magnitude that decreases with time, owing to dephasing. After a variable time delay τ_d, a second $\pi/2$ microwave pulse brings the state vector to a point on the Bloch sphere that depends on both f_m and τ_d. The subsequent measurement of the qubit state projects the vector onto either $|0\rangle$ or $|1\rangle$. Thus, a plot of the switching probability versus τ_d for a given microwave frequency maps out the free evolution of the qubit. For a resonant pulse ($f_m = \nu_{10}$), the free evolution and the microwave pulses are synchronized, and the measurement reveals a coherence amplitude that decays exponentially with characteristic time $T_2^\star$. To map out $T_2^\star$ over a larger parameter space, the $\pi/2$ microwave pulses are detuned from ν_{10}. Thus, the pulse and evolution are no longer synchronized, and oscillations — Ramsey fringes — are observed at a frequency $\nu_{Ramsey} = |f_m - \nu_{10}|$ (Fig. 6c).

To remove the slow fluctuations that differentiate $T_2^\star$ from T_2, a spin-echo technique, analogous to that used in NMR, can be used. In this technique, a π pulse is applied at the midpoint in time between the two $\pi/2$ pulses. The π pulse flips the qubit state vector to the opposite side of the equatorial plane; therefore, a fluctuation that initially caused the phase to advance now causes it to lag, and vice versa. Thus, at the time of the second $\pi/2$ pulse, the effects of fluctuations that occur on timescales longer than the overall measurement time are (ideally) completely cancelled out. An example is shown in Fig. 6d.

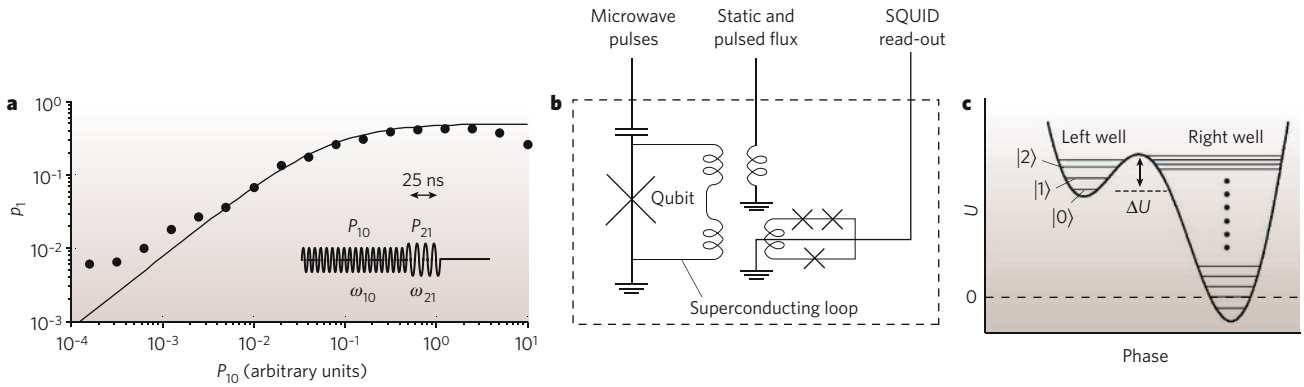

Figure 5 | Phase qubits. a, The filled circles represent the probability p_1 that the phase qubit occupies the first excited state versus microwave power P_{10} at angular frequency ω_{10}. The solid line is the theoretical prediction. The inset shows the pulse sequence; the microwaves at angular frequency ω_{10} equalize the probability that the ground and excited states are occupied, and the microwaves at angular frequency ω_{21} cause the qubit to switch to the voltage state if the first excited state is occupied. (Panel reproduced, with permission, from ref. 13.) **b**, For zero-voltage operation, the Josephson junction of a phase qubit is shunted by a superconducting loop, coupled to a read-out SQUID, that allows static and pulsed fluxes to be applied. The dashed line indicates the components fabricated on the silicon chip, which is maintained at 25 mK. (Panel reproduced, with permission, from ref. 26.) **c**, The asymmetrical double-well potential of a phase qubit is shown. The qubit states are $|0\rangle$ and $|1\rangle$. The state $|2\rangle$ becomes occupied on the application of microwaves at frequency ω_{21} provided that the state $|1\rangle$ is occupied. The state $|3\rangle$, above $|2\rangle$, has no role in the read-out process. Dots in the right well indicate the intervening energy levels. (Panel reproduced, with permission, from ref. 26.)

© 2008 Macmillan Publishers Limited. All rights reserved

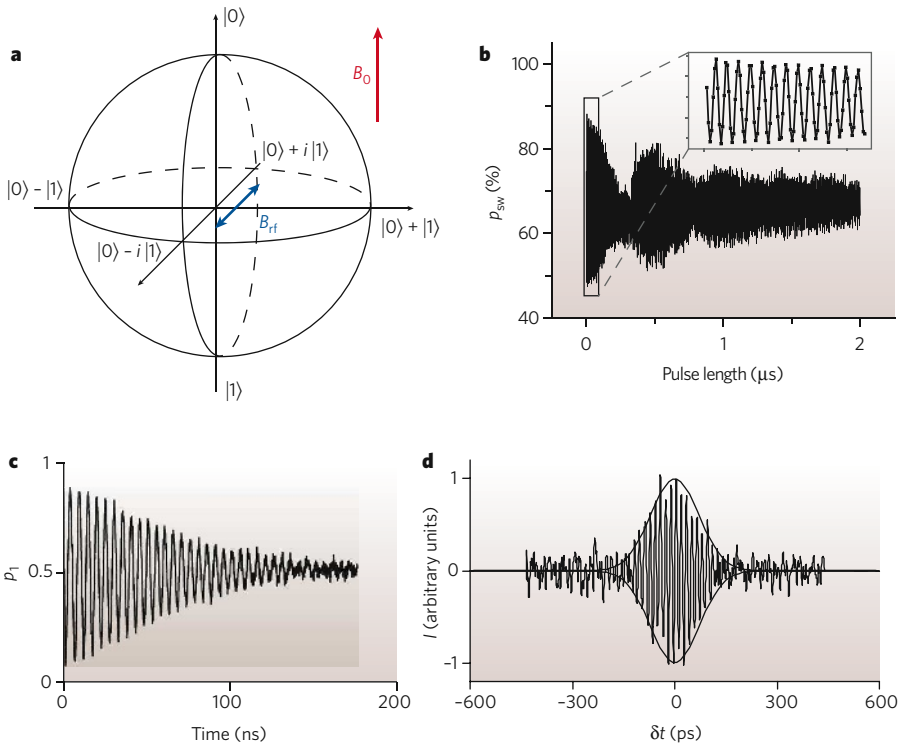

Figure 6 | Qubit manipulation in the time domain. **a**, The Bloch sphere is depicted, with an applied static magnetic field B_0 and a radio-frequency magnetic field B_{rf}. Any given superposition of the six states shown is represented by a unique point on the surface of the sphere. **b**, Rabi oscillations in a flux qubit are shown. The probability p_{sw} that the detector (SQUID) switches to the normal state versus pulse length is shown, and the inset is a magnification of the boxed region, showing that the dense traces are sinusoidal oscillations. As expected, the excited-state population oscillates under resonant driving. (Panel reproduced, with permission, from ref. 40.) **c**, Ramsey fringes in a phase qubit are shown. Coherent oscillations of the switching probability p_1 between two detuned $\pi/2$ pulses is shown as a function of pulse separation. (Panel reproduced, with permission, from ref. 31.) **d**, The charge echo in a Cooper-pair box is shown as a function of the time difference $\delta t = t_1 - t_2$, where t_1 is the time between the initial $\pi/2$ pulse and the π pulse, and t_2 is the time between the π pulse and the second $\pi/2$ pulse. The echo peaks at $\delta t = 0$. (Panel reproduced, with permission, from ref. 39.)

Measuring the times T_1, T_2 and T_2^* provides an important initial characterization of qubit coherence. However, other factors such as pulse inaccuracy, relaxation during measurement and more complex decoherence effects result in measurement errors. A more complete measure of a qubit is fidelity, a single number that represents the difference between the ideal and the actual outcome of the experiment. Determining the fidelity involves quantum-process tomography (a repeated set of state tomographies), which characterizes a quantum-mechanical process for all possible initial states. In a Ramsey-fringe tomography experiment, Matthias Steffen *et al.*[31] found a fidelity of ~80%, where 10% of the loss was attributed to read-out errors and another 10% to pulse-timing uncertainty.

Decoherence

Superconducting qubits are macroscopic, so — along the lines of Schrödinger's cat — they could be expected to be very sensitive to decoherence. In fact, given the unique properties of the superconducting state, careful engineering has led to remarkable increases in decoherence times compared with those of early devices.

Ideally, each type of qubit is described by a single degree of freedom. The central challenge is to eliminate all other degrees of freedom. In broad terms, there are two classes of decohering element: extrinsic and intrinsic. Obvious extrinsic sources include electromagnetic signals from radio and television transmitters; these can generally be eliminated by using careful shielding and enough broadband filters. A more challenging extrinsic source to exclude is the local electromagnetic environment: for example, contributions from the leads that are coupled to read-out devices or are used to apply flux or charge biases. These leads allow great flexibility in control of the system at the expense of considerable coupling to the environment. This issue was recognized in the first proposals of macroscopic quantum coherence and largely motivated the Caldeira–Leggett theory of quantum dissipation[6]. This theory maps any linear dissipation onto a bath of harmonic oscillators. The effects of these oscillators can be calculated from the Johnson–Nyquist noise that is generated by the complex impedance of the environment. In the weak-damping regime, both T_1 and τ_ϕ can be computed directly from the power spectrum of this noise, and then the impedance can be engineered to minimize decoherence[28,29]. The experimental difficulty is to ensure that the complex impedances 'seen' by the qubit are high over a broad bandwidth, for example, 0–10 GHz. It is particularly difficult to avoid resonances over such a broad range of frequencies. Clever engineering has greatly reduced this source of decoherence, but it would be optimistic to consider that this problem has been completely solved.

The main intrinsic limitation on the coherence of superconducting qubits results from low-frequency noise, notably '$1/f$ noise' (in which the spectral density of the noise at low frequency f scales as $1/f^\alpha$, where α is of the order of unity). In the solid state, many $1/f$ noise sources are well described by the Dutta–Horn model as arising from a uniform distribution of two-state defects[32]. Each defect produces random telegraph noise, and a superposition of such uncorrelated processes leads to a $1/f$ power spectrum. There are three recognized sources of $1/f$ noise. The first is critical-current fluctuations, which arise from fluctuations in the transparency of the junction caused by the trapping and untrapping of electrons in the tunnel barrier[33]. All superconducting qubits are subject to dephasing by this mechanism. The slow fluctuations modulate energy-level splitting, even at the degeneracy point, so each measurement is made on a qubit with a slightly different frequency. The resultant phase errors lead to decoherence.

The second source of $1/f$ noise is charge fluctuations, which arise from the hopping of electrons between traps on the surface of the superconducting film or the surface of the substrate. This motion induces charges onto the surface of nearby superconductors. This decoherence mechanism is particularly problematic for charge qubits, except at the degeneracy point, where the qubits are (to first order) insensitive. If the value of E_c/E_j increases, however, the energy bands (Fig. 3c) become flatter, and the qubit is correspondingly less sensitive to charge noise away from the degeneracy point. This mechanism underlies the substantially increased values of T_2 in the transmon[20].

The third source of $1/f$ noise is magnetic-flux fluctuations. Although such fluctuations were first characterized more than 20 years ago[34], the mechanism by which these occur remained obscure until recently. It is now thought that flux noise arises from the fluctuations of unpaired electron spins on the surface of the superconductor or substrate[35,36], but the details of the mechanism remain controversial. Flux noise causes decoherence in flux qubits, except at the degeneracy point, as well as in phase qubits, which have no degeneracy point. The increased value of T_2 in quantronium results from its insensitivity to both flux noise and charge noise at the double degeneracy point.

© 2008 Macmillan Publishers Limited. All rights reserved

Table 1 | Highest reported values of T_1, T_2^* and T_2

Qubit	T_1 (μs)	T_2^* (μs)	T_2 (μs)	Source
Flux	4.6	1.2	9.6	Y. Nakamura, personal communication
Charge	2.0	2.0	2.0	ref. 77
Phase	0.5	0.3	0.5	J. Martinis, personal communication

In general, all three low-frequency processes lead to decoherence. They do not contribute to relaxation because this process requires an exchange of energy with the environment at the energy-level splitting frequency of the qubit, which is typically in the gigahertz range. However, there is strong evidence that charge fluctuations are associated with the high-frequency resonators that have been observed, in particular, in phase qubits[37]. Improvements in the quality of the oxide layers that are used in the junctions and capacitors have resulted in large reductions in the concentration of these high-frequency resonators[38].

The strategy of operating a qubit at the optimum point, which was first carried out with quantronium but is now applied to all types of superconducting qubit (except for phase qubits), has been successful at increasing phase-coherence times by large factors. Further substantial improvements have resulted from the use of charge- or flux-echo techniques[39,40]. In NMR, the spin-echo technique removes the inhomogeneous broadening that is associated with, for example, variations in magnetic field, and hence in the NMR frequency, over the sample. In the case of qubits, the variation is in the qubit energy-level splitting frequency from measurement to measurement. For some qubits, using a combination of echo techniques and optimum point operation has eliminated pure dephasing, so decoherence is limited by energy relaxation ($T_2^* = 2T_1$). In general, however, the mechanisms that limit T_1 are unknown, although resonators that are associated with defects may be responsible[36,41]. The highest reported values of T_1, T_2^* and T_2 are listed in Table 1.

Coupled qubits

An exceedingly attractive and unique feature of solid-state qubits in general and superconducting qubits in particular is that schemes can be implemented that both couple them strongly to each other and turn off their interaction *in situ* by purely electronic means. Because the coupling of qubits is central to the architecture of quantum computers, this subject has attracted much attention, in terms of both theory and experiment. In this section, we illustrate the principles of coupled qubits in terms of flux qubits and refer to analogous schemes for other superconducting qubits.

Because the flux qubit is a magnetic dipole, two neighbouring flux qubits are coupled by magnetic dipole–dipole interactions. The coupling strength can be increased by having the two qubits use a common line. Even stronger coupling can be achieved by including a Josephson junction in this line to increase the line's self-inductance (equation (6), Box 1). In the case of charge and phase qubits, nearest-neighbour interactions are mediated by capacitors rather than inductors. Fixed interaction has been implemented for flux, charge and phase qubits[42–45]. These experiments show the energy levels that are expected for the superposition of two pseudospin states: namely, a ground state and three excited states; the first and second excited states may be degenerate. The entanglement of these states for two phase qubits has been shown explicitly by means of quantum-state tomography[46]. The most general description (including all imperfections) of the qubit state based on the four basis states of the coupled qubits is a four-by-four array known as a density matrix. Steffen *et al.*[46] carried out a measurement of the density matrix; they prepared a system in a particular entangled state and showed that only the correct four matrix elements were non-zero — and that their magnitude was in good agreement with theory. This experiment is a proof-of-principle demonstration of a basic function required for a quantum computer. Simple quantum gates have also been demonstrated[47,48].

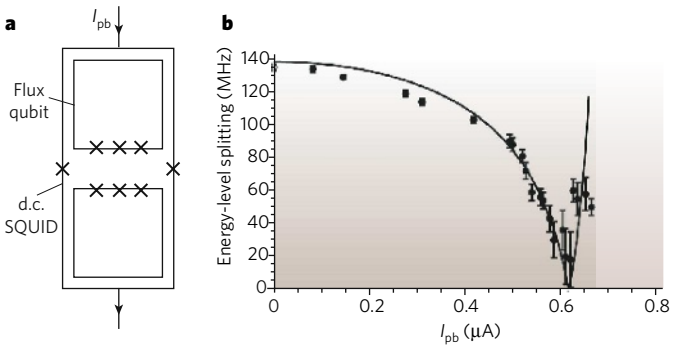

Figure 7 | Controllably coupled flux qubits. a, Two flux qubits are shown surrounded by a d.c. SQUID. The qubit coupling strength is controlled by the pulsed bias current I_{pb} that is applied to the d.c. SQUID before measuring the energy-level splitting between the states $|1\rangle$ and $|2\rangle$. **b**, The filled circles show the measured energy-level splitting of the two coupled flux qubits plotted against I_{pb}. The solid line is the theoretical prediction, fitted for I_{pb}; there are no fitted parameters for the energy-level splitting. Error bars, ±1σ. (Panels reproduced, with permission, from ref. 50.)

Two flux qubits can be coupled by flux transformers — in essence a closed loop of superconductor surrounding the qubits — enabling their interaction to be mediated over longer distances. Because the superconducting loop conserves magnetic flux, a change in the state of one qubit induces a circulating current in the loop and hence a flux in the other qubit. Flux transformers that contain Josephson junctions enable the interaction of qubits to be turned on and off *in situ*. One such device consists of a d.c. SQUID surrounding two flux qubits[49] (Fig. 7a). The inductance between the two qubits has two components: that of the direct coupling between the qubits, and that of the coupling through the SQUID. For certain values of applied bias current (below the critical current) and flux, the self-inductance of the SQUID becomes negative, so the sign of its coupling to the two qubits opposes that of the direct coupling. By choosing parameters appropriately, the inductance of the coupled qubits can be designed to be zero or even have its sign reversed. This scheme has been implemented by establishing the values of SQUID flux and bias current and then using microwave manipulation and measuring the energy-level splitting of the first and second excited states[50] (Fig. 7b). A related design — tunable flux–flux coupling mediated by an off-resonant qubit — has been demonstrated[51], and tunable capacitors have been proposed for charge qubits[52].

Another approach to variable coupling is to fix the coupling strength geometrically and tune it by frequency selection. As an example, we consider two magnetically coupled flux qubits biased at their degeneracy points. If each qubit is in a superposition of eigenstates, then its magnetic flux oscillates and the coupling averages to zero — unless both qubits oscillate at the same frequency, in which case the qubits are coupled. This phenomenon is analogous to the case of two pendulums coupled by a weak spring. Even if the coupling is extremely weak, the pendulums will be coupled if they oscillate in antiphase at exactly the same frequency.

Implementing this scheme is particularly straightforward for two phase qubits because their frequencies can readily be brought in and out of resonance by adjusting the bias currents[37]. For other types of qubit, the frequency at the degeneracy point is set by the as-fabricated parameters, so it is inevitable that there will be variability between qubits. As a result, if the frequency difference is larger than the coupling strength, the qubit–qubit interaction cancels out at the degeneracy point. Several pulse sequences have been proposed to overcome this limitation[53–55], none of which has been convincingly demonstrated as yet. The two-qubit gate demonstrations were all carried out away from the optimum point, where the frequencies can readily be matched.

On the basis of these coupling schemes, several architectures have been proposed for scaling up from two qubits to a quantum computer. The central idea of most proposals is to couple all qubits to a long central coupling element, a 'quantum bus'[56,57] (Fig. 8), and to use frequency selection to determine which qubits can be coupled[56–60]. This scheme has been experimentally demonstrated. As couplers become longer, they become transmission lines that have electromagnetic modes. For example, two

© 2008 Macmillan Publishers Limited. All rights reserved

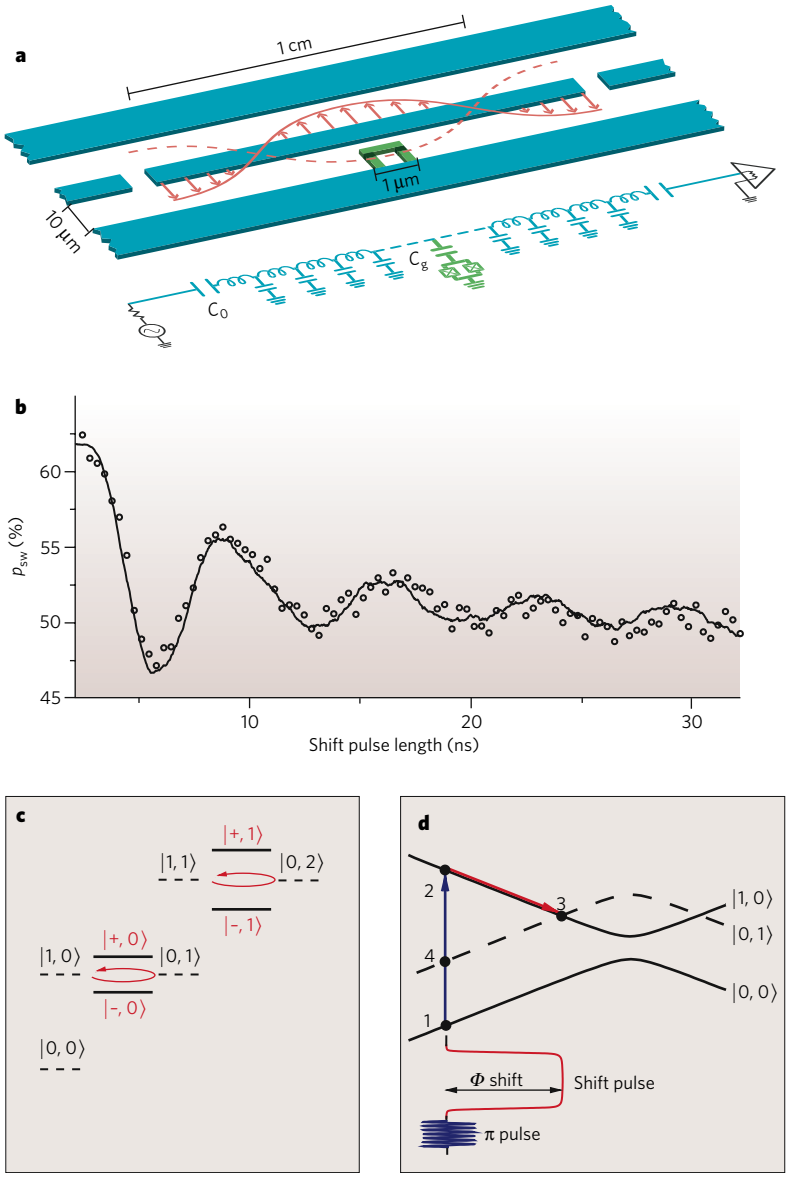

Figure 8 | Circuit QED. a, The upper part of the panel depicts a microstrip cavity (blue) that contains a charge qubit (green) placed at an antinode of the electric field. The microstripline can be used as a quantum bus. The lower part depicts this circuit in a lumped circuit representation. (Panel reproduced, with permission, from ref. 59.) C_0 is the capacitance of the coupling capacitor to the measurement electronics, and C_g is the capacitance of the coupling capacitor to the charge qubit. **b**, The open circles show the measured vacuum Rabi oscillations of a flux qubit coupled to a lumped resonator. The solid curve is a fit to the data. (Panel reproduced, with permission, from ref. 68.) **c**, An energy ladder of qubit ground and excited states combined with photon number n, $|0, n\rangle$ and $|1, n\rangle$ (dashed lines), is shown. With the cavity in resonance with the qubits, the states with zero photons split into linear combinations $|\pm, 0\rangle$ (solid lines), with an energy-level splitting g, and the states with one photon split into linear combinations $|\pm, 1\rangle$, with an energy-level splitting $\sqrt{2}g$. The red arrows indicate that if the system is initially in one of the states represented by dashed lines, it will perform Rabi oscillations between the qubit and the cavity. (Panel modified, with permission, from ref. 68.) **d**, An energy-band diagram (solid and dashed black lines) is shown as a function of applied flux for the measurement scheme that led to the results in **b**. The measurement pulse (π pulse) forces the system from the ground state (point 1) into a state with an excited qubit (point 2) (depicted in blue), which then puts the qubit and the cavity into resonance at point 3 (depicted in red). After the vacuum Rabi oscillation occurs, the system returns to point 2 or makes a coherent transition to point 4, where the qubit excitation is converted to a cavity photon. (Panel modified, with permission, from ref. 68.)

qubits have been coupled by placing them at the antinodes of a standing wave on a stripline[59–62]. Coupling between specific pairs of qubits can result in a scalable architecture[63]. By first coupling a qubit to the standing-wave mode using frequency selection, a photon is excited and then stored after decoupling. Subsequently, a second qubit is coupled to the mode, and the photon transfers the quantum state to the second qubit.

Architectures for adiabatic quantum computers are the subject of intense research. Adiabatic quantum computing encodes the solution to a hard problem in the ground state of a qubit system and uses quantum physics to prepare that ground state efficiently. The ground state of a four-qubit system with tunable interactions has been mapped out[64]. It should, however, be noted that there is no proof that an adiabatic quantum computer will be faster than a classical computer.

Quantum optics on a chip

An important new direction in superconducting qubit research is based on analogy between superconducting circuits and the fields of atomic physics and quantum optics. So far, we have described only qubits as quantum objects, and the control fields and read-out signals have been treated as classical variables. Circuit QED, by contrast, addresses the quantum behaviour of the electromagnetic field, such as that of single photons. In previous sections, the discussion refers to a quantum field in a coherent state in the limit of large numbers of photons.

The key requirement for reaching the quantum limit of the electromagnetic field is that the zero-point fluctuation of a single mode — measured by the root mean square of the electric field, $E_{rms} = \sqrt{\langle E^2 \rangle_{vacuum}}$ — be strong enough to have an appreciable coupling strength $g = dE_{rms}$ to the qubit electric dipole moment d. This requirement is met by increasing the amplitude of the field by creating a standing wave in a resonator and placing the qubit at one of the antinodes[59] (Fig. 8a). The resonator can be either a microstripline — an on-chip wave guide for microwaves — or a lumped circuit. In the first experiment[65], the resonator was tunable. The physics is closely related to cavity QED[66], in which atoms couple to an optical field confined between two mirrors. A key difference is that in circuit QED, the 'atom' (that is, the superconducting qubit) does not move inside the cavity, so the 'atom'–field interaction has time to act without losing the 'atom'. Together with the fact that $g/\hbar$ is larger than the rate of photon loss from the cavity, this difference allows the strong coupling limit of QED to be achieved in a relatively straightforward manner. The underlying reasons are that g is proportional to d (which, for a Cooper-pair box, is large, about 10^4 atomic units) and that E_{rms} is also large because of the increase in the electromagnetic field in the one-dimensional stripline.

Circuit QED can be operated in two distinct strong-coupling limits: the resonant regime, and the off-resonant dispersive regime. In the resonant regime, the qubit energy-level splitting is in resonance with the cavity

© 2008 Macmillan Publishers Limited. All rights reserved

frequency. In this regime, the combined states of the qubit and cavity can be written in the form |qubit state, photon number⟩. On resonance, the qubit and cavity can exchange excitations without losing energy: that is, the energy of $|1, n\rangle$ is equal to the energy of $|0, n+1\rangle$. The eigenstates of the system are thus superpositions of the form $|\pm, n\rangle = |1, n\rangle \pm |0, n+1\rangle$, with energies split by $g\sqrt{n}$, leading to the energy spectrum shown in Fig. 8c. This has a striking consequence: suppose that initially the qubit energy is not in resonance with the cavity (so the two are decoupled) and that the qubit is put into an excited state while the cavity is left in its vacuum state. When the qubit and the cavity in that state are suddenly coupled by using the procedure shown in Fig. 8d, the original state ceases to be an eigenstate and, instead, becomes an equal superposition of $|+, 0\rangle$ and $|-, 0\rangle$. After a time t, these acquire a relative phase of $gt/\hbar$ and manifest themselves as a coherent oscillation between $|1, 0\rangle$ and $|0, 1\rangle$, even though initially there was no photon in the cavity. These vacuum Rabi oscillations have been shown spectroscopically[67] and in the time domain[68] (Fig. 8b).

The second case is the off-resonant dispersive regime. In this case, the qubit and cavity eigenstates are not entangled, and the two systems cannot share excitations. The mutual energies, however, are still correlated, because the energy-level splitting of the qubit depends on the cavity state, and vice versa. Consequently, the cavity can be used to read out the qubit and to couple qubits to each other[59].

Circuit QED has been highly successful. So far, experimental progress has included attaining the strong coupling limit[67], mapping out the discrete nature of the quantized field[69], generating single photons[70] and coupling qubits using a bus[61,62]. These developments are leading to flexible quantum optics on a chip and open the door to a new domain of mesoscopic physics. Scalable architectures for quantum computers based on circuit QED have been proposed[62].

These ideas have led to the recent demonstration of a superconducting qubit laser. The 'atom' — a charge qubit — is weakly coupled to a second lead. In appropriate bias conditions, a cyclic process takes place: Cooper pairs that enter the box are broken into two quasiparticles, which exit through the second lead. This cycle results in a significant overpopulation of the first excited qubit state compared with the ground state — that is, a population inversion — and the generation of a laser action[71].

Studies in atomic physics have produced superb techniques for actively cooling atoms. Because superconducting qubits operate at millikelvin temperatures, it might be thought that further cooling is unnecessary. But both the preparation of a high-fidelity initial state and the supply of qubits initialized to the ground state for error correction can be facilitated by active cooling. Cooling to 3 mK from an initial temperature of 400 mK has been achieved by exciting the population of the excited state of a flux qubit to a higher excited state that is delocalized in a double-well potential, and then allowing the qubit to relax to the ground state[72]. 'Sisyphus cooling' has also been demonstrated[73]: in this cooling protocol, the energy that is supplied to the qubit from the heat bath is cyclically removed by the magnetic component of a suitably tailored microwave field.

Outlook

Quantum computing is a huge driving force for technological innovation. Since macroscopic quantum coherence was shown, the progress in the design and operation of superconducting qubits has been remarkable. There is now a rich variety of devices that contain the three qubit types, either separately or in combination. Decoherence times have been increased from ~1 ns to ~10 μs, and single-shot and QND read-outs are close to being achieved. So, what challenges and prospects now lie ahead?

On a fundamental level, the next benchmark is to verify a violation of Bell's inequality[74]. This inequality, which involves the outcomes of a combination of two-qubit measurements, is obeyed for any local theory but is violated for truly non-local physics such as quantum mechanics. A variation is the Leggett–Garg inequality[75], which relates to temporal correlations rather than to two-qubit correlations. One important aspect of quantum mechanics — entanglement — has been shown for superconducting qubits[46], but the testing of whether Bell's inequality is violated poses formidable technological challenges, particularly with respect to the fidelity of the measurement and the elimination of cross-talk. To make a Bell test convincing, the interaction between qubits needs to be switched off very accurately so that measurements are truly independent. An even more convincing test would involve a true space-like separation: that is, measuring the read-out of two qubits in such a short time that no signal has been able to travel between them at the speed of light. Given the confines of a dilution refrigerator, however, it seems that it will not be possible to test superconducting qubits in this way.

Another important experiment involving entanglement will be to investigate whether teleportation of a state occurs[76]: that is, the transfer of a quantum state inside an entangled pair of states.

On the path to quantum computing, superconducting qubits are clearly among the most promising candidates. Nevertheless, the path is long, and there are quantitative technological obstacles to be overcome, notably increasing the decoherence time and improving the fidelity of the read-out. The key benchmark will be to demonstrate simple error correction. To achieve these grand goals will require technological progress, not the least in the elimination — or at least the reduction — of low-frequency noise. Two-qubit coherence — in particular, the question of whether noise processes are correlated between qubits — is largely unexplored.

Will there ever be a superconducting quantum computer? This question cannot be answered today. The error thresholds discussed in fault-tolerance research — 1 error in 10,000 operations being a typical, but by no means universal, benchmark — are daunting. However, fault-tolerance research is an evolving field, and the computational protocols that have been discussed so far (which minimize the number of physical qubits and interactions required for a given algorithm) might not be best suited for superconducting qubits. Promising alternatives might be error-correction models with more generous thresholds, topological computing or other alternative computational models. Adiabatic quantum computing could also be an alternative if it is proved to be faster than classical computing. While addressing these issues, researchers are also likely to gain further insight into many physical properties and processes. ■

1. Bardeen, J., Cooper, L. N. & Schrieffer, J. R. Theory of superconductivity. *Phys. Rev.* **108,** 1175–1204 (1957).
2. Tinkham, M. *Introduction to Superconductivity* (McGraw-Hill, New York, 1996).
3. Devoret, M. H. in *Quantum Fluctuations: Les Houches Session LXIII* (eds Reynaud, S., Giacobino, E. & David, F.) 351–386 (Elsevier, Amsterdam, 1997).
4. Voss, R. F. & Webb, R. A. Macroscopic quantum tunneling in 1-μm Nb Josephson junctions. *Phys. Rev. Lett.* **47,** 265–268 (1981).
5. Devoret, M. H., Martinis, J. M. & Clarke, J. Measurements of macroscopic quantum tunneling out of the zero-voltage state of a current-biased Josephson junction. *Phys. Rev. Lett.* **55,** 1908–1911 (1985).
6. Caldeira, A. O. & Leggett, A. J. Quantum tunneling in a dissipative system. *Ann. Phys. (NY)* **149,** 374–456 (1983).
7. Martinis, J. M., Devoret, M. H. & Clarke, J. Energy-level quantization in the zero-voltage state of a current-biased Josephson junction. *Phys. Rev. Lett.* **55,** 1543–1546 (1985).
8. Leggett, A. J. in *Chance and Matter: Les Houches Session XLVI* (eds Souletie, J., Vannimenus, J. & Stora, R.) 395–506 (Elsevier, Amsterdam, 1987).
9. Nakamura, Y., Chen, C. D. & Tsai, J. S. Spectroscopy of energy-level splitting between two macroscopic quantum states of charge coherently superposed by Josephson coupling. *Phys. Rev. Lett.* **79,** 2328–2331 (1997).
10. Friedman, J. R., Patel, V., Chen, W.,Tolpygo, S. K. & Lukens, J. E. Quantum superpositions of distinct macroscopic states. *Nature* **406,** 43–46 (2000).
11. van der Wal, C. H. *et al.* Quantum superpositions of macroscopic persistent current. *Science* **290,** 773–776 (2000).
12. Vion, D. *et al.* Manipulating the quantum state of an electrical circuit. *Science* **296,** 886–889 (2002).
13. Martinis, J. M., Nam, S., Aumentado, J. & Urbina, C. Rabi oscillations in a large Josephson-junction qubit. *Phys. Rev. Lett.* **89,** 117901 (2002).
14. *The SQUID Handbook: Fundamentals and Technology of SQUIDs and SQUID Systems* Vol. I (eds Clarke, J. & Braginski, A. I.) (Wiley, Weinheim, 2004).
15. Wilhelm, F. K. *et al.* Macroscopic quantum superposition of current states in a Josephson junction loop. *Usp. Fiz. Nauk* **44** (suppl. 171), 117–121 (2001).
16. Devoret, M. H. & Schoelkopf, R., Amplifying quantum signals with the single-electron transistor. *Nature* **406,** 1039–1046 (2000).
17. Schoelkopf, R. J., Wahlgren, P., Kozhevnikov, A. A., Delsing, P. & Prober, D. E. The radio-frequency single-electron transistor (RF-SET): a fast and ultrasensitive electrometer. *Science* **280,** 1238–1242 (1998).
18. Bouchiat, V., Vion, D., Joyez, P., Esteve, D. & Devoret, M. H. Quantum coherence with a single Cooper pair. *Physica Scripta* **T76,** 165–170 (1998).
19. Nakamura, Y., Pashkin, Y. A. & Tsai, J. S., Coherent control of macroscopic quantum states in a single-Cooper-pair box. *Nature* **398,** 786–788 (1999).

© 2008 Macmillan Publishers Limited. All rights reserved

20. Koch, J. *et al.* Charge-insensitive qubit design derived from the Cooper pair box. *Phys. Rev. A* **76,** 042319 (2007).
21. Ithier, G. *et al.* Decoherence in a superconducting quantum bit circuit *Phys. Rev. B* **72,** 134519 (2005).
22. Siddiqi, I. *et al.* Direct observation of dynamical bifurcation between two driven oscillation states of a Josephson junction. *Phys. Rev. Lett.* **94,** 027005 (2005).
23. Braginsky, V. B., Khalili, F. Y. & Thorne, K. S. *Quantum Measurement* (Cambridge Univ. Press, Cambridge, UK, 1995).
24. Lupaşcu, A. *et al.* Quantum non-demolition measurement of a superconducting two-level system. *Nature Phys.* **3,** 119–125 (2007).
25. Grajcar, M. *et al.* Low-frequency measurement of the tunneling amplitude in a flux qubit. *Phys. Rev. B* **69,** 060501 (2004).
26. Cooper, K. B. *et al.* Observation of quantum oscillations between a Josephson phase qubit and a microscopic resonator using fast readout. *Phys. Rev. Lett.* **93,** 180401 (2004).
27. Slichter C. P. *Principles of Nuclear Magnetic Resonance* 3rd edn (Springer, New York, 1990).
28. Makhlin, Y., Schön, G. & Shnirman, A. Quantum-state engineering with Josephson-junction devices. *Rev. Mod. Phys.* **73,** 357–400 (2001).
29. Wilhelm, F. K., Hartmann, U., Storcz, M. J. & Geller, M. R. in *Manipulating Quantum Coherence in Solid State Systems* (eds Flatté, M. E. & Tifrea, I.) 195–233 (Springer, Dordrecht, 2007).
30. Ramsey, N. F. A molecular beam resonance method with separated oscillating fields. *Phys. Rev.* **78,** 695–699 (1950).
31. Steffen, M. *et al.* State tomography of capacitively shunted phase qubits with high fidelity. *Phys. Rev. Lett.* **97,** 050502 (2006).
32. Dutta P. & Horn P. M. Low frequency fluctuations in solids: 1/*f* noise. *Rev. Mod. Phys.* **53,** 497–516 (1981).
33. van Harlingen, D. J. *et al.* Decoherence in Josephson-junction qubits due to critical-current fluctuations. *Phys. Rev. B* **70,** 064517 (2004).
34. Wellstood, F. C., Urbina, C. & Clarke, J. Low-frequency noise in dc superconducting quantum interference devices below 1 K. *Appl. Phys. Lett.* **50,** 772–774 (1987).
35. Koch, R. H., DiVincenzo, D. P. & Clarke, J. Model for 1/*f* flux noise in SQUIDs and qubits. *Phys. Rev. Lett.* **98,** 267003 (2007).
36. Faoro, L. & Ioffe, L. B. Microscopic origin of low-frequency flux noise in Josephson circuits. Preprint at <http://arxiv.org/abs/0712.2834> (2007).
37. Simmonds, R. W., Lang, K. M., Hite, D. A., Pappas, D. P. & Martinis, J. M. Decoherence in Josephson qubits from junction resonances. *Phys. Rev. Lett.* **93,** 077033 (2004).
38. Martinis, J. M. *et al.* Decoherence in Josephson qubits from dielectric loss. *Phys. Rev. Lett.* **95,** 210503 (2005).
39. Nakamura, Y., Pashkin, Y. A., Yamamoto, T. & Tsai, J. S. Charge echo in a Cooper-pair box. *Phys. Rev. Lett.* **88,** 047901 (2002).
40. Bertet, P. *et al.* Relaxation and dephasing in a flux-qubit. *Phys. Rev. Lett.* **95,** 257002 (2005).
41. Astafiev, O., Pashkin, Y. A., Nakamura, Y., Yamamoto, T. & Tsai, J. S. Quantum noise in the Josephson charge qubit. *Phys. Rev. Lett.* **93,** 267007 (2004).
42. Berkley, A.J. *et al.* Entangled macroscopic quantum states in two superconducting qubits. *Science* **300,** 1548–1550 (2003).
43. Majer, J. B., Paauw, F. G., ter Haar, A. C. J., Harmans, C. J. P. M. & Mooij, J. E. Spectroscopy of coupled flux qubits. *Phys. Rev. Lett.* **94,** 090501 (2005).
44. Pashkin, Y. A. *et al.* Quantum oscillations in two coupled charge qubits. *Nature* **421,** 823–826 (2003).
45. McDermott, R. *et al.* Simultaneous state measurement of coupled Josephson phase qubits. *Science* **307,** 1299–1302 (2005).
46. Steffen, M. *et al.* Measurement of the entanglement of two superconducting qubits via state tomography. *Science* **313,** 1423–1425 (2006).
47. Yamamoto, Y., Pashkin, Y. A., Astafiev, O., Nakamura, Y. & Tsai, J. S. Demonstration of conditional gate operation using superconducting charge qubits. *Nature* **425,** 941–944 (2003).
48. Plantenberg, J. H., de Groot, P. C., Harmans, C. J. & Mooij, J. E. Demonstration of controlled-NOT quantum gates on a pair of superconducting quantum bits. *Nature* **447,** 836–839 (2007).
49. Plourde, B. L. T. *et al.* Entangling flux qubits with a bipolar dynamic inductance. *Phys. Rev. B* **70,** 140501 (2004).
50. Hime, T. *et al.* Solid-state qubits with current-controlled coupling. *Science* **314,** 1427–1429 (2006).
51. Niskanen, A. O. *et al.* Quantum coherent tunable coupling of superconducting qubits. *Science* **316,** 723–726 (2007).
52. Averin, D. V. & Bruder, C. Variable electrostatic transformer controllable coupling of two charge qubits. *Phys. Rev. Lett.* **91,** 057003 (2003).
53. Bertet, P., Harmans, C. J. P.M. & Mooij, J. E. Parametic coupling for superconducting qubits. *Phys. Rev. B* **73,** 064512 (2006).
54. Rigetti, C., Blais, A. & Devoret, M. Protocol for universal gates in optimally biased superconducting qubits. *Phys. Rev. Lett.* **94,** 240502 (2005).
55. Liu, Y.-x., Wei, L. F., Tsai, J. S. & Nori, F. Controllable coupling between flux qubits. *Phys. Rev. Lett.* **96,** 067003 (2006).
56. Makhlin, Y., Schön, G. & Shnirman, A. Josephson-junction qubits with controlled couplings. *Nature* **398,** 305–307 (1999).
57. Wei, L. F., Liu, Y.-x. & Nori, F. Quantum computation with Josephson qubits using a current-biased information bus. *Phys. Rev. B* **71,** 134506 (2005).
58. Lantz, J., Wallquist, M., Shumeiko, V. S. & Wendin, G. Josephson junction qubit network with current-controlled interaction. *Phys. Rev. B* **70,** 140507 (2004).
59. Blais, A., Huang, R.-S., Wallraff, A., Girvin, S. M. & Schoelkopf, R. J. Cavity quantum electrodynamics for superconducting electrical circuits: an architecture for quantum computation. *Phys. Rev. A* **69,** 062320 (2004).
60. Helmer, F. *et al.* Two-dimensional cavity grid for scalable quantum computation with superconducting circuits. Preprint at <http://arxiv.org/abs/0706.3625> (2007).
61. Majer, J. B. *et al.* Coupling superconducting qubits via a cavity bus. *Nature* **449,** 443–447 (2007).
62. Sillanpaa, M. A., Park, J. I. & Simmonds, R. W. Coherent quantum state storage and transfer between two phase qubits via a resonant cavity. *Nature* **449,** 438–442 (2007).
63. Fowler, A. G. *et al.* Long-range coupling and scalable architecture for superconducting flux qubits. *Phys. Rev. B* **76,** 174507 (2007).
64. Grajcar, M. *et al.* Four-qubit device with mixed couplings. *Phys. Rev. Lett.* **96,** 047006 (2006).
65. Devoret, M. H. *et al.* in *Quantum Tunneling in Condensed Media* (eds Kagan, Y. & Leggett, A. J.) 313–345 (Elsevier, Amsterdam, 1992).
66. Haroche, S. & Kleppner, D. Cavity quantum electrodynamics. *Phys. Today* **42,** 24–26 (1989).
67. Wallraff, A. *et al.* Strong coupling of a single photon to a superconducting qubit using circuit quantum electrodynamics. *Nature* **431,** 162–167 (2004).
68. Johansson, J. *et al.* Vacuum Rabi oscillations in a macroscopic superconducting qubit *LC* oscillator system. *Phys. Rev. Lett.* **96,** 127006 (2006).
69. Schuster, D. I. *et al.* Resolving photon number states in a superconducting circuit. *Nature* **445,** 515–518 (2007).
70. Houck, A. A. *et al.* Generating single microwave photons in a circuit. *Nature* **449,** 443–447 (2007).
71. Astafiev, O. *et al.* Single artificial-atom lasing. *Nature* **449,** 588–590 (2007).
72. Valenzuela, S. O. *et al.* Microwave-induced cooling of a superconducting qubit. *Science* **314,** 1589–1592 (2006).
73. Gracjar, M. *et al.* Sisyphus damping and amplification by a superconducting qubit. Preprint at <http://arxiv.org/abs/0708.0665> (2007).
74. Clauser, J. F., Horne, M. A., Shimony, A. & Holt, R. A. Proposed experiment to test local hidden-variable theories. *Phys. Rev. Lett.* **23,** 880–884 (1969).
75. Leggett, A. J. & Garg, A. Quantum mechanics versus macroscopic realism: is the flux there when nobody looks? *Phys. Rev. Lett.* **54,** 857–860 (1985).
76. Bennett, C. H. *et al.* Teleporting an unknown quantum state via dual classical and Einstein–Podolsky–Rosen channels. *Phys. Rev. Lett.* **70** 1895–1899 (1993).
77. Schreier, J. A. *et al.* Suppressing charge noise decoherence in superconducting charge qubits. *Phys. Rev. B* **77,** 180502 (2008).
78. Duty, T., Gunnarson, D., Bladh, K. & Delsing, P. Coherent dynamics of a Josephson charge qubit. *Phys. Rev. B* **69**, 140503 (2004).
79. Dolan, G. J. Offset masks for liftoff photoprocessing. *Appl. Phys. Lett.* **31,** 337–339 (1977).

Acknowledgements Our work is supported by the US Department of Energy (Division of Materials Sciences and Engineering, in the Office of Basic Energy Sciences) (J.C.), and by the Natural Sciences and Engineering Research Council of Canada, QuantumWorks and EuroSQIP (F.K.W.).

Author Information Reprints and permissions information is available at npg.nature.com/reprints. The authors declare no competing financial interests. Correspondence should be addressed to the authors (jclarke@berkeley.edu; fwilhelm@iqc.ca).

© 2008 Macmillan Publishers Limited. All rights reserved

Coherent manipulation of single spins in semiconductors

Ronald Hanson[1] & David D. Awschalom[2]

During the past few years, researchers have gained unprecedented control over spins in the solid state. What was considered almost impossible a decade ago, in both conceptual and practical terms, is now a reality: single spins can be isolated, initialized, coherently manipulated and read out using both electrical and optical techniques. Progress has been made towards full control of the quantum states of single and coupled spins in a variety of semiconductors and nanostructures, and towards understanding the mechanisms through which spins lose coherence in these systems. These abilities will allow pioneering investigations of fundamental quantum-mechanical processes and provide pathways towards applications in quantum information processing.

In the past few decades, the application of nuclear magnetic resonance and electron spin resonance to large spin ensembles has yielded substantial information on spin dynamics in semiconductors. Experimental advances since the 1990s have allowed researchers to increase their control over single charges, providing a pathway for studies of single spins. Early experiments on single spins confined in semiconductor quantum dots highlighted the opportunity for controlling individual quantum states in a solid.

When quantum information processing became a realistic prospect in the late 1990s, Daniel Loss and David DiVincenzo proposed a quantum computing scheme based on spins in quantum dots[1], and Bruce Kane developed a proposal for a silicon-based quantum computer[2]. It was apparent from these and other theoretical concepts that, in a future quantum computer, the spins must be initialized, manipulated and read out one by one[3]. At about the same time, other researchers were independently developing 'toolkits' of sensitive spin-manipulation techniques to investigate fundamental quantum-mechanical processes in nanostructures such as decoherence on the atomic scale. Ultimately, around the start of this century, spintronics emerged[4], a field that seeks to encode classical information in the spin state of electrons. Both spintronics and quantum information processing have been major driving forces towards the control of single-spin systems.

Here we review experimental progress towards full control of the quantum states of single and coupled spins in different semiconductor systems. We also discuss the mechanisms that lead to the loss of spin coherence in these systems.

Single spins in semiconductors

Single-spin systems in semiconductors broadly fall into two categories: atomic impurities and quantum dots. Atomic impurities are routinely added to semiconductors to control the electrical properties (doping). When the concentration of impurities is very low, the possibility of addressing individual impurities arises. Atomic impurities may have nuclear spin, or they can act as a potential trap for electrons or holes. Often they do both, as in the case of phosphorus in silicon. If two or more impurities are present, or if there is a combination of impurities and lattice defects such as a vacancy, more complicated 'centres' can be formed that often have excellent properties for single-spin studies. One prime example is the nitrogen–vacancy (N–V) colour centre in diamond, which consists of a substitutional nitrogen atom next to a missing carbon (the vacancy) (Fig. 1). This N–V centre has a paramagnetic electron spin and a strong optical transition at a visible wavelength, which allows optical imaging of single spins.

Quantum dots, by contrast, behave like atoms in many ways, but they are fabricated in the laboratory. By engineering the electronic band structure, reducing the size of the semiconductor crystal in one or more dimensions, or applying electric fields, charge carriers can be confined to a small region of the crystal. If the region is roughly the same size as the wavelength of the charge carrier, the energy levels will be quantized as in real atoms. Many atomic properties, such as shell structure and optical selection rules, have analogues in quantum dots, giving rise to their nickname 'artificial atoms'[5–7]. In contrast to real atoms, however, quantum dots allow flexible control over the confinement potential and tend to be easier to excite optically. Quantum dots with large tunnel coupling (that is, strong overlap of their electronic wavefunctions) can form 'artificial molecules'. Such covalent bonding transforms the single-dot orbitals into molecular-like orbitals that span both quantum dots. As a consequence, spins in neighbouring coupled quantum dots overlap strongly and will form two-particle wavefunctions such as spin singlet and triplet states[8].

Quantum dots come in various sizes and in a range of materials. Here we mainly focus on the two types of quantum dot in which coherent dynamics have been observed at the single-spin level. In the first type, confinement is achieved through the application of electric fields, and measurements typically involve the transport of charge carriers through the device. Quantum dots with a tunable number of electrons are routinely fabricated from a two-dimensional electron gas (2DEG) that confines the charge carriers to a plane. Confinement in the remaining two dimensions is achieved by electric fields, either through metallic surface gates above the 2DEG (Fig. 1a) or, if a small pillar has been prepared by etching, from the edges. Gallium arsenide (GaAs) has been the material of choice for many years for these devices, as the high level of control has led to high-purity, flexible devices. More recently, motivated by the detrimental effect of lattice nuclear spins on the coherence times of electron spins, quantum dots have also been studied in materials such as silicon and carbon that can be isotopically purified to obtain a lattice that is free of nuclear spins.

[1]Kavli Institute of Nanoscience Delft, Delft University of Technology, P.O. Box 5046, 2600 GA Delft, The Netherlands. [2]California Nanosystems Institute, University of California, Santa Barbara, California 93106, USA.

© 2008 Macmillan Publishers Limited. All rights reserved

The second type of quantum dot is defined in the semiconductor during the growth of the crystal. For instance, small islands of semiconductor material such as indium gallium arsenide (InGaAs) can be created within a matrix of a semiconductor with a larger bandgap, such as GaAs (Fig. 1b). The difference in bandgap confines charge carriers to the island. Once the material is grown, the bandgap profile is fixed. However, changes to the overall potential, and potential gradients on top of the bandgap profile, can be induced by electric or magnetic fields. Another example of growth-defined dots is nanocrystal quantum dots, whose small size confines charge carriers. Double dots can be formed in nanocrystal dots by growing shells of different materials around the core.

Optical transitions in this second type of quantum dot typically have a large oscillator strength, and many studies use only optical techniques. Recent years have also seen the advent of hybrid systems, in which both electrical transport and optical excitation and detection are possible[9].

Experiments on single spins in quantum dots

In the 1990s, measurements of electron transport through single quantum dots yielded information about spin states[10]. The past five years have seen tremendous progress towards the control of single spins[8]. Single-spin dynamics was first studied in a series of pioneering experiments[11] at the NTT Basic Research Laboratories in Atsugi, Japan, in 2001 that made use of fast voltage pulses on gate electrodes. Toshimasa Fujisawa, Seigo Tarucha and co-workers found that if a transition between two states was forbidden by spin-selection rules, the corresponding decay time (more than 200 μs) was more than four orders of magnitude greater than for transitions not involving a change of spin (about 10 ns). In a second experiment, they made a single electron oscillate coherently between orbitals in neighbouring coupled dots[12]. The orbital ('charge') coherence of this oscillation was found to disappear in just a few nanoseconds, whereas theory was predicting coherence times of several microseconds for the spin degree of freedom[13–15].

In 2004, Leo Kouwenhoven and co-workers at the Kavli Institute of Nanoscience in Delft, the Netherlands, combined the pulse schemes of Fujisawa's group with a fast charge sensor that could tell exactly when an electron was entering or leaving the dot. By making the tunnelling rate of the electron from the dot dependent on its spin state, they could determine the spin state by measuring the charge on the dot over time (Fig. 2a). Two variations of this spin-to-charge conversion were demonstrated to work in single-shot mode[16,17]. Again, relaxation times for a single electron and for two-electron spin states were found to be of the order of a millisecond. A few years later, even longer electron spin relaxation times, of up to a second, were found at magnetic fields of a few tesla by Marc Kastner's group at the Massachusetts Institute of Technology in Cambridge[18].

Coherent control over two-electron spin states

Two electrons in neighbouring quantum dots with a significant tunnel coupling form a two-particle spin wavefunction, which can be a spin singlet or a spin triplet. The energy difference between these states can be described as an effective exchange splitting, $J(t)$. Control over this exchange splitting allows dynamical control of the two-electron spin states. If two electrons with opposite spin orientation in neighbouring dots are initially decoupled, turning on the coupling will result in a precession of the two spins in the singlet–triplet basis. This leads to periodic swapping of the two spin states at integer multiples of the time interval $\pi\hbar/J$ (where $\hbar$ is $h/2\pi$ and h is Planck's constant), whereas the electrons are entangled for intermediate times[1]. In fact, the state swapping occurs for arbitrary initial states of the two spins. This two-spin control, appropriately called a SWAP operation, is an essential ingredient for many proposals for quantum computing with spins in dots[19–21]. If logical quantum bits (qubits) are encoded in more than one spin, control over the exchange splitting is sufficient to build up any quantum gate[22]. The exchange operation has several benefits: the control is fully electrical, the interaction can be turned on and off, and the resultant gate operation times can be very short (less than a nanosecond).

The first step towards the exchange operation was the observation by Tarucha's group[23] of Pauli spin blockade in a double quantum dot. The presence of double-dot singlet and triplet states became apparent when the current was suppressed in one bias direction (Fig. 2c). It was later found that this current blockade can be lifted by fluctuating fields from the nuclear spins that cause mixing of the singlet and triplet spin states[24,25]. In 2005, by using the strength of the exchange interaction to control the mixing, Charles Marcus's group at Harvard University in Cambridge, Massachusetts, demonstrated coherent oscillations of two spins[26]. Although it was not yet possible to probe arbitrary input states, this experiment demonstrated the essence of the SWAP gate.

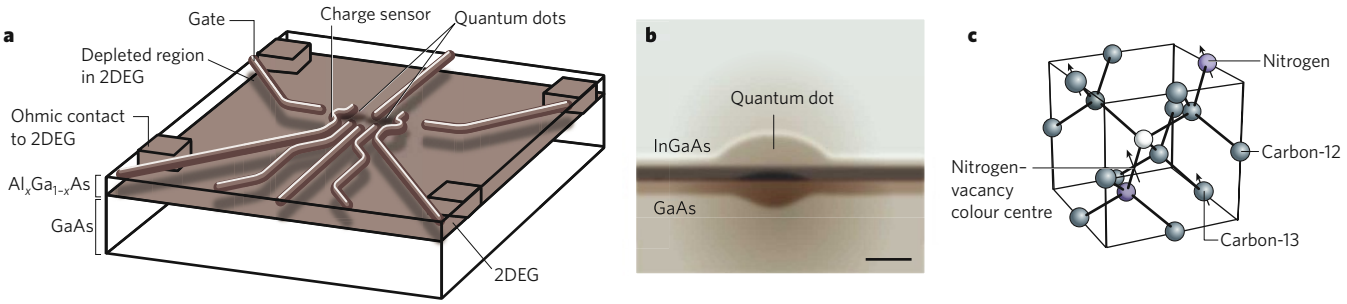

Figure 1 | Single-spin systems. Studies of the coherence of a single spin require a system in which the spin is localized and isolated from environmental disturbances. In semiconductors, such systems are either impurity atoms or quantum dots, which act as artificial atoms. In the three systems on which this article mainly focuses, the level of experimental control is so high that the dynamics of a single spin can be studied and manipulated. **a**, A quantum dot defined in a two-dimensional electron gas (2DEG). The electrons are confined in the third dimension by electric fields from the surface gate electrodes. Electron spins can be manipulated using magnetic resonance or a combination of electric fields and a position-dependent effective magnetic field. Interactions between spins in neighbouring tunnel-coupled dots are mediated by the exchange interaction. These quantum dots are typically measured at temperatures below 1 K. **b**, A quantum dot defined by growth. The semiconductor of the island has a smaller bandgap than that of the surrounding matrix, thereby confining charge carriers to the island. Spins can be created and controlled optically. Additional gates can be used to apply an electric field to the structure to change the number of carriers on the quantum dot. Measurements are typically carried out at around 4 K. Scale bar, 5 nm. **c**, A nitrogen–vacancy (N–V) colour centre in diamond, consisting of a substitutional nitrogen atom next to a missing carbon atom. The N–V centre (in the negatively charged state) comprises six electrons that form a spin triplet in the electronic ground state. Strong optical transitions to excited states, in combination with spin-selection rules, allow optical initialization and read-out of the electron spin. Coherent control of the spin has been demonstrated with high fidelity at room temperature using magnetic resonance. The N–V centre interacts with nearby electron spins by means of magnetic dipolar coupling, and through hyperfine interaction with nearby nuclear spins. Also, non-local coupling between N–V centres may be established by using the optical transition; photons then act as mediators of the interaction.

© 2008 Macmillan Publishers Limited. All rights reserved

Single-spin rotations

A year after the coherent two-spin experiments, the Delft group, now headed by Lieven Vandersypen, demonstrated single-spin control[27] through magnetic resonance. In this technique, an oscillating magnetic field is applied perpendicular to the static magnetic field. When the frequency of the oscillating field is matched to the energy difference of the two spin states, the spins are rotated coherently.

Although electric fields do not couple directly to the spin, a coupling between the two can be mediated through a position-dependent effective magnetic field. By 'shaking' the electron in this field gradient, an oscillating effective magnetic field is imposed on the electron that can coherently rotate the spin (see, for example, ref. 28). A few examples of this approach have already been demonstrated in a quantum dot by exploiting a gradient in the nuclear spin polarization[29], a field gradient from a micromagnet[30], and the spin–orbit coupling[31]. In the last case, coherent control has been achieved on a timescale similar to that obtained with magnetic resonance (about 100 ns for a single rotation). In comparison to magnetic resonance, electrical control has the important advantage that it allows spins to be easily addressed locally, because electric fields are much easier to confine to small regions of space than magnetic fields.

Experiments on optically measured quantum dots

The physics of optically measured quantum dots is very similar to that of those studied electrically, but the experimental techniques differ markedly. Experiments on quantum dots in group III–V and group II–VI semiconductors, such as InGaAs dots in a GaAs matrix, make use of optical-selection rules in these materials. Shining circularly polarized light onto the material excites electron–hole pairs with specific spin. This has become a standard method for exciting packets of spin-polarized electrons in semiconductors and studying their coherent behaviour[32].

In a quantum dot, the same technique applies but with limited space for charge carriers. With proper tuning, the number of excited electron–hole pairs in the dot can be limited to one. In this way, a single electron and single hole can be created with well-defined spin states, in addition to any permanent charge carriers in the dot. The spin-selection rules also work the other way: when an electron–hole pair recombines, the polarization of the emitted photon tells us what the spins of the electron and the hole were. Optical-selection rules thereby allow the initialization and read-out of the spin states (Fig. 2d).

Optical techniques have been used to probe the stability of electron spins. In 2004, Jonathan Finley and co-workers at the Walter Schottky Institute in Munich, Germany, optically pumped electron–hole pairs that had a specific spin orientation into a large number of quantum dots. They then removed the holes by rapidly changing the electrical potential of the dots[33]. After a variable time, they reinserted a hole into each dot to allow recombination, and monitored the polarization of the emitted photons, which reflects the spin of the captured electrons. In these ensemble measurements, the electron spin could be found in the same orientation even after 20 ms. Finley and co-workers have recently repeated the spin relaxation measurements for single holes[34]. For a long time, it was thought that these hole spins would lose their orientation quickly as a result of strong spin–orbit coupling in the valence band. However, Finley's data pointed to very long hole-spin relaxation times of up to 300 μs, as predicted by a recent theory from Loss and co-workers at the University of Basel, Switzerland, that takes into account the confinement potential and strain[35]. Future experiments will seek to obtain coherent control of the hole spin state and determine the spin coherence time.

The spin orientation of electrons can also be inferred from the Kerr effect, in which the linear polarization of an incident laser beam is rotated in proportion to the spin polarization of electrons. This powerful technique has become a standard method for studying spin dynamics in semiconductors. It has recently been extended to the single-spin limit by the group of David Awschalom at the University of California, Santa Barbara[36], and subsequently by the group of Atac Imamoglu at ETH Zurich, Switzerland[37]. With this single-spin sensitivity, time-resolved observation of the precession of a single spin in a magnetic field has been achieved[38].

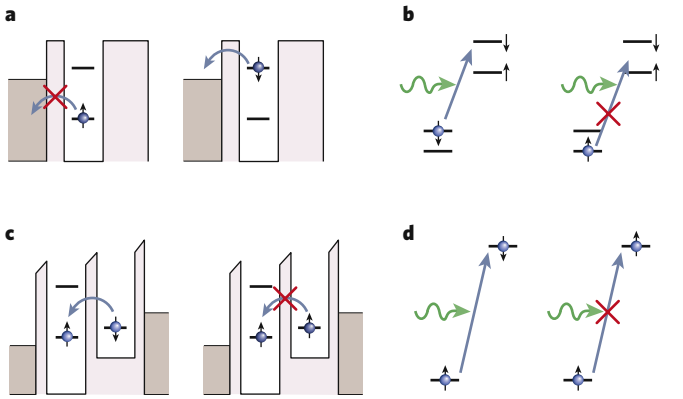

Figure 2 | Single-spin read-out. Studying a single spin is difficult because the magnetic moment of a spin is very small. Several spin read-out techniques have been developed in which the spin information is transferred to quantities that are more easily measured, such as electric charge or the polarization of light. This conversion requires that a transition between two states depends on the initial spin state; several examples of such transitions that are used in experiments are shown. **a**, **b**, Conversion of spin-state information into electric charge or photons by exploiting the energy difference between spin states. In **a**, an electron can tunnel from the quantum dot to the reservoir only if it is in the spin-down state. Measurement of the charge on the dot yields the spin state. **b**, A colour centre or quantum dot is optically excited and subsequently emits a photon only if it is in the spin-down state. The laser light is not resonant for the other spin state. Using a sensitive photon counter, the spin state can be determined after several optical cycles[65]. **c**, **d**, Spin read-out by spin-selection rules. The Pauli principle forbids two electrons with the same spin orientation to occupy a single orbital. Therefore, if one electron occupies an orbital, a second electron cannot enter if it has the same spin. Transitions that conserve spin (such as tunnelling and electric dipole transitions) can thus be blocked for certain spin states, hence the name 'Pauli spin blockade'. **c**, In a double quantum dot, the transition from the right dot to the left dot is blocked if the two electrons involved have the same spin. The second electron needs to go into a higher orbital, which is energetically not available. **d**, Circularly polarized laser light excites electrons with a certain spin orientation out of the valence band to the lowest orbital in the conduction band in a quantum dot. If an electron with the same spin orientation is already present in that orbital, the transition is forbidden.

Optical techniques also allow the coherent manipulation of spins. One method that has been proposed in the context of quantum information processing makes use of Raman transitions of spins in a microcavity[39]. Alternatively, single spins may be manipulated using the a.c. Stark effect[40], in which an intense laser pulse at a frequency slightly below the optical transition renormalizes the energy of the optical transition. When circularly polarized light is used, only one of the two spin states is affected by the laser pulse, resulting in an energy shift between spin up and spin down. This shift, known as the a.c. Stark shift, acts as an effective magnetic field along the light propagation direction; the magnitude of this field depends both on the detuning of the laser with respect to the optical transition and on the intensity of the pulse. Awschalom's group recently used the a.c. Stark effect to manipulate a single electron spin[41]. Short laser pulses were shown to induce rotations of the spin over an angle up to 180° in a time interval as short as 30 ps. This is about three orders of magnitude faster than any magnetic or electrical manipulation on single spins in quantum dots achieved thus far and is an important improvement in the context of quantum error correction.

Loss of spin coherence in quantum dots

In this discussion, we distinguish between energy relaxation processes (typically characterized by a spin relaxation time, T_1) and phase relaxation processes (characterized by a spin coherence time, T_2). By definition, T_1 sets a bound on T_2 such that $T_2 \leq 2T_1$. For successful quantum error correction, T_2 must exceed the spin manipulation time by several

© 2008 Macmillan Publishers Limited. All rights reserved

orders of magnitude. A third timescale, T_2^*, is often used to denote the time after which the electron phase is randomized during free evolution. If the spin manipulation time is less than T_2^*, the fidelity of the control can be severely reduced, which adds a second requirement for quantum information application.

Quantum coherence of spins in semiconductor quantum dots is limited by coupling to other degrees of freedom in the environment. Electrons or holes can couple to states outside the quantum dot (Fig. 3a), and fluctuations in the electrical potential can indirectly lead to decoherence of the spin (Fig. 3b).

The absence of inversion symmetry in the lattice and the presence of electric fields or confinement asymmetries lead to coupling between spin and the motion of electrons (Fig. 3c). This spin–orbit coupling mixes the spin eigenstates. Except for small energy splitting, spin relaxation in group III–V quantum dots is typically dominated by spin–orbit coupling in combination with phonon emission that takes away the excess energy. Measurements of the spin relaxation time in many different devices have confirmed the theoretically predicted dependence on magnetic field and temperature[8]. However, the phase of localized electron spins is much less sensitive to the spin–orbit coupling[15]. The spin decoherence time, T_2, of electrons in group III–V quantum dots is typically limited by the nuclear spins (Fig. 3d).

The hyperfine interaction with the nuclear spins has two effects on the electron spin[42]. First, each nuclear spin exerts a tiny effective magnetic field on the electron spin. The sum of the fields of the roughly 1 million nuclear spins in a quantum dot, known as the Overhauser field, can be large (up to several tesla) if the nuclear spins all point in the same direction. The magnetic moment associated with the nuclear spins is small, so the thermal polarization is tiny even at millikelvin temperatures. However, the Overhauser field still fluctuates around this tiny average. A simple estimate tells us that for n nuclear spins, the statistical variation is of the order of $\sqrt{n}$, which corresponds to an effective magnetic field of a few millitesla for a typical group III–V quantum dot. Such a field causes the phase of the electron spin to change by π in roughly 10 ns. A measurement usually lasts tens of seconds, during which time the nuclear spins change orientation many times. One measurement therefore yields an average over many different nuclear spin configurations, leading to random phase variations between successive measurements. This leads to a dephasing time, T_2^*, of about 10 ns (refs 13, 14), a timescale that was first verified in optical experiments[43,44].

The Overhauser field changes slowly relative to the spin manipulation time, because the nuclear spins interact weakly both among themselves and with their surroundings. For example, recent optical experiments indicate that, in certain circumstances, nuclear spin polarizations in quantum dots can sometimes survive for up to an hour[45]. Simple spin-echo techniques can therefore be used to eliminate the effect of the quasi-static Overhauser field, provided that the electron spin can be manipulated on a timescale that is short compared with the spin precession time in the Overhauser field. There are two approaches to achieving this. The most straightforward is to make the manipulation time very short, either by using the exchange energy in two-spin systems or by optical manipulation using the a.c. Stark effect. Alternatively, the Overhauser field can be made smaller. One way of doing this is to narrow the distribution of the Overhauser fields by bringing the nuclear spins to a specific and stable quantum state[46–48]. Another option is to polarize all of the nuclear spins. Nuclear spin polarizations of up to 60% have been measured in quantum dots[44,49], but it is anticipated that a polarization far above 90% is required for a significant effect[50].

Another effect of the nuclear spins on the electron spin coherence comes from flip-flop processes[42], in which a flip of the electron spin (say from spin up to spin down) is accompanied by a flop of one nuclear spin (from spin down to spin up). In a first-order process, this leads to spin relaxation (the electron spin is flipped). If the electron spin is continuously repolarized, for example by optical pumping, the nuclear spins will all be flopped into the same spin state. After many such flip-flop events, a significant nuclear spin polarization can arise. This process is called dynamical nuclear polarization. If there is a large energy mismatch between the electron spin splitting and the nuclear spin splitting (because there is an external magnetic field, for instance), this first-order process is strongly suppressed. Second-order processes — in which two nuclear spins exchange their state by two flip-flops with the electron spin — are still possible. Through these virtual flip-flops, the nuclear spins can change orientation much faster than is possible with the magnetic dipolar interaction with nearby nuclear spins. This effectively leads to spin diffusion. The observed T_2 of about a microsecond is thought to be compatible with this picture, although firm experimental evidence isolating the different causes of nuclear field fluctuations is still lacking[8].

Spins of holes in the valence band of group III–V semiconductors have wavefunctions that have zero weight at the position of the nuclei, so the contact hyperfine interaction should not affect the coherence of holes. Richard Warburton and co-workers have recently initialized single hole spins in quantum dots at zero magnetic field[51] by adapting a procedure that was previously demonstrated on single electron spins[52].

The detrimental effect of the nuclear spins on the coherence in quantum dots has also spurred research into materials systems that contain

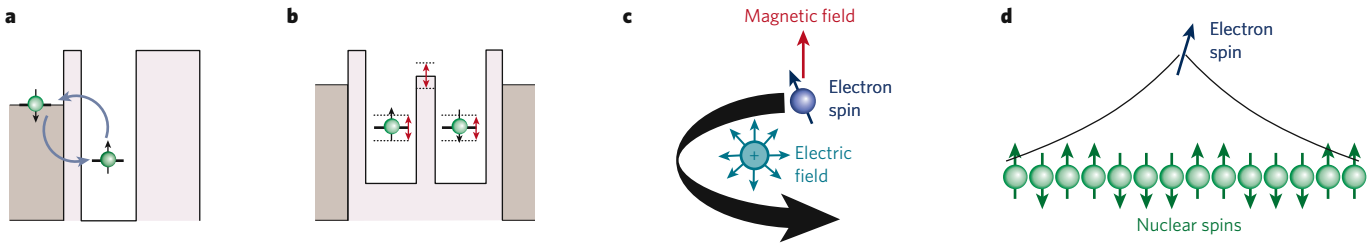

Figure 3 | Spin decoherence in quantum dots. The coherence of spins in quantum dots is affected by several mechanisms. **a**, Co-tunnelling. Although energy conservation forbids first-order tunnelling of charge carriers to states outside the dot at higher energy, second-order tunnelling processes (co-tunnelling) — in which a charge carrier tunnels from the dot to a reservoir and is replaced by a different charge carrier from the reservoir — are allowed[83]. The charge carrier from the reservoir will in general not be in the same spin quantum state as the one that first occupied the dot, so this process causes spin coherence to be lost. By increasing the energy difference between the dot and the reservoir states, and also making the tunnel coupling between them small, co-tunnelling processes can effectively be suppressed. **b**, Charge noise. Fluctuations in the electrical potential (charge noise) do not couple directly to the spin but can influence the spin dynamics indirectly. For example, the energy splitting, J, between singlet and triplet states in a double quantum dot depends strongly on the height of the tunnel barrier between the dots and the alignment of the levels in the dots. Any changes in the electrostatic environment can lead to changes (indicated by red arrows) in the barrier height and level misalignment, which modify J and therefore induce random phase shifts between the singlet and triplet states[84,85]. Charge switching and gate-voltage noise are two possible causes for such changes[86]. **c**, Spin–orbit coupling. The coupling between the spin and orbital of charge carriers leads to mixing of the spin states in a quantum dot. As a result of this coupling, any disturbance of the orbitals leads to phase fluctuations of the spin state. **d**, Nuclear spins. The charge carriers in the dot couple to the nuclear spins of the host material. These nuclear spins exert an effective magnetic field, and allow spin flip-flop processes that lead to spin relaxation and decoherence.

© 2008 Macmillan Publishers Limited. All rights reserved

fewer or no nuclear spins. Two prominent examples are carbon and silicon, which can both be purified isotopically to yield a zero-spin lattice. Single and double quantum dots have been studied in these systems for several years, with control now approaching the level of GaAs systems[53–57]. Experiments probing the spin coherence times in silicon and carbon quantum dots are expected in the near future.

Coherent control of magnetic dopants

In contrast to non-magnetic nanostructures, individual magnetic-ion spins can be doped within group II–VI semiconductor quantum dots and measured through their exchange coupling to the electrons and holes. Statistically, it is possible to find an ion-impurity spin that is randomly doped at the centre of a single quantum dot. Using self-assembled quantum dots consisting of cadmium telluride and zinc telluride, Lucien Besombes *et al.*[58] isolated an individual paramagnetic manganese ion within individual dots. The micro-photoluminescence spectrum of an exciton (an electron–hole pair) was observed to split into six equally spaced lines owing to the quantization of manganese with a spin of 5/2. The next step was to apply a gate bias and change the charge state of the dot by pulling in either one electron or one hole. In this case, the coupling between the manganese ion and either the hole or the electron splits the six-line spectrum into twelve lines[59], in agreement with models based on spin exchange interactions within diluted magnetic semiconductors[60].

Dilute doping of group III–V semiconductors with manganese ions produces a unique environment for single-ion spin physics. Because the manganese states rest within the bandgap, it is not necessary to isolate a single manganese impurity within a single quantum dot, as the ions themselves act as recombination centres. In analogy with atomic physics, they form their own 'ideal' quantum dot states. The spin state of the manganese ion is independent of the electronic exciton and can be read out directly from the polarization of the manganese neutral acceptor emission[61]. In the absence of an applied magnetic field, the orientation of the magnetic ions is controlled by a dynamic interaction with optical injected electron spins. This mechanism is similar to dynamic nuclear polarization between electron spins and nuclear spins through the hyperfine interaction. After the manganese ions are partially aligned, a mean field interaction between the manganese ions, mediated by heavy hole states, favours a parallel alignment of the magnetic moments, creating a zero field splitting of the manganese-ion spins. The measurements indicate that single manganese-ion spins have longer coherence times than their electronic counterparts, motivating further studies of coherent control of manganese spins in semiconductors.

Coherent control of spins in diamond

Spins in diamond have recently become a leading candidate for solid-state quantum control, owing to their long coherence times and strong optical transitions, as well as the enormous progress that has been made in the growth and engineering of diamond as a unique semiconductor[62]. Ensemble experiments in the late 1990s indicated that spins of impurity centres in diamond can have very long coherence times, even at room temperature[63]. A more recent series of experiments demonstrated high-fidelity coherent control over electron spins and nuclear spins at room temperature at the single-spin level.

Most work is focused on the N–V centre (Fig. 1c) because of its attractive properties for quantum coherent operation[62]: the N–V centre's electronic-level structure allows both optical cooling and optical read-out of the electron spin. In 1997, following progress in confocal microscopy and the availability of diamond samples with a low concentration of N–V centres, Jörg Wrachtrup and co-workers reported the first study[64] of a single N–V-centre spin. In the seven years that followed, Fedor Jelezko, Wrachtrup and co-workers demonstrated single-shot read-out of the N–V electron spin at 1.5 K using resonant laser excitation[65] (Fig. 2b), coherent control of a single spin using magnetic resonance[66], and a two-qubit gate involving the host nuclear spin of the N–V centre[67]. In a parallel development, materials research achieved the growth of diamond using the chemical vapour deposition (CVD) method. With CVD, control over the number of impurity atoms increased enormously, resulting in the availability of very clean layers of diamond. Moreover, diamond nanocrystals of various sizes that contain N–V centres or other colour centres can now be grown[68]. These crystals have the advantage that they are small and light, and can be positioned onto other materials. This may facilitate interfacing spins in diamond with optical components such as fibres and cavities[69].

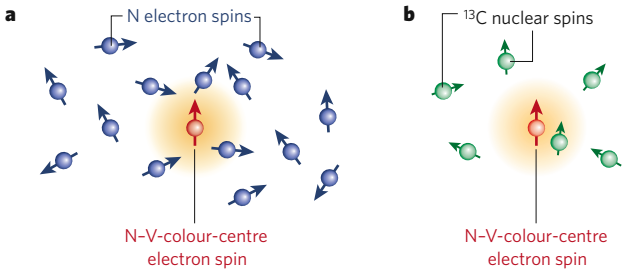

Figure 4 | Control and coherence in diamond. Spins in diamond are unique among solid-state systems in that single spins can be coherently controlled with high fidelity even at room temperature. The amount of impurity spins has a strong influence on coherence properties. **a**, Schematic representation of a nitrogen–vacancy (N–V) centre surrounded by electron spins of nitrogen impurities. In this case, the coherent dynamics of the N–V-centre spin are determined by the nitrogen atom's electron spins; the influence of nuclear spins is negligible because their magnetic moment is three orders of magnitude smaller than that of the electrons. Because an electron spin bath is easily tunable with a magnetic field, these systems allow detailed investigation of spin decoherence models and tests of quantum control in a tunable spin bath[73]. **b**, Schematic representation of an N–V centre surrounded by nuclear spins of carbon-13 in an ultrapure diamond. Nuclear spins that are much closer to the N–V centre than the others (within the orange sphere) stand out from the rest of the nuclear spins and can be individually distinguished and controlled[78].

The coherent evolution of impurity spins in diamond is dominated by magnetic interactions (Fig. 4). Whereas in quantum dots many nuclear spins have identical coupling to the electron spin, the highly localized nature of an impurity spin makes the magnetic interactions strongly dependent on the distance between spins. Other couplings such as a spin–orbit interaction have a much weaker effect at impurities than in quantum dots because of the much larger electronic-level splittings.

For impurity concentrations down to about 1 p.p.m., magnetic dipolar coupling between impurity electron spins dominates spin coherence in diamond[63,70] (Fig. 4a). In some cases, two spins are much closer to each other than to the rest of the spins, in which case the dynamics become a simple two-spin evolution. One example is an N–V centre in close proximity to a single nitrogen impurity, in which case the nitrogen spin can be polarized and read out through the N–V centre[71,72].

In general, an N–V centre will be coupled to many nitrogen spins, which can be viewed as a 'spin bath'. Even in this case, the spin of the N–V centre can be controlled with high fidelity, allowing investigation of decoherence induced by the spin bath. Analogous to an electron spin in a quantum dot that is coupled to a nuclear spin bath, the nitrogen electron spins influence the evolution of the N–V centre in two ways. First, the magnetic dipolar field from the bath shifts the energy splitting between the N–V centre's spin states (analogous to the Overhauser field in quantum dots). It has recently been shown[73] that the interactions within the bath, leading to the fluctuations of the dipolar field, are strongly suppressed when a magnetic field is applied, in which case single-spin flips do not conserve energy. The second effect of the spin bath comes from flip-flop processes with the N–V electron spin. In contrast to a nuclear spin bath (where the spin splitting is tiny), the electron spin bath can be tuned into energy resonance with the N–V-centre electron spin. Resonant flip-flop processes then provide a strong additional decoherence path, leading to much shorter spin coherence times.

Because the spin coherence in diamond is dominated by magnetic interactions, it is not strongly temperature dependent, except at low

© 2008 Macmillan Publishers Limited. All rights reserved

temperatures and high magnetic fields, at which the bath spins polarize thermally; this occurs for electron spins in a field of 8 T at a few kelvin. Recent experiments on a diamond with a high concentration of nitrogen electron spins show that when all of the electron spins are thermally polarized, the fluctuations in the spin bath are completely frozen out and the spin coherence time reaches the same high value as in ultrapure diamond[74].

In most diamonds studied thus far, the positions of the impurity spins were random, affected only by growth parameters. In 2005, single N–V centres were deliberately created by ion-implanting nitrogen[75,76]. This approach may lead to fundamental studies of spin coherence in diamond by designing different spin environments, as well as allow pathways for engineering spin qubits into future scalable quantum information-processing systems.

In diamonds where the impurity concentration is very low (below 1 p.p.m.), the presence of the few nuclear spins of the carbon-13 isotope (which has a natural abundance of 1.1%) becomes apparent. These nuclear spins also constitute a spin bath, which limits the N–V centre's coherence time to a few hundred microseconds[70,71]. Because a single N–V spin can be rotated using magnetic resonance in less than 10 ns, more than 10,000 error-free operations can be performed, which is within the commonly assumed threshold for quantum error correction. As in the case of impurity electron spins, if a few nuclear spins are much closer to the N–V centre than the other nuclear spins, their individual coupling to the N–V-centre spin can be detected[77] (Fig. 4b). Mikhail Lukin's group at Harvard University demonstrated that these nuclear spins can be used to store quantum information for much longer than the electron spin's coherence time[78]. The quantum state of the N–V electron spin can be mapped onto, or retrieved from, the nuclear-spin memory through a combination of state-dependent precession of the nuclear spin and fast optical reinitialization of the N–V-centre spin. Experiments have shown that even on a 20-ms timescale, the nuclear spin shows no sign of decoherence[78], suggesting that nuclear spins may have coherence times of seconds or even longer. By extending the control to multiple nuclear spins, a small quantum memory can be created that will operate at room temperature.

As well as long spin coherence times, N–V centres also have a strong optical transition. Lifetime-limited optical linewidths have been observed[79], and the optical preparation of a coherent superposition of spin states has been demonstrated in coherent population trapping experiments on single N–V centres[80]. These results may, in the future, be extended to dynamical all-optical control of single spins in diamond.

Optical control opens the door to schemes for creating entangled states of spins at large distances[81], in a similar way as was recently demonstrated for atom traps[82]. Such long-distance entanglement is also a crucial ingredient for applications in quantum communication.

Outlook

After enormous progress in recent years, researchers can now initialize, control and read out single spins in semiconductors in a few specific systems, with others likely to be added to the list within a few years. The coherence times of electron spins in materials with few or no nuclear spins, as well as the coherence times of hole spins, are expected to be much longer than for electron spins in group III–V semiconductors. Carbon-based materials, such as carbon nanotubes and graphene, are being heavily investigated; diamond has already shown its potential for quantum coherence studies (at room temperature) with a level of single-spin control that meets the quantum information-processing error-correction threshold.

The emphasis of this research area will shift in the coming years from single-spin control to the creation and manipulation of entangled states of two or more spins, as well as the development of sophisticated quantum control techniques. This will lead the way for more studies on fundamental issues such as decoherence and the role of measurements in quantum mechanics. At the same time, protocols for quantum information processing may be tested in systems with few spins. These are exciting times for 'spin doctors', as they continue to drive a rapidly expanding field that has a promising future. ■

1. Loss, D. & DiVincenzo, D. P. Quantum computation with quantum dots. *Phys. Rev. A* **57,** 120–126 (1998).
2. Kane, B. E. A silicon-based nuclear spin quantum computer. *Nature* **393,** 133–137 (1998).
3. DiVincenzo, D. P. The physical implementation of quantum computation. *Fortschr. Phys.* **48,** 771–783 (2000).
4. Wolf, S. A. *et al.* Spintronics: a spin-based electronics vision for the future. *Science* **294,** 1488–1495 (2001).
5. Kastner, M. A. Artificial atoms. *Phys. Today* **46,** 24–31 (1993).
6. Ashoori, R. C. Electrons in artificial atoms. *Nature* **379,** 413–419 (1996).
7. Kouwenhoven, L. P. & Marcus, C. M. Quantum dots. *Phys. World* **11,** 35–39 (1998).
8. Hanson, R., Kouwenhoven, L. P., Petta, J. R., Tarucha, S. & Vandersypen, L. M. K. Spins in few-electron quantum dots. *Rev. Mod. Phys.* **79,** 1217–1265 (2007).
9. Zrenner, A. *et al.* Coherent properties of a two-level system based on a quantum-dot photodiode. *Nature* **418,** 612–614 (2002).
10. Kouwenhoven, L. P., Austing, D. G. & Tarucha, S. Few-electron quantum dots. *Rep. Prog. Phys.* **64,** 701–736 (2001).
11. Fujisawa, T., Austing, D. G., Tokura, Y., Hirayama, Y. & Tarucha, S. Allowed and forbidden transitions in artificial hydrogen and helium atoms. *Nature* **419,** 278–281 (2002).
12. Hayashi, T., Fujisawa, T., Cheong, H. D., Jeong, Y. H. & Hirayama, Y. Coherent manipulation of electronic states in a double quantum dot. *Phys. Rev. Lett.* **91,** 226804 (2003).
13. Khaetskii, A. V., Loss, D. & Glazman, L. Electron spin decoherence in quantum dots due to interaction with nuclei. *Phys. Rev. Lett.* **88,** 186802 (2002).
14. Merkulov, I. A., Efros, A. L. & Rosen, J. Electron spin relaxation by nuclei in semiconductor quantum dots. *Phys. Rev. B* **65,** 205309 (2002).
15. Golovach, V. N., Khaetskii, A. & Loss, D. Phonon-induced decay of the electron spin in quantum dots. *Phys. Rev. Lett.* **93,** 016601 (2004).
16. Elzerman, J. M. *et al.* Single-shot read-out of an individual electron spin in a quantum dot. *Nature* **430,** 431–435 (2004).
17. Hanson, R. *et al.* Single-shot readout of electron spin states in a quantum dot using spin-dependent tunnel rates. *Phys. Rev. Lett.* **94,** 196802 (2005).
18. Amasha, S. *et al.* Electrical control of spin relaxation in a quantum dot. *Phys. Rev. Lett.* **100,** 046803-1-4 (2008).
19. Levy, J. Universal quantum computation with spin-1/2 pairs and Heisenberg exchange. *Phys. Rev. Lett.* **89,** 147902 (2002).
20. Taylor, J. M. *et al.* Fault-tolerant architecture for quantum computation using electrically controlled semiconductor spins. *Nature Phys.* **1,** 177–183 (2005).
21. Hanson, R. & Burkard, G. Universal set of quantum gates for double-dot spin qubits with fixed interdot coupling. *Phys. Rev. Lett.* **98,** 050502 (2007).
22. DiVincenzo, D. P., Bacon, D.P., Kempe, J., Burkard, G. & Whaley, K. B. Universal quantum computation with the exchange interaction. *Nature* **408,** 339–342 (2000).
23. Ono, K., Austing, D. G., Tokura, Y. & Tarucha, S. Current rectification by Pauli exclusion in a weakly coupled double quantum dot system. *Science* **297,** 1313–1317 (2002).
24. Johnson, A. C. *et al.* Triplet–singlet spin relaxation via nuclei in a double quantum dot. *Nature* **435,** 925–928 (2005).
25. Koppens, F. *et al.* Control and detection of singlet–triplet mixing in a random nuclear field. *Science* **309,** 1346–1350 (2005).
26. Petta, J. R. *et al.* Coherent manipulation of coupled electron spins in semiconductor quantum dots. *Science* **309,** 2180–2184 (2005).
27. Koppens, F. H. L. *et al.* Driven coherent oscillations of a single electron spin in a quantum dot. *Nature* **442,** 766–771 (2006).
28. Kato, Y. *et al.* Gigahertz electron spin manipulation using voltage controlled g-tensor modulation. *Science* **299,** 1201–1204 (2003).
29. Laird, E. A. *et al.* Hyperfine-mediated gate-driven electron spin resonance. *Phys. Rev. Lett.* **99,** 246601 (2007).
30. Pioro-Ladriere, M. *et al.* Electrically driven single-electron spin resonance in a slanting Zeeman field. Preprint at <http://arxiv.org/abs/0805.1083> (2008).
31. Nowack, K. C., Koppens, F. H. L., Nazarov, Y. V. & Vandersypen, L. M. K. Coherent control of a single electron spin with electric fields. *Science* **318,** 1430–1433 (2007).
32. Awschalom, D. D. & Kikkawa, J. M. Electron spin and optical coherence in semiconductors. *Phys. Today* **52,** 33–38 (1999).
33. Kroutvar, M. *et al.* Optically programmable electron spin memory using semiconductor quantum dots. *Nature* **432,** 81–84 (2004).
34. Heiss, D. *et al.* Observation of extremely slow hole spin relaxation in self-assembled quantum dots. *Phys. Rev. B* **76,** 241306 (2007).
35. Bulaev, D. V. & Loss, D. Spin relaxation and decoherence of holes in quantum dots. *Phys. Rev. Lett.* **95,** 076805 (2005).
36. Berezovsky, J. *et al.* Nondestructive optical measurements of a single electron spin in a quantum dot. *Science* **314,** 1916–1920 (2006).
37. Atature, M., Dreiser, J., Badolato, A. & Imamoglu, A. Observation of Faraday rotation from a single confined spin. *Nature Phys.* **3,** 101–106 (2007).
38. Mikkelsen, M. H., Berezovsky, J., Stoltz, N. G., Coldren, L. A. & Awschalom, D. D. Optically detected coherent spin dynamics of a single electron in a quantum dot. *Nature Phys.* **3,** 770–773 (2007).
39. Imamoglu, A. *et al.* Quantum information processing using quantum dot spins and cavity QED. *Phys. Rev. Lett.* **83,** 4204–4207 (1999).
40. Cohen-Tannoudji, C. & Dupont-Roc, J. Experimental study of Zeeman light shifts in weak magnetic fields. *Phys. Rev. A* **5,** 968–984 (1972).
41. Berezovsky, J., Mikkelsen, M. H., Stoltz, N. G., Coldren, L. A. & Awschalom, D. D. Picosecond coherent optical manipulation of a single electron spin in a quantum dot. *Science* **320,** 349–352 (2008).
42. Meier, F. & Zakharchenya, B. P. (eds) *Optical Orientation* (North-Holland, Amsterdam, 1984).
43. Braun, P. F. *et al.* Direct observation of the electron spin relaxation induced by nuclei in quantum dots. *Phys. Rev. Lett.* **94,** 116601 (2005).
44. Bracker, A. S. *et al.* Optical pumping of the electronic and nuclear spin of single charge-tunable quantum dots. *Phys. Rev. Lett.* **94,** 047402 (2005).
45. Giedke, G., Taylor, J. M., D'Alessandro, D., Lukin, M. D. & Imamoglu, A. Quantum measurement of a mesoscopic spin ensemble. *Phys. Rev. A* **74,** 032316 (2006).

© 2008 Macmillan Publishers Limited. All rights reserved

46. Greilich, A. *et al.* Nuclei-induced frequency focusing of electron spin coherence. *Science* **317,** 1896–1899 (2007).
47. Stepanenko, D., Burkard, G., Giedke, G. & Imamoglu, A. Enhancement of electron spin coherence by optical preparation of nuclear spins. *Phys. Rev. Lett.* **96,** 136401 (2006).
48. Klauser, D., Coish, W. A. & Loss, D. Nuclear spin state narrowing via gate-controlled Rabi oscillations in a double quantum dot. *Phys. Rev. B* **73,** 205302 (2006).
49. Baugh, J., Kitamura, Y., Ono, K. & Tarucha, S. Large nuclear Overhauser fields detected in vertically coupled double quantum dots. *Phys. Rev. Lett.* **99,** 096804 (2007).
50. Coish, W. A. & Loss, D. Hyperfine interaction in a quantum dot: Non-Markovian electron spin dynamics. *Phys. Rev. B* **70,** 195340 (2004).
51. Gerardot, B. D. *et al.* Optical pumping of a single hole spin in a quantum dot. *Nature* **451,** 441–444 (2008).
52. Atatüre, M. *et al.* Quantum-dot spin-state preparation with near-unity fidelity. *Science* **312,** 551–553 (2006).
53. Mason, N., Biercuk, M. J. & Marcus, C. M. Local gate control of a carbon nanotube double quantum dot. *Science* **303,** 655–658 (2004).
54. Sapmaz, S., Meyer, C., Beliczynski, P. M., Jarillo-Herrero, P. D. & Kouwenhoven,L. P. Excited state spectroscopy in carbon nanotube double quantum dots. *Nano Lett.* **6,** 1350–1355 (2006).
55. Hu, Y. *et al.* Double quantum dot with integrated charge sensor based on Ge/Si heterostructure nanowires. *Nature Nanotech.* **2,** 622–625 (2007).
56. Simmons, C. B. *et al.* Single-electron quantum dot in Si/SiGe with integrated charge sensing. *Appl. Phys. Lett.* **91,** 213103 (2007).
57. Liu, H. W. *et al.* Pauli-spin-blockade transport through a silicon double quantum dot. *Phys. Rev. B* **77,** 073310 (2008).
58. Besombes, L. *et al.* Probing the spin state of a single magnetic ion in an individual quantum dot. *Phys. Rev. Lett.* **93,** 207403 (2004).
59. Léger, Y., Besombes, L., Fernández-Rossier, J., Maingault, L. & Mariette, H. Electrical control of a single Mn atom in a quantum dot. *Phys. Rev. Lett.* **97,** 107401 (2006).
60. Erwin, S. C. Nanomagnetism: spin doctors play with single electrons. *Nature Nanotech.* **1,** 98–99 (2006).
61. Myers, R. C. *et al.* Zero-field optical manipulation of magnetic ions in semiconductors. *Nature Mater.* **7,** 203–208 (2008).
62. Awschalom, D. D., Epstein, R. & Hanson, R. The diamond age of spintronics. *Sci. Am.* **297,** 84–91 (2007).
63. Reynhardt, E. C., High, G. L. & vanWyk, J. A. Temperature dependence of spin–spin and spin–lattice relaxation times of paramagnetic nitrogen defects in diamond. *J. Chem. Phys.* **109,** 84718477 (1998).
64. Gruber, A. *et al.* Scanning confocal optical microscopy and magnetic resonance on single defect centers. *Science* **276,** 2012–2014 (1997).
65. Jelezko, F., Popa, I., Gruber, A. & Wrachtrup, J. Single spin states in a defect center resolved by optical spectroscopy. *Appl. Phys. Lett.* **81,** 2160–2162 (2002).
66. Jelezko, F., Gaebel, T., Popa, I., Gruber, A. & Wrachtrup, J. Observation of coherent oscillations in a single electron spin. *Phys. Rev. Lett.* **92,** 76401 (2004).
67. Jelezko, F. *et al.* Observation of coherent oscillation of a single nuclear spin and realization of a two-qubit conditional quantum gate. *Phys. Rev. Lett.* **93,** 130501 (2004).
68. Rabeau, J. R. *et al.* Single nitrogen vacancy centers in chemical vapor deposited diamond nanocrystals. *Nano Lett.* **7,** 3433–3437 (2007).
69. Park, Y.-S., Cook, A. K. & Wang, H. Cavity QED with Diamond nanocrystals and silica microspheres. *Nano Lett.* **6,** 2075–2079 (2006).
70. Kennedy, T. A. *et al.* Long coherence times at 300 K for nitrogen–vacancy center spins in diamond grown by chemical vapor deposition. *Appl. Phys. Lett.* **83,** 4190–4192 (2003).
71. Gaebel, T. *et al.* Room-temperature coherent coupling of single spins in diamond. *Nature Phys.* **2,** 408–413 (2006).
72. Hanson, R., Mendoza, F. M., Epstein, R. J. & Awschalom, D. D. Polarization and readout of coupled single spins in diamond. *Phys. Rev. Lett.* **97,** 087601 (2006).
73. Hanson, R., Dobrovitski, V. V., Feiguin, A. E., Gywat, O. & Awschalom, D. D. Coherent dynamics of a single spin interacting with an adjustable spin bath. *Science* **320,** 352–355 (2008).
74. Takahashi, S., Hanson, R., van Tol, J., Sherwin, M. S. & Awschalom, D. D. Quenching spin decoherence in diamond through spin bath polarization. Preprint at <http://arxiv.org/abs/0804.1537> (2008).
75. Meijer, J. *et al.* Generation of single colour centers by focussed nitrogen implantation. *Appl. Phys. Lett.* **87,** 261909 (2005).
76. Rabeau, J. R. *et al.* Implantation of labelled single nitrogen vacancy centers in diamond using 15N. *Appl. Phys. Lett.* **88,** 023113 (2006).
77. Childress, L. *et al.* Coherent dynamics of coupled electron and nuclear spin qubits in diamond. *Science* **314,** 281–285 (2006).
78. Dutt, M. V. G. *et al.* Quantum register based on individual electronic and nuclear spin qubits in diamond. *Science* **316,**1312–1316 (2007).
79. Tamarat, P. *et al.* Stark shift control of single optical centers in diamond. *Phys. Rev. Lett.* **97,** 083002 (2006).
80. Santori, C. *et al.* Coherent population trapping of single spins in diamond under optical excitation. *Phys. Rev. Lett.* **97,** 247401 (2006).
81. Barrett, S. D. & Kok, P. Efficient high-fidelity quantum computation using matter qubits and linear optics. *Phys. Rev. A* **71,** 060310 (2005).
82. Moehring, D. L. *et al.* Entanglement of single-atom quantum bits at a distance. *Nature* **449,** 68–72 (2007).
83. Averin, D. V. & Nazarov, Y. V. Virtual electron diffusion during quantum tunnelling of the electric charge. *Phys. Rev. Lett.* **65,** 2446–2449 (1990).
84. Coish, W. A. & Loss, D. Singlet–triplet decoherence due to nuclear spins in a double quantum dot. *Phys. Rev. B* **72,** 25337 (2005).
85. Hu, X. & Das Sarma, S. Charge-fluctuation-induced dephasing of exchange-coupled spin qubits. *Phys. Rev. Lett.* **96,** 100501 (2006).
86. Jung, S. W., Fujisawa, T., Hirayama, Y. & Jeong, Y. H. Background charge fluctuation in a GaAs quantum dot device. *Appl. Phys. Lett.* **85,** 768–770 (2004).

Acknowledgements We thank the Air Force Office of Scientific Research (AFOSR), the Dutch Organization for Fundamental Research on Matter (FOM) and the Netherlands Organization for Scientific Research (NWO) for support.

Author Information Reprints and permissions information is available at npg.nature.com/reprints. The authors declare no competing financial interests. Correspondence should be addressed to the authors (r.hanson@tudelft.nl; awsch@physics.ucsb.edu).

© 2008 Macmillan Publishers Limited. All rights reserved